STRUCTURAL DESIGN AND ANALYSIS OF THE MISSION ADAPTIVE WINGS OF AN UNMANNED AERIAL VEHICLE

A THESIS SUBMITTED TO
THE GRADUATE SCHOOL OF NATURAL AND APPLIED SCIENCES
OF
MIDDLE EAST TECHNICAL UNIVERSITY

BY

LEVENT ÜNLÜSOY

IN PARTIAL FULFILLMENT OF THE REQUIREMENTS
FOR
THE DEGREE OF MASTER OF SCIENCE
IN
AEROSPACE ENGINEERING

FEBRUARY 2010

Approval of the thesis:

STRUCTURAL DESIGN AND ANALYSIS OF THE MISSION ADAPTIVE WINGS OF AN UNMANNED AERIAL VEHICLE

submitted by **LEVENT ÜNLÜSOY** in partial fulfillment of the requirements for the degree of **Master of Science in Aerospace Engineering Department, Middle East Technical University** by,

Prof. Dr. Canan Özgen _____
Dean, Graduate School of **Natural and Applied Sciences**

Prof. Dr. Ozan Tekinalp _____
Head of Department, **Aerospace Engineering**

Prof. Dr. Yavuz Yaman _____
Supervisor, **Aerospace Engineering Dept., METU**

Examining Committee Members:

Prof. Dr. Serkan Özgen _____
Aerospace Engineering Dept., METU

Prof. Dr. Yavuz Yaman _____
Aerospace Engineering Dept., METU

Assist. Prof. Dr. Melin Şahin _____
Aerospace Engineering Dept., METU

Assist. Prof. Dr. Ender Ciğeroğlu _____
Mechanical Engineering Dept., METU

Özcan Ertem, M.Sc. _____
Executive Vise President, TAI

Date: 05.02.2010

I hereby declare that all the information in this document has been obtained and presented in accordance with academic rules and ethical conduct. I also declare that, as required by these rules and conduct, I have fully cited and referenced all material and results that are not original to this work.

Name, Last Name:

Signature:

ABSTRACT

STRUCTURAL DESIGN AND ANALYSIS OF THE MISSION ADAPTIVE WINGS OF AN UNMANNED AERIAL VEHICLE

Ünlüsoy, Levent
M.Sc., Department of Aerospace Engineering
Supervisor : Prof. Dr. Yavuz Yaman

February 2010, 114 pages

In this study, the structural design and analysis of a wing having mission-adaptive control surfaces were conducted. The wing structure was designed in order to withstand a maximum aerodynamic loading of 5 g due to maneuver. The structural model of the wing was developed by using MSC/PATRAN package program and that structural model was analyzed by using MSC/NASTRAN package program. The designed wing was then manufactured by Turkish Aerospace Industries Inc. (TUSAŞ-TAI). The finite element analysis results were verified by conducting ground vibration tests on the manufactured wing. The comparative results were used to tune the finite element model and the results obtained showed that the modeling was very successful.

Keywords: Aircraft Structural Design, Finite Element Analysis, Mission-Adaptive Wing, Experimental Model Tuning

ÖZ

İNSANSIZ BİR HAVA ARACININ GÖREVE UYUMLU KANATLARININ YAPISAL TASARIM VE ANALİZİ

Ünlüsoy, Levent
Yüksek Lisans, Havacılık ve Uzay Mühendisliği Bölümü
Tez Yöneticisi : Prof. Dr. Yavuz Yaman

Şubat 2010, 114 sayfa

Bu çalışmada, göreve uyumlu kontrol yüzeylerine sahip bir kanadın yapısal tasarımı ve analizi yapılmıştır. Kanat, uçağın 5 g değerinde azami aerodinamik yükleme ile yaptığı manevralara dayanabilecek şekilde tasarlanmıştır. Kanadın yapısal modeli MSC/PATRAN paket programı kullanılarak oluşturulmuş, bu yapısal modelin analizleri MSC/NASTRAN paket programı kullanılarak yapılmıştır. Akabinde, tasarlanan kanat Türk Havacılık ve Uzay Sanayii A.Ş. (TUSAŞ-TAI) tarafında üretilmiştir. Sonlu elemanlar analizlerinden elde edilen sonuçlar, üretilen kanadın yer titreşim testleri yapılarak doğrulanmıştır. Karşılaştırmalı sonuçlar kanat modelinin uyumlamasında kullanılmış; alınan sonuçlar oluşturulan modelin son derece başarılı olduğunu göstermiştir.

Anahtar Kelimeler: Hava Araçlarının Yapısal Tasarımı, Sonlu Eleman Analizi, Göreve Uyumlu Kanat, Deneysel Model Uyumlaması

to my precious family

and

beloved wife

for their love, care and support

and

to my friends

for their patience over years

ACKNOWLEDGEMENTS

I would like to express my gratitude to my supervisor Prof. Dr. Yavuz Yaman for his patient guidance, encouragements, insight and support in this study.

I must also express my appreciation to my superiors within the project, Assist. Prof. Dr. Güçlü Seber, Assist. Prof. Dr. Melin Şahin and Prof. Dr. Serkan Özgen for their guidance.

I would like to deeply thank my colleagues Erdoğan Tolga İnsuyu and Evren Sakarya for their help throughout this thesis study.

I would also gratefully appreciate the support and assistance of all my cherished friends but especially Mehmet Efruz Yalçın.

I would like to thank my parents for their guidance and insight and my sister and wife for their care and support.

Finally, this work was partially supported by The Scientific and Technological Research Council of Turkey, through the project 'TUBITAK/107M103, Aeroservoelastic Analysis of the Effects of Camber and Twist on Tactical Unmanned Aerial Vehicle Mission-Adaptive Wings'. The author gratefully acknowledges the support given.

TABLE OF CONTENTS

LIST OF TABLES

TABLES

LIST OF FIGURES

FIGURES

LIST OF SYMBOLS

A	Aspect Ratio
b	Wing Span
c	Wing Chord Length
C_p	Aerodynamic Pressure Coefficient
E	Young's Modulus
g	Gravitational Acceleration
G	Shear Modulus
I	Second Moment of Area
L	Lifting Force
n	Aerodynamic Load Factor
t/c	Thickness to Chord Ration
V	Volume Fraction
W	Weight
λ	Taper Ratio
ν	Poisson's Ratio

LIST OF ABBREVIATIONS

0D	Dimensionless
1D	One Dimensional
2D	Two Dimensional
3D	Three Dimensional
CAD	Computer Aided Design
CNC	Computer Numerical Control
CS	Cross Sectional
FEA	Finite Element Analysis
FEM	Finite Element Method
FFT	Fast Fourier Transformation
FRF	Frequency Response Function
GVT	Ground Vibration Tests
LE	Leading Edge
MPC	Multi Point Constraint
NACA	National Advisory Committee of Aeronautics
RBE	Rigid Body Element
TE	Trailing Edge
UAV	Unmanned Aerial Vehicle

CHAPTER 1

INTRODUCTION

1.1 Background to the Study

This thesis study was devoted to the structural design and analyses of a wing particularly built for an unmanned aerial vehicle (UAV) having mission-adaptive control-surfaces. The study was conducted within the scope of a research and development project 'Aeroservoelastic Analysis of the Effects of Camber and Twist on Tactical Unmanned Aerial Vehicle Mission-Adaptive Wings' which was supported by The Scientific and Technological Research Council of Turkey (TUBITAK) under the project code of 107M103. The fuselage and the tail of the unmanned aerial vehicle was designed and analyzed by Erdoğan Tolga İnsuyu [1] and the mission adaptive control surfaces, which have the ability to change the effective camber and twist of the wing, were designed and analyzed by Evren Sakarya [2] within the same project.

1.2 Scope of the Study

Chapter 2 of the thesis gives the literature survey about the unconventional air vehicles and the structural issues related to those.

The design lay-out of the considered wing was given in Chapter 3.

The detailed finite element model generated by using MSC®/PATRAN package program was presented in Chapter 4.

The structural analyses which were conducted by using MSC®/NASTRAN package program were detailed in Chapter 5.

The manufacturing process of the wing, which was completed by Turkish Aerospace Industries Inc. (TUSAŞ-TAI), was explained in detail in Chapter 6.

Chapter 7 of the study gives the details and results of the ground vibration tests, which were conducted on the manufactured wing.

The verification analysis and the resultant tuning of the developed structural model, which was done with the help of experimental data obtained, were presented in Chapter 8.

Chapter 8 concludes the work with the general conclusions drawn and the recommendations for the future work.

1.3 Limitations of the Study

The model developed within this thesis is confined to the design limitations of the unmanned aerial vehicle studied within the framework of the project 'TUBITAK 107M103 Aeroservoelastic Analysis of the Effects of Camber and Twist on Tactical Unmanned Aerial Vehicle Mission-Adaptive Wings'. The wing structure to be designed should safely sustain the requirements of the smart control surfaces in order to increase the control surface effectiveness [2]. The control surface effectiveness was highly dependent on the actuators driving them. The actuation capacity of these devices must fully be transmitted to the control surfaces. The best way to establish this was to design the wing torque box with maximum possible lateral rigidity hence the design procedures were followed accordingly.

CHAPTER 2

LITERATURE REVIEW

2.1 Mission Adaptive Aerial Vehicles

The mission adaptive aerial vehicles have the capability to change their shape in order to adapt themselves to the changing flight conditions and/or the mission profile of the vehicle. The aims of the mission adaptive flight vehicles are to fly different kinds of missions, perform effective maneuvers and have increased fuel efficiency [3].

The available shape changing mechanisms are divided into two main areas. The first one is the wing planform change, which can be classified as wing extension, wing sweep and wing folding. The second one is the compliance, which can be summarized as twist and camber changes. The wing planform changes generally considered for the increase of the mission capability of the vehicle whereas compliances are applied for the control purposes [4].

The planform changes applied on the wing can alter the mission profile of the aircraft, since each and every mission has its own effective wing configuration. For instance, the concept can increase efficiency at attack by decreasing the aspect ratio while by increasing the aspect ratio then it can increase the loiter efficiency and so on. One of the most effective examples for wing planform changes related to the mission is the conceptual aircraft of NextGen, MAS [5], where the planform changes of the wing are shown in Figure 1.

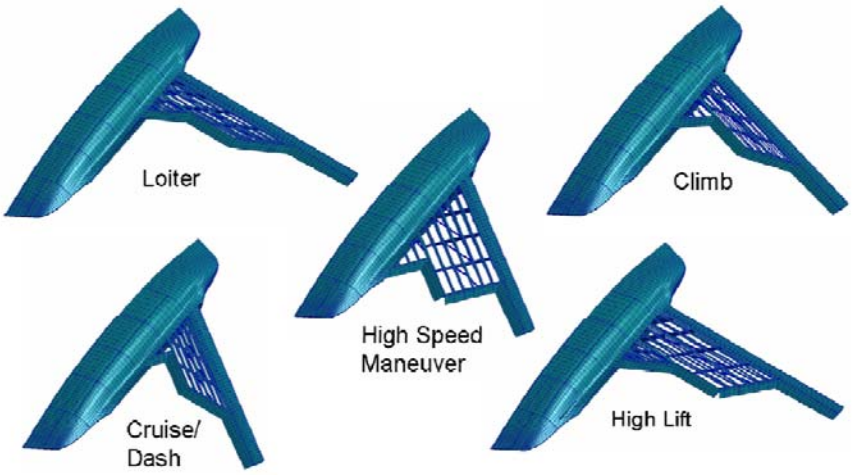

Figure 1: NextGen MAS Wing Planform Change Concept [5]

The wing planform changes can also be used for limited control aspects. The anti-symmetric extension of the wing can create a rolling moment which can replace the conventional ailerons. Figure 2 shows an example of anti-symmetric wing extension.

Figure 2: Anti-symmetric Wing Extension Mechanism [3]

Another example for the planform changes is the folding wing concept. Figure 3 shows Lockheed Martin's folding wing tactical UAV.

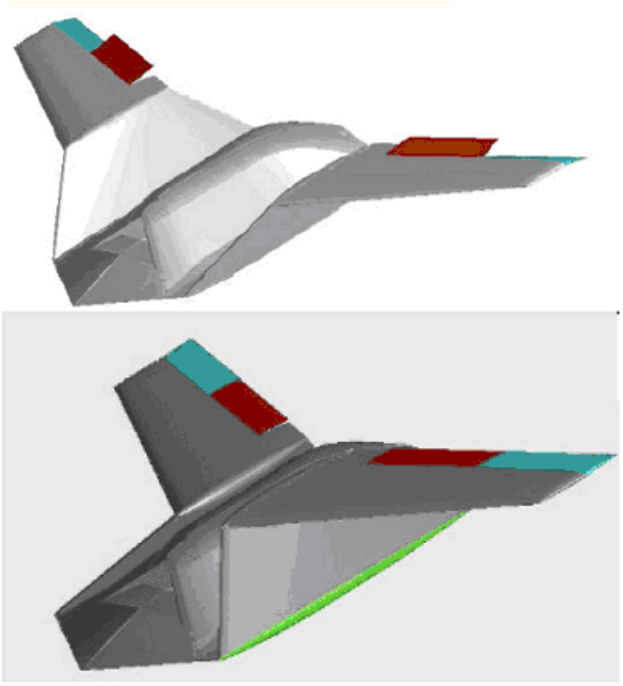

Figure 3: Lockheed Martin Folding Wing Concept [3]

The compliance type morphing concepts generally deals with the twist and camber changes on the wings. In this concept the main aim is to eliminate the conventional control surfaces and seams, and control the vehicle with continuous changes on the wing section. The figure below shows the compliant morphing wing concept developed by FlexSys Inc. [6].

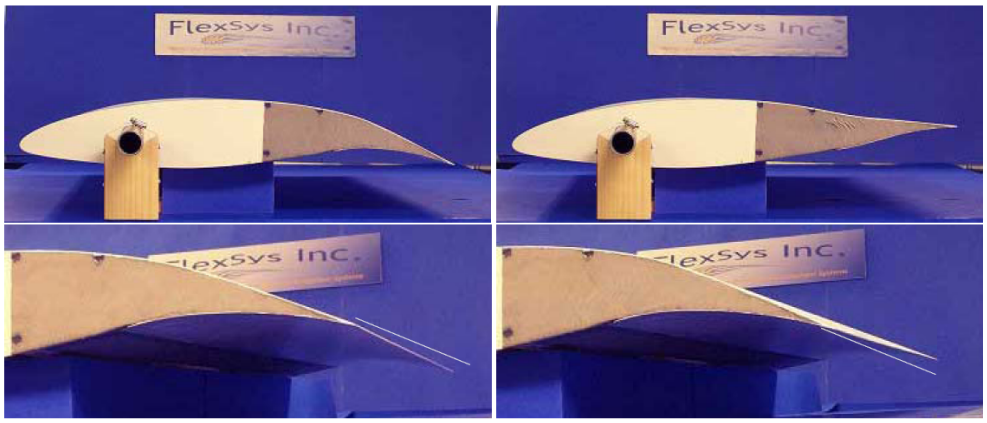

Figure 4: Compliant Morphing Wing Concept of FlexSys Inc. [6]

2.2 Structural Issues in Mission Adaptive Wing Concept

The morphing wing concepts increase efficiency of the aerial vehicles in terms of both mission adaptation and control performance in the expense of simple structural design. The developed concepts all require, somehow complicated structural design and therefore increase total weight of the wing. Moreover, these complicated structural designs increase the development and/or prototype costs. The complicated internal structural design of the NextGen's MAS is outlined in Figure 5.

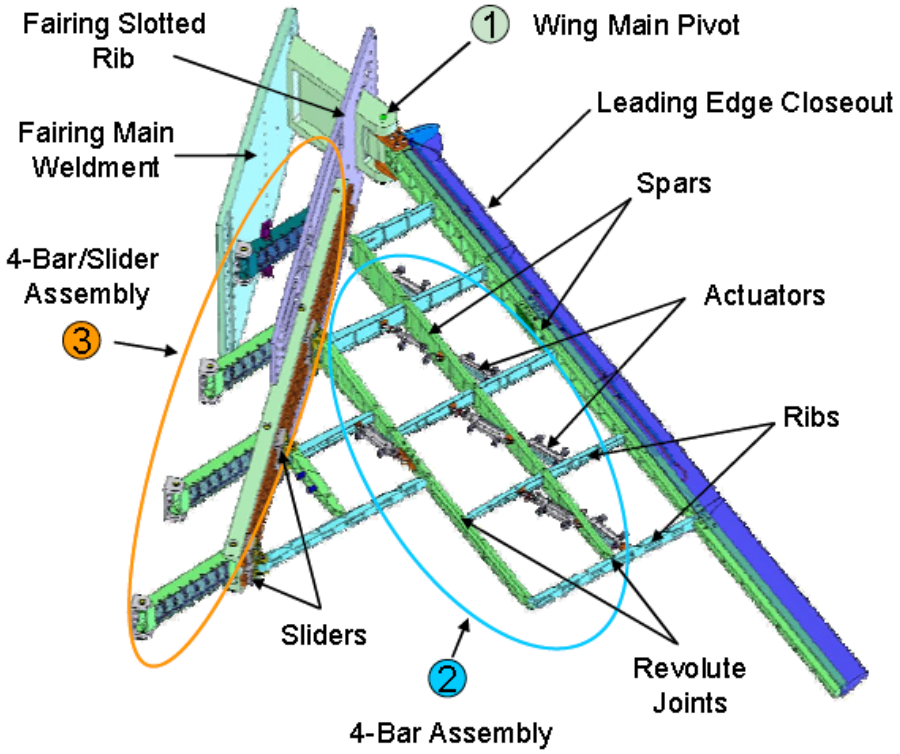

Figure 5: The Internal Structure of the NextGen's MAS [5]

There was a mission adaptive wing concept developed for the F-111A having supercritical wings which effectively increases its high altitude supersonic mission radius by 139 %. This mission adaptive wing concept also has a very complicated internal structural design which can be seen in Figure 6.

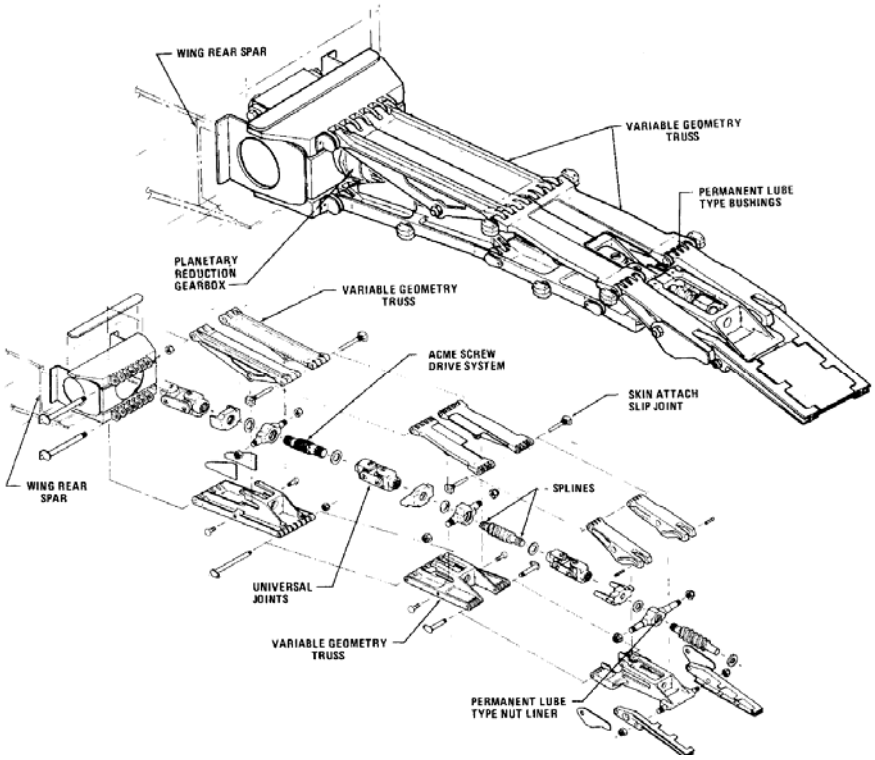

Figure 6: Internal Structure of F-111A Trailing Edge Morphing Concept [4]

The morphing concept can effectively change the aircraft performance parameters; however, it also changes the structural requirements of the wing. For instance, when the wing planform area changes during flight, the load distribution over the wing also changes. In addition to that, the profile changes may also cause a change in the location of the center of gravity (CG) of the aircraft, which effectively alters the characteristics of the overall structure. These possible changes require the necessity of designing a structure which can either change its characteristics with the shape changes or withstand to all the loading profiles to be encountered. Moreover, the CG location should be corrected in order to encounter the possible disadvantages caused by the change of mechanical stability of the vehicle. This is the most important design limitation of a mission adaptive structure.

CHAPTER 3

DESIGN OF THE MISSION ADAPTIVE WING

3.1 Introduction

This chapter is devoted to the design of the mission adaptive wing on which the smart control surfaces will be installed. The designed smart control surfaces have open cross-sections. The most effective way in alleviating the associated problems of the open cross-sections was to design the stiffest possible torque box structure for the wing without exceeding the weight limitation for the wing.

The basic parameters such as airfoil section, wing planform area S, wing chord length c, wing span b, aspect ratio A, taper ratio λ and thickness to chord ratio t/c should have been decided at early stages of the aircraft conceptual design. Table 1 shows details of these parameters for the wing designed in this study.

Table 1: Aircraft Conceptual Design Wing Geometric Parameters (SI Units)

Airfoil Section	NACA 4412
Planform Area, S	1.5 [m^2]
Chord Length, c	0.5 [m]
Wing Span, b	3 [m]
Aspect Ratio, A	6
Taper Ratio, λ	1
Thickness to Chord Ratio, t/c	0.12

The typical wing control surface chord length to wing chord length ratio is in between 0.15 and 0.25 [7]. For the wing considered it was decided to be 0.4 to increase the control surface effectiveness.

The approximate empty weight build up for general aviation purposes claims that a wing weighs 2.5 [lb/ft^2] [7]. The total estimate mass of the wings of the current design was calculated as 18.3 [kg].

3.2 Design of Main Structural Parts and Selection of Materials

3.2.1 Location of Spars

The design of main structural parts such as spars, ribs and skin depends on the selected design parameters. The starting point of design of a wing box structure is selection of the number of spars. The spars are the main load carrying member of the wing structure. They generally undergo torsional and bending stresses due to aerodynamic loading they are subjected to during the flight. This wing should be consisting of a spar located at 60 % of the chord to support the smart control surfaces which has a chordwise length of 0.4 times the length of the chord. Although, the wing of subject was comparably small in size only one spar cannot sustain the continuity of the wing, and hence there should be another spar in the wing box structure. The historical design data indicates that for a two-spar wing the front (or main) spar should be located in between 12 % and 17 % of the chord if the rear (or secondary) spar is located at 55 % to 60 % of the chord [9]. The main reason behind this is to make the neutral axis and the shear center coincide in order to improve the aeroelastic characteristics of the wing. This combination of spars holds true for the closed cross-section wings, however, for the open cross-section wing considered the shear center will be shifted to the leading edge. In order to shift it back to its meant location the best option seemed to locate the main spar at around 25 % of the chord. Hence, the locations of the spars are selected as shown in Table 2.

Table 2: Chordwise Locations of the Spars

Structural Member	Chordwise Location w.r.t. Leading Edge
Main Spar	25 %
Secondary Spar	60 %

3.2.2 Selection of Materials

The most important factors for the selection of the materials used are the yield and ultimate strengths, corrosion and thermal resistance, stiffness and density. Other important factors are the manufacturability, cost and availability [7]. The most common aerospace materials such as wood, aluminum, steel, nickel, magnesium, titanium and fiber reinforced composites were being investigated at this section.

First eliminated material was the wood basically due to very low stiffness value. Secondly, the overall weight of the structure was considered and automatically eliminated the high stiffness and strength materials such as steel and nickel. The cost criterion left the ideal aerospace material titanium out since titanium is regarded as the ideal aerospace material since it has the highest stiffness to weight ratio. Finally, the availability problem of magnesium diverted the study to either aluminum or fiber reinforced composites. It was decided the inner-members of the wing box structure should be manufactured from aluminum and skin should be manufactured from fiber reinforced composites.

3.2.3 Rib Locations

Since it was detailed in [2] it was planned to install four actuators inside each wing. These actuators needed support arms to fully apply their actuation forces to the control surfaces. Therefore, at least four support ribs for the actuation were needed. In addition to that four more ribs will be needed to stiffen main and secondary spar relative distortions, and prevent skin panels from buckling by reducing the panel

lengths and hence increasing critical buckling stress. The total ribs inside each of the wing torque box will then be eight for each of the wings. Table 3 gives the spanwise distances of the rib segments from the root section of the wing. The rib segmental numbers started from the root section. In addition to that, Figure 7 gives the top view of the internal structure and shows the spar and the rib locations.

Table 3: The Spanwise Distances of the Rib Segments from the Root Section of the Wing

Rib Segmental Number	Distance From the Root Section of the Wing [mm]
1	150
2	300
3	475
4	625
5	800
6	1000
7	1250
8	1500

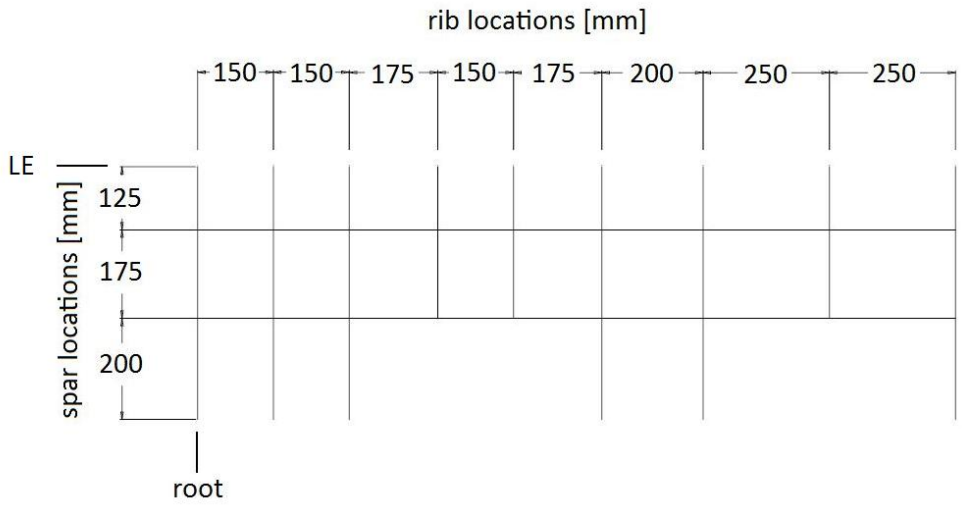

Figure 7: Top View of the Internal Structural Design [mm]

3.2.4 Member Thicknesses and Final Selection of Materials

A computer program in Microsoft Excel has been prepared to calculate the necessary geometric data and as well as the lateral rigidity values for the cross-sections. Hence the materials selected and geometric values were calculated for the wing torque box structural members and these properties are given in Table 4. APPENDIX A outlines the details of the algorithm developed.

Table 4: Material, Thickness, and Lateral Rigidity Values of the Wing Torque Box Structural Members

Structural Member	Material	Thickness [mm]	Second Moment of Area, I [m^4]	Lateral Rigidity, EI [$N.m^2$]
Main Spar	Aluminum 7075-T651	2.54	1.019E-07	7440
Secondary Spar	Aluminum 7075-T651	2.54	6.760E-08	4930
Skin	7781 E-Glass Fiber - Araldite LY5052 Resin	1.08 (4 layers laminate)	2.604E-08	5730
Ribs	Aluminum 2024-T3	0.8	Negligible for Euler-Bernoulli Beam Assumption	Negligible for Euler-Bernoulli Beam Assumption

The combination had resulted in a total mass of 5.35 [kg]. The mass calculated was determined to be less than the value estimated, however, the connectors, fasteners and fittings would bring additional mass to the structure in later stages. Table 5, Table 6 and Table 7 give the mechanical and physical properties of the selected materials.

Table 5: 2D Orthotropic Properties of 7781 E-Glass Fabric–Araldite LY5052 Resin–Aradur HY5052 Hardener Composite Material Selected for the Skin [10]

Density	1772 [kg/m^3]
Young's Modulus, E_{11}	22.1 [GPa]
Young's Modulus, E_{22}	22.4 [GPa]
Shear Modulus, G_{12}	3.79 [GPa]
Shear Modulus, G_{23}	2.96 [GPa]
Shear Modulus, G_{13}	2.96 [GPa]
Ultimate Compression Strength	249 [MPa]
Ultimate Tensile Strength	369 [MPa]
Inter-laminar Shear Strength	33.21 [MPa]

Table 6: Physical and Mechanical Properties of Aluminum 7075-T651 Material Selected for the Spars [11]

Density	2810 [kg/m^3]
Young's Modulus, E	71.7 [GPa]
Shear Modulus, G	26.9 [GPa]
Poison's Raito, ν	0.33
Ultimate Strength	572 [MPa]
Yield Strength	503 [MPa]
Shear Strength	331 [MPa]

Table 7: Physical and Mechanical Properties of Aluminum 2024-T3 Material Selected for the Ribs [11]

Density	2780 [kg/m^3]
Young's Modulus, E	73.1 [GPa]
Shear Modulus, G	28.0 [GPa]
Poison's Raito, ν	0.33
Ultimate Strength	483 [MPa]
Yield Strength	385 [MPa]
Shear Strength	283 [MPa]

3.2.5 Discussion and Conclusion

This detailed the design phases of the mission adaptive wing of the Unmanned Aerial Vehicle. During the design, historical data was used as a guideline and the general characteristics of the wing are decided. Inevitably there will be some design changes to occur in the following chapters. Since the necessary requirements seem to be satisfied, these modifications were assumed to be minor.

CHAPTER 4

STRUCTURAL MODELLING OF THE MISSION ADAPTIVE WING

4.1 Introduction

The structural modeling of the designed wing will be conducted by using the Finite Element Method and MSC®/PATRAN Package program. This chapter describes the selection of the element types, solid modeling for FEM, part connection methods, mesh generation and the boundary conditions.

4.2 Selection of Element Types

The most commonly used element type in aerospace industry is the two-dimensional (2D) elements since the industry is mostly dealing with thin walled structures. Almost every main structural part can be modeled using this type of elements. 1D type elements on the other hand also have applications for connecting apparatus and mostly for beamlike structures. Moreover, additional masses having no stiffness effect such as avionic equipments and their cabling systems can be modeled using 0D type of elements. Nevertheless, 3D type elements are not preferred for aerospace applications.

As it was mentioned before, 2D type elements are the most commonly used element type in aviation industry. This type of elements generally designed for thin walled structures such as the skin, however, for the wing considered the thicknesses of the other members of the torque box were also small. Thus, those members could also be considered as thin walled structures and were modeled by using 2D type elements. When the spars were taken into account, it was determined that the webs of

the spars should be modeled by using 2D shell element in order to get torsion response where the flanges should be modeled using 1D beam elements to get more accurate results in bending responses.

Since skin was a thin walled structure, the element types would be '2D Shell Elements'. The last set of main structural parts was the ribs which were used to increase the torsional stiffness of the wing structure and skin panel stability. The ribs were the structural parts generally undergo stresses which caused by the relative motion of the spars and skin panels connected to them. Moreover, in application mostly the resultant stress levels on the ribs, except the concentrated stresses around fasteners, assumed to be very low compared to the stresses on the spars and the skin. Hence, for convenience, the same element type of the skin is assigned for the ribs. Table 8 gives the summary of results of this section of the study.

Table 8: Summary of Selection of Element Types

Structural Member	Element Type
Spar Webs	2D Shell
Spar Flanges	1D Beam
Skin	2D Shell
Ribs	2D Shell

4.3 Geometrical Modeling for Finite Element Method

The geometrical modeling of the main structural members were done by generating surfaces at the mid-planes of the structural parts for which 2D shell elements were assigned. Then, the edges of the surfaces generated for the spar webs were used to create the 1D beam elements assigned for the spar flanges.

First the geometrical model of the composite skin was generated. Figure 8 gives the isometric view of the surfaces representing the skin of the wing torque box designed.

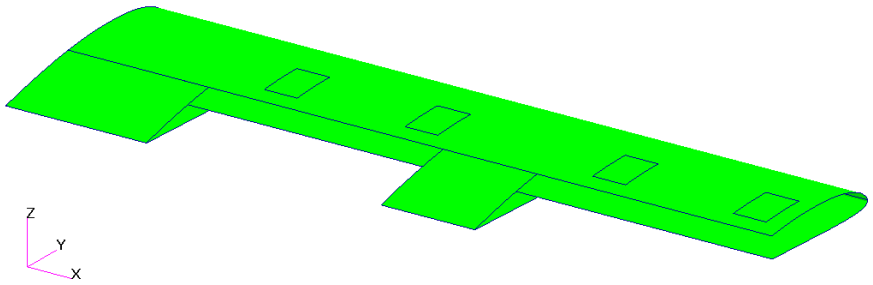

Figure 8: Isometric View of the Torque Box Skin Surfaces

Afterwards, the ribs were generated each in three portions. The first portion was located at the leading edge section up to the location of the main spar web. The second portion was in between the two spar webs. The last portion started at the secondary spar web and continued until the trailing edge. Figure 9 gives the isometric view of all the ribs and the Figure 10 is the zoomed isometric view of three portions of a unique rib.

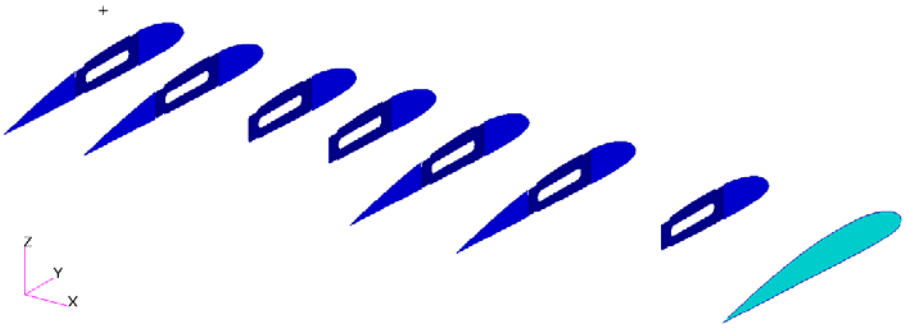

Figure 9: Isometric View of the Geometrical Model of the Ribs

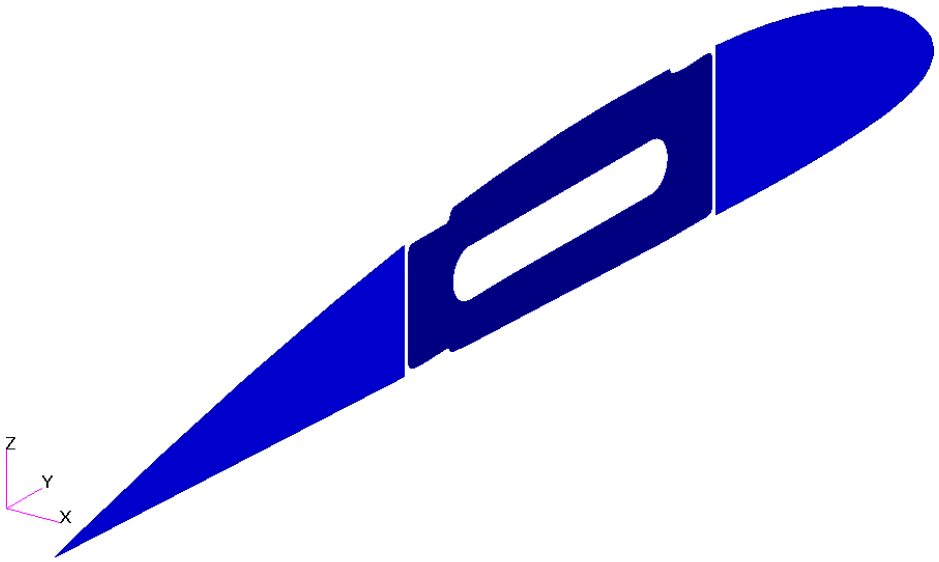

Figure 10: Isometric View of a Unique Rib Segment

Finally, surfaces representing the webs of the spars of the wing torque box were generated. Note that the edges of these surfaces represent the flanges. Figure 11 is the isometric view of the spars. The isometric view of the wing torque box internal geometry ready for meshing is given in Figure 12.

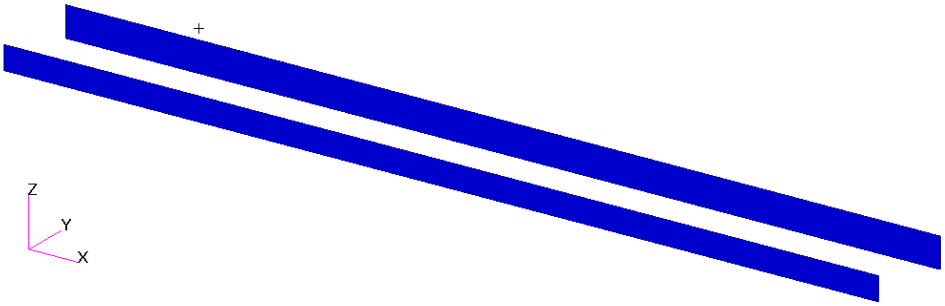

Figure 11: Isometric View of the Geometrical Model of the Spar Webs

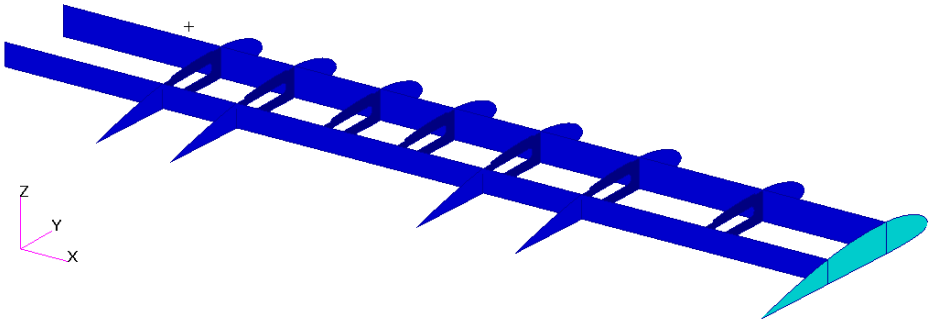

Figure 12: Isometric View of the Geometrical Model of Torque Box Internal Structure

4.4 Material and Element Property Definition

There were four materials introduced to the software, two of which were the isotropic materials Aluminum 2024-T3 and Aluminum 7075-T651. The third material defined was the 2D orthotropic lamina properties of the woven 7781 E-Glass Fabric with LY5052 Resin and HY5052 Hardener. The forth material was the four layer (Note that since the glass fabric is a woven fabric each layer is formed of fiber sequence of 0°/90°) laminated composite with the combined staking sequence of 0°/90°/0°/90°/0°/90°/0°/90° and ply thickness of 0.27 [mm] [10]. Table 9 gives the relevant property sets.

Table 9: Summary of the Property Sets Used in the Finite Element Model

Element Property	Material	Thickness or CS Area
Spar Webs	Aluminum 7075-T652	2.54 [mm]
Main Spar Flange	Aluminum 7075-T652	65 [mm^2]
Secondary Spar Flange	Aluminum 7075-T652	65 [mm^2]
Leading Edge Ribs	Aluminum 2024-T3	0.8 [mm]
Trailing Edge Ribs	Aluminum 2024-T3	0.8 [mm]
Mid-chord Ribs	Aluminum 2024-T3	0.8 [mm]
Tip Rib	Aluminum 2024-T3	0.8 [mm]
Corner Connectors	Aluminum 7075-T652	1.65 [mm]
Composite Skin	4 Layer Laminated Composite	1.08 [mm]

4.5 Mesh Generation

The parametric (simple) surfaces such as the spars can be meshed using meshing technique called the 'Iso Meshing', whereas non-parametric (advanced) surfaces such as ribs and skin can only be meshed using 'Paver Meshing' method [13]. Iso Meshing method create elements having same angles between edges, however, Paver Meshing only keeps the global element edge length defined for meshing approximately the same, and then it creates non-symmetrical elements.

First the connection locations had to be identified. There were two sets of connection locations for the wing analyzed. The first one was the connection between spars and the skin and the second one was the connection between the ribs and the skin.

When all the necessary edges for the defined connection sets were associated to the related parent surface, the resulting geometry can be seen in Figure 13. The small triangles shown in Figure 13 define the associations between geometries.

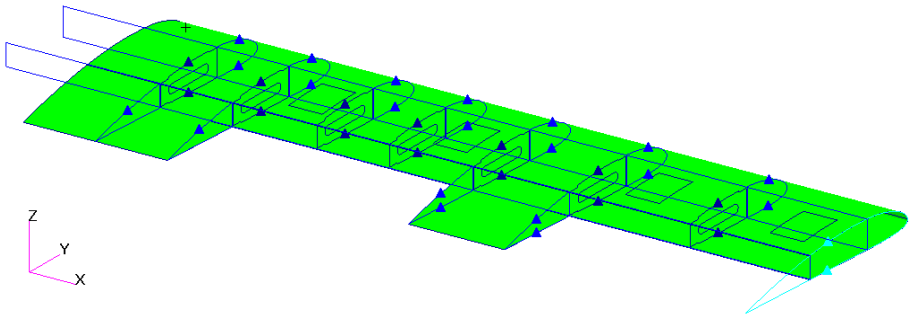

Figure 13: Geometric Associations Generate for Ruled Meshing at the Connection Locations of the Main Structural Parts

The second step was to create the mesh seeds along the associations obtained. The meshing will be fine and the element edge length was selected to be 1 centimeter. Figure 14 shows all the mesh seeds, which are given in yellow color, created for the ruled meshing.

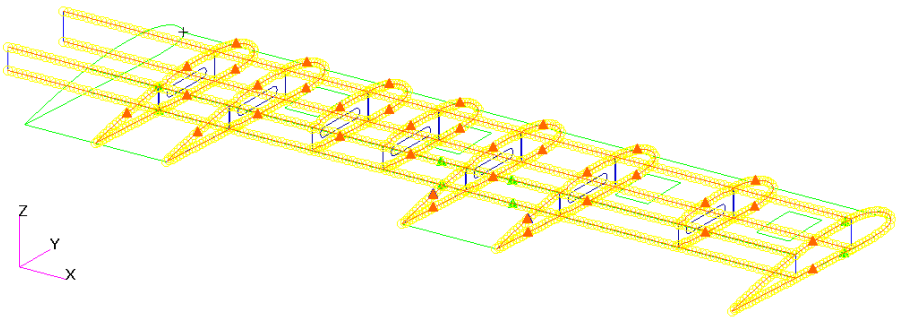

Figure 14: Mesh Seeds Generated for the Ruled Meshing of the Wing Torque Box Main Structural Members

The wing torque box main structure was then meshed by using the generated mesh seeds. The isometric view of the mesh generated is given in Figure 15. Additionally, Figure 16 shows the isometric view of the mesh on the spars with 3D

offset view of the flanges and Figure 17 shows the isometric view of the mesh at a unique rib segment.

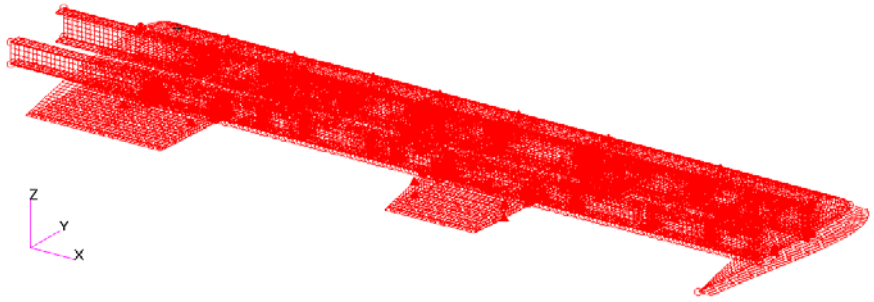

Figure 15: Isometric View of the Mesh Generated over Wing Torque Box Geometry

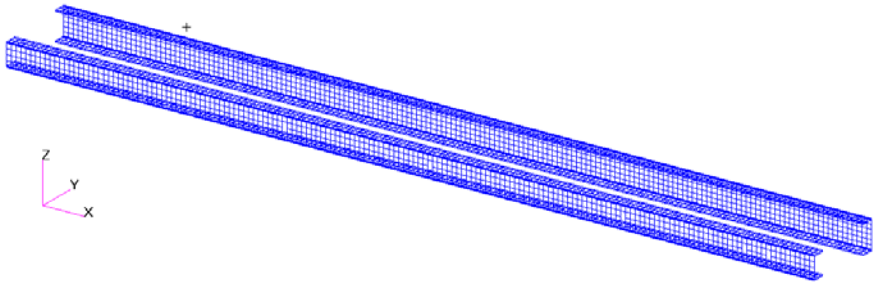

Figure 16: Isometric View of the Mesh on the Spars with the 3D Offset View of the Flanges

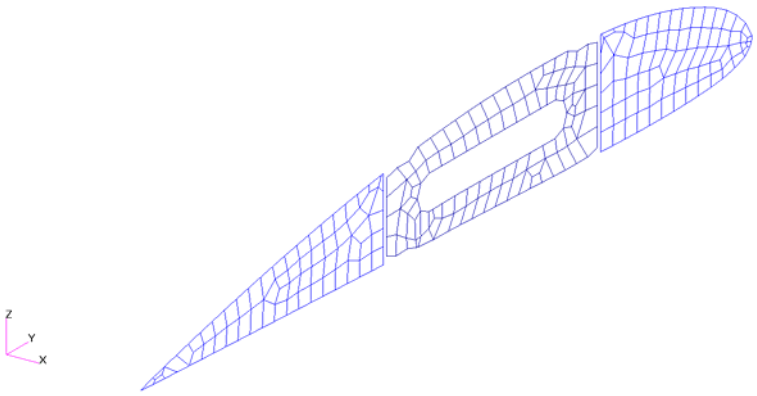

Figure 17: Isometric View of the Mesh on a Unique Rib Segment

4.6 Element Connections and the Details of the Finite Element Model

The scope of this section is to identify the details such as element connections, spar flange geometries and local stiffeners.

4.6.1 Connection between Skin and Wing Torque Box Inner Structure

In reality the connection between the fiber-reinforced composites and aluminum is done by using the elastomer adhesives. The mechanical properties of the adhesives depend on temperature and moisture levels as well as the curing time and pressure applied over the adhesive during curing [15]. In order to define the adhesive properties the wing has to be manufactured and the parts must be connected, and then some methodological experiments will show the exact properties. Since the structural analyses have to be done before the manufacturing; some engineering assumptions have to be made to represent the actual connection case [16].

Hence in the model, the skin and the ribs were connected by using the equivalence module; and the skin-spar connections on the other hand were modeled by using RBE2 type multi point constraints [13]. Figure 18 and Figure 19 gives examples of the skin-rib connection, and Figure 20 and Figure 21 illustrate the skin-spar connection. Altogether 604 RBE2 elements used to model the connection between spar and the skin of the wing torque box.

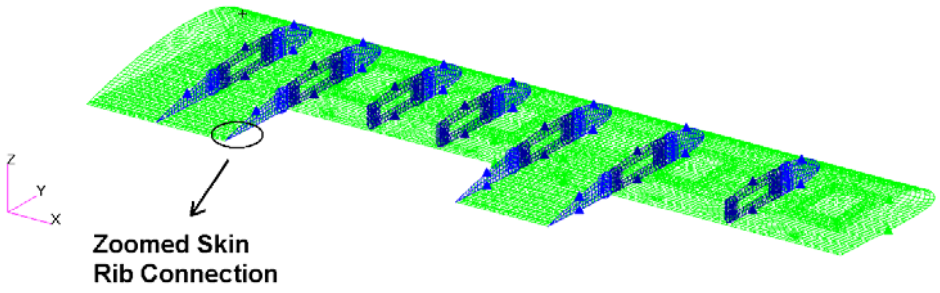

Figure 18: The Location of the Skin-Rib Connection Sample in Isometric View of the Wing Torque Box

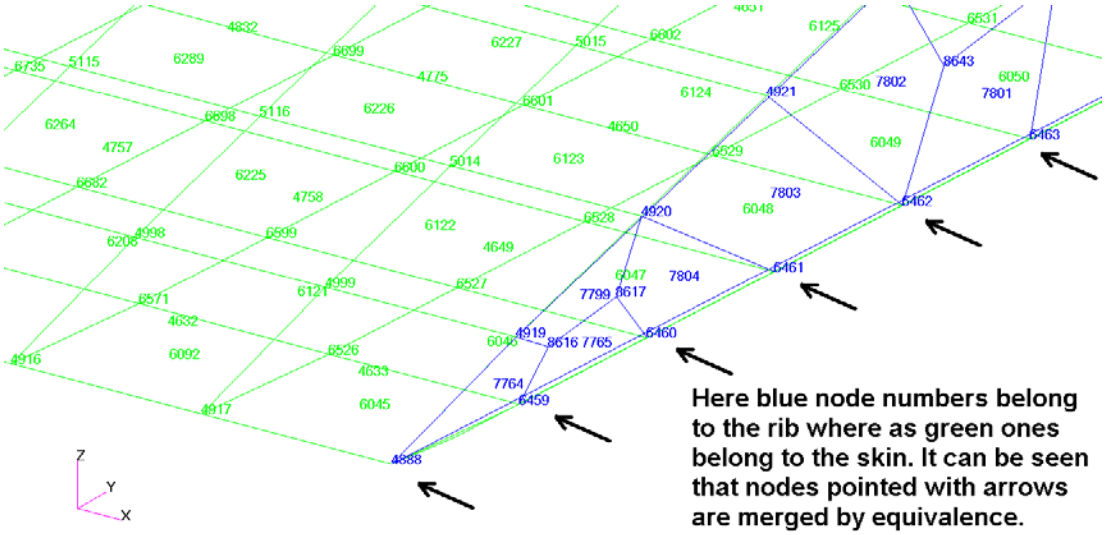

Figure 19: Zoomed Isometric View of Skin-Rib Connection Location of which is Shown at Figure 18

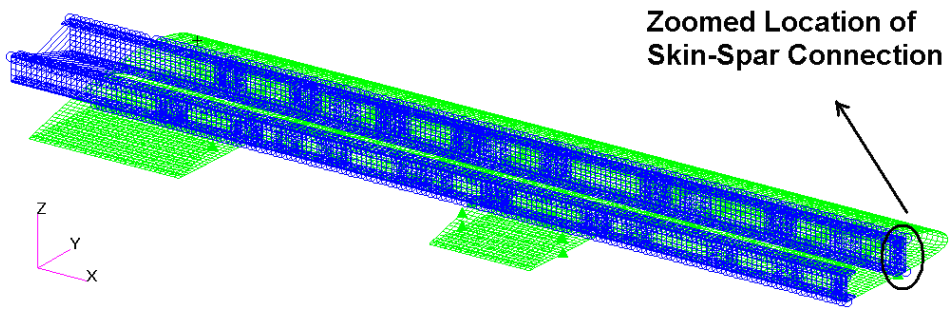

Figure 20: The Location of the Skin-Spar Connection Sample in Isometric View of the Wing Torque Box

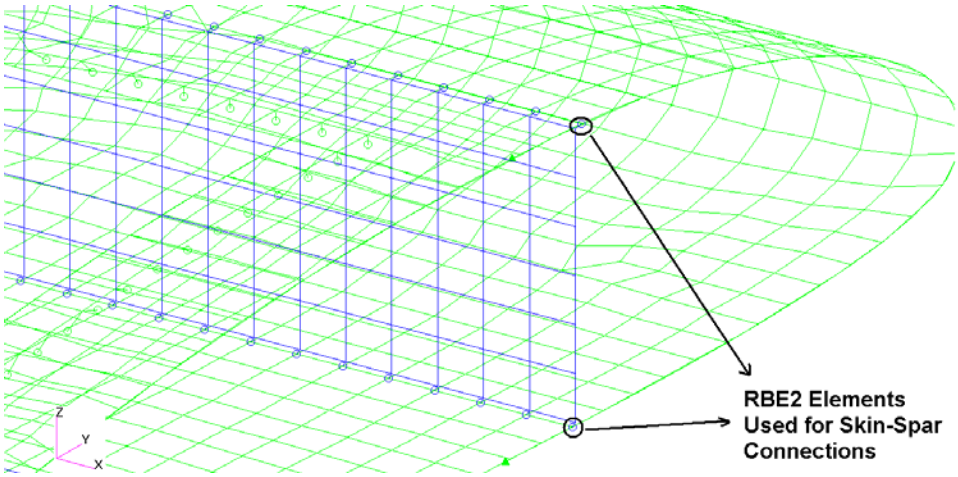

Figure 21: Zoomed Isometric View of Skin-Spar Connection Location of which is Shown at Figure 20

4.6.2 Connection between Spars and Ribs

The connections between the members of the inner structure of a wing torque box in practice were generally done by using the fittings and fasteners. The fittings were used to increase the stiffness at connection locations and the fasteners were utilized to connect the members.

In this study the fittings were selected as L-Section corner type connectors. A zoomed isometric view of a unique rib segment showing the geometry of the corner connectors can be viewed in Figure 22.

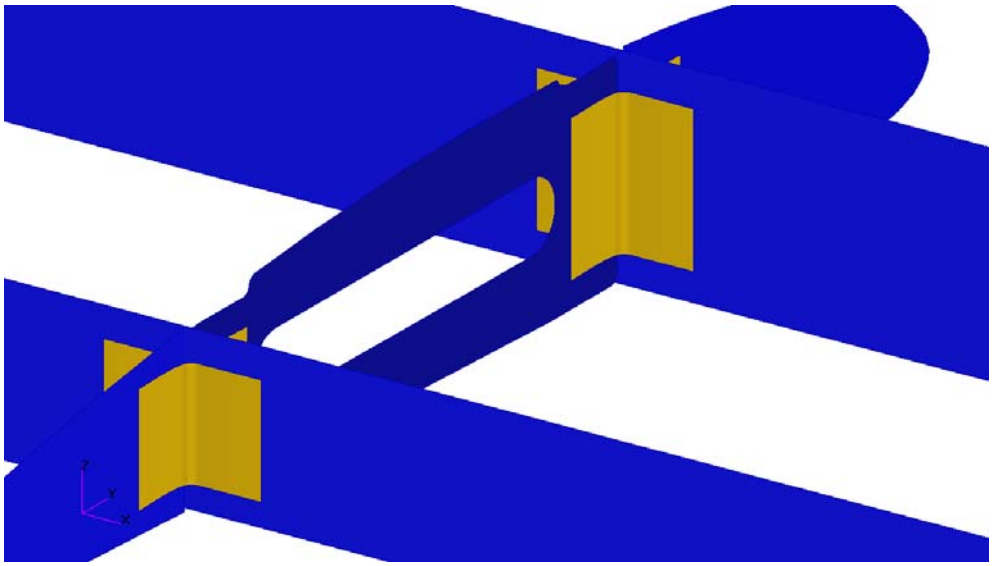

Figure 22: Zoomed Isometric View of Corner Connectors at a Unique Rib Segment of the Wing Torque Box

The fasteners for the connections were modeled by using RBE2 type multi point constraints. The connections were modeled as the fitting-rib connection of which a sample is shown in Figure 23. The total number of the RBE2 elements used for modeling of the connection of the spars and the ribs was 248.

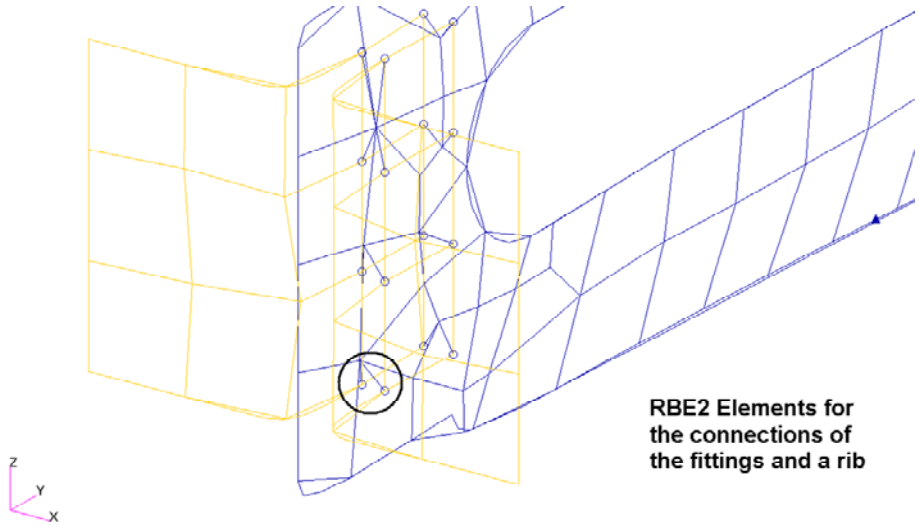

Figure 23: Zoomed Isometric View of a Sample Rib-Fitting Connection by the Utilization of RBE2 Elements

4.7 Finite Element Model Details

In the model developed, 17537 nodes resulted in 79509 degrees of freedom exist including all the restrictions. Table 10 details the information about the number of element types, element topology, and total number of multi point constraints used in the generated finite element model.

Table 10: Element Summary of the Generated Finite Element Model

Element Type	Element Topology	Total Used in the Model
1D Beam	Bar2	668
2D Shell	Quad4	16210
2D Shell	Tria3	33
MPC	RBE2	1442

4.8 Application of the Boundary Conditions

The model developed in this chapter will be manufactured and subjected to ground vibration tests. For the ground vibration tests a test bench was designed and externally manufactured. APPENDIX B gives the details of the test bench. The boundaries of the fixture were taken as the boundary conditions of the model. This was satisfied by fixing all six degrees of freedom on the nodes corresponding to the test fixture. Figure 24 shows the zoomed isometric view of the boundary.

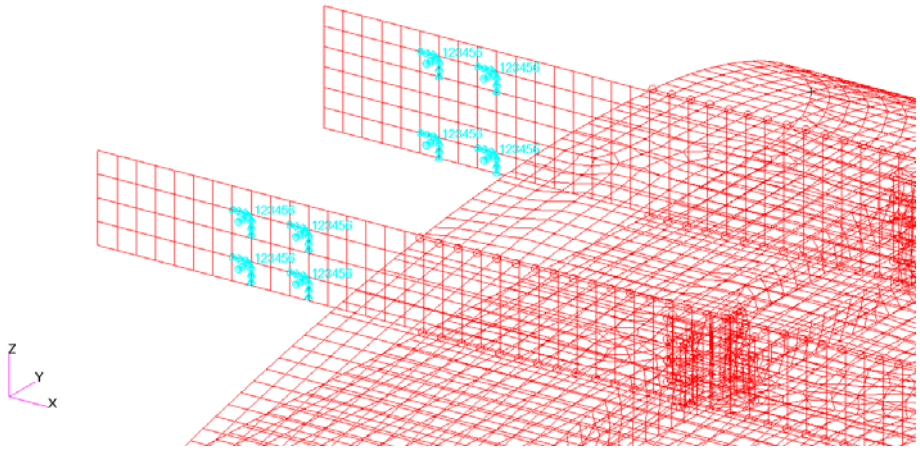

Figure 24: Boundary Conditions Applied on the Wing Torque Box for Structural Analyses

4.9 Discussions

The scope of this chapter was to give a description of the finite element model developed. The finite element model described in detail in this chapter will be referred to Model 1 throughout the rest of the study.

CHAPTER 5

STRUCTURAL ANALYSIS OF THE MISSION ADAPTIVE WING

5.1 Introduction

The structural analysis of the designed wing will be conducted by using the Finite Element Method and MSC®/NASTRAN Package program. This chapter describes dynamic and the static analyses of the wing torque box designed. It further represents the buckling characteristics of the composite skin. The relevant results were also given.

5.2 Dynamic Analyses of the Wing Torque Box and Results

The primary parameter that the design of the wing built on was high rigidity requirement of the mission-adaptive control surfaces. The best parameter to examine stiffness characteristics of the structure was considered to be the first out-of-plane bending natural frequency. Therefore, the most important analyses to be done is the natural frequency analysis, which will eventually show that the stiffness characteristic of the structure. The results given here will show the first natural frequencies of all three types of global mode shapes of the wing which are out-of-plane bending, in-plane bending and torsion. In addition to these the natural frequency corresponding to second out-of-plane natural will also be shown in order to examine the further dynamic characteristics of the structure.

The dynamic analysis of the developed wing model, Model 1, was conducted by using the solver 103 module of MSC®/ NASTRAN package program. Table 11

shows the first four natural frequencies and the corresponding global mode shapes. Figure 25 to the Figure 28 give the relevant global mode shapes of Model 1.

Table 11: Natural Frequency and Mode Shape Analysis Results Based on Model 1 Using Finite Element Method

Global Mode Shape	Natural Frequency Value [Hz.]
1. Out-of-plane Bending	17.29
1. In-plane Bending	56.42
1. Torsion	63.16
2. Out-of-plane Bending	106.67

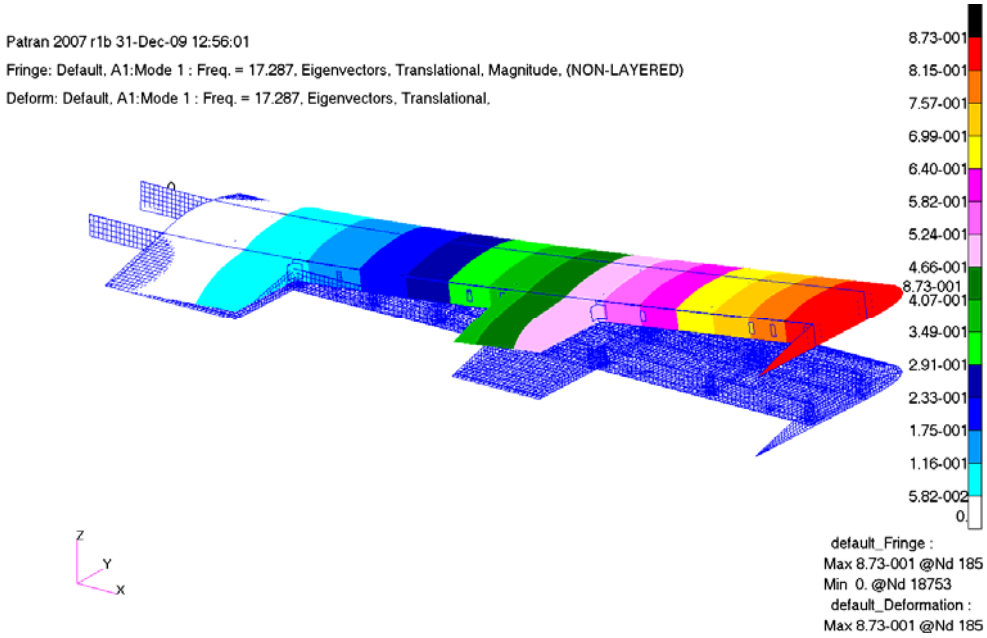

Figure 25: First Out-of-plane Bending Mode Shape of Model 1 [17.287 Hz]

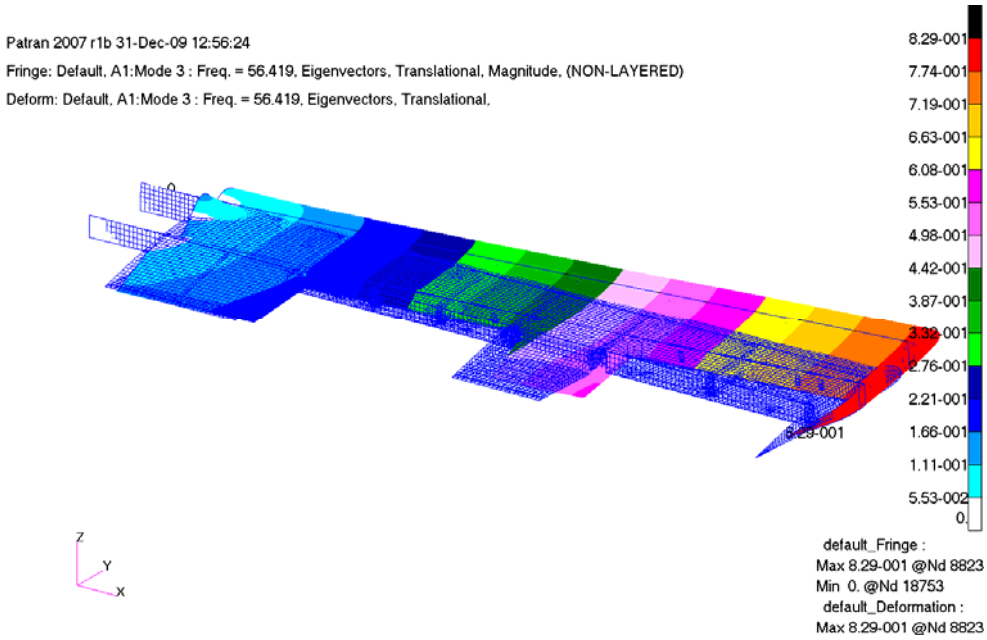

Figure 26: First In-plane Bending Mode Shape of Model 1 [56.419 Hz]

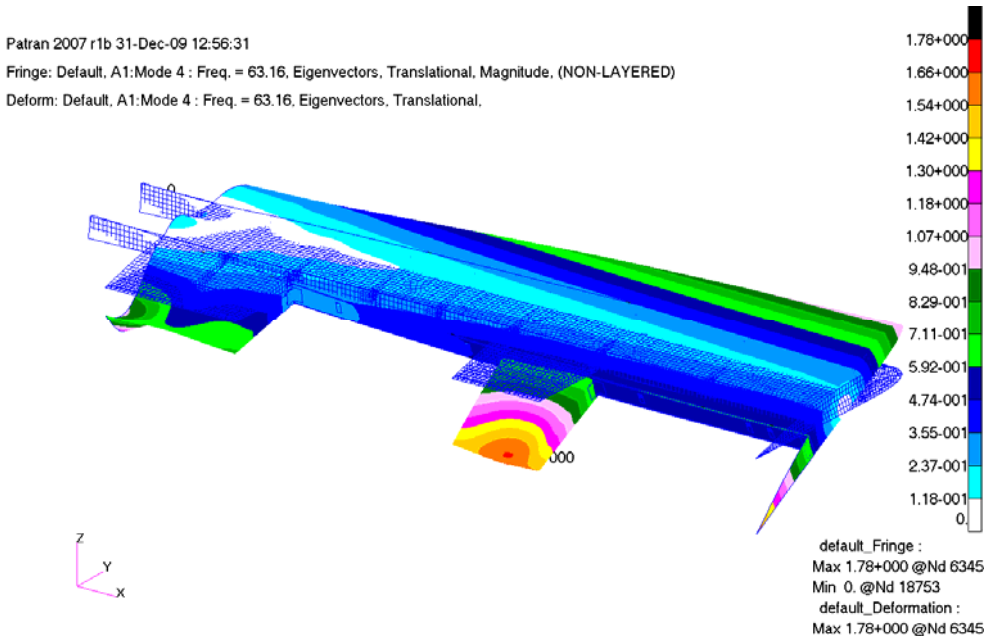

Figure 27: First Torsion Mode Shape of Model 1 [63.16 Hz]

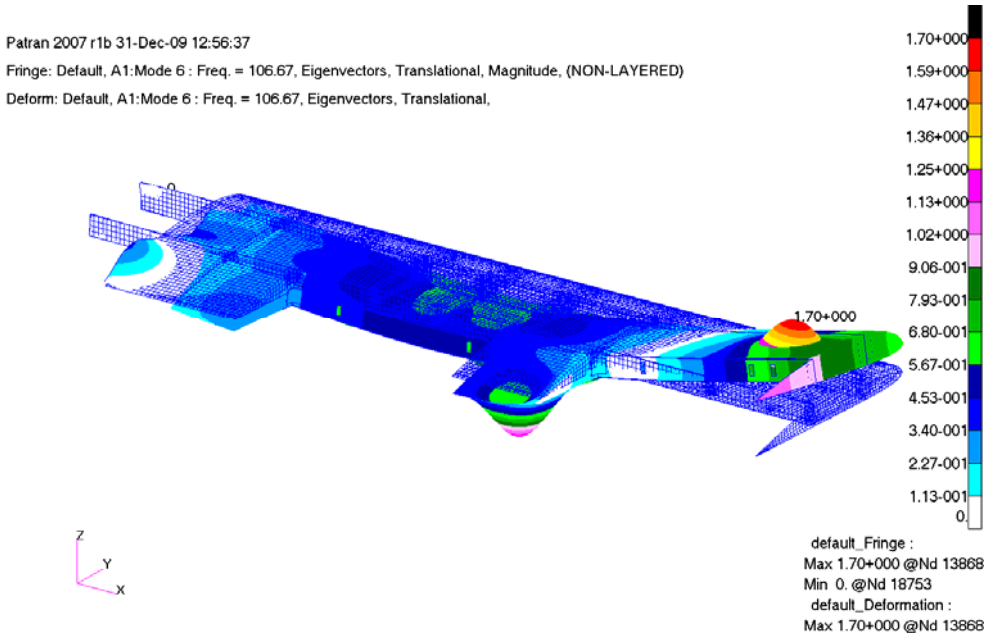

Figure 28: Second Out-of-plane Bending Mode Shape of Model 1 [106.67 Hz]

5.3 Static Analyses of the Wing Torque Box and Results

The static analyses within the scope of this study were conducted in three groups divided in terms of the loadings applied. First one was the loading of the wing torque box under its own weight in in-vacuo condition. The second loading was the aerodynamic loading under cruise conditions. Finally, the third loading was the maximum load factor maneuver loading. The main target of the analyses will be the stress distribution of the internal structure.

5.3.1 Wing Torque Box under Its Own Weight

The method in order to model this type of loading was to create an inertial acceleration field which was the equivalent of the gravitational acceleration of 9.81 [m/s^2]. Figure 29 shows the inertial field created on the Model 1.

Figure 29: Loading of the Wing under its Own Weight by Using Gravitational Acceleration Field

The static analyses were conducted by using the solver 101 module of MSC®/ NASTRAN package program. Figure 30 shows the displacement field of the wing torque box under its own weight. The maximum displacement of 1.3 [mm] occurred at the tip of the wing torque box. Figure 31 and Figure 32 show the stress distribution on the internal structure and the maximum stress location respectively. The maximum stress value reached at the boundary of the main spar was found as 9.87 [MPa]. Comparing this value with the yield strength of Aluminum 7075-T651, which was given at Table 6 as 503 [MPa], it was understood that the wing is far safe with a large margin of safety value of 51.

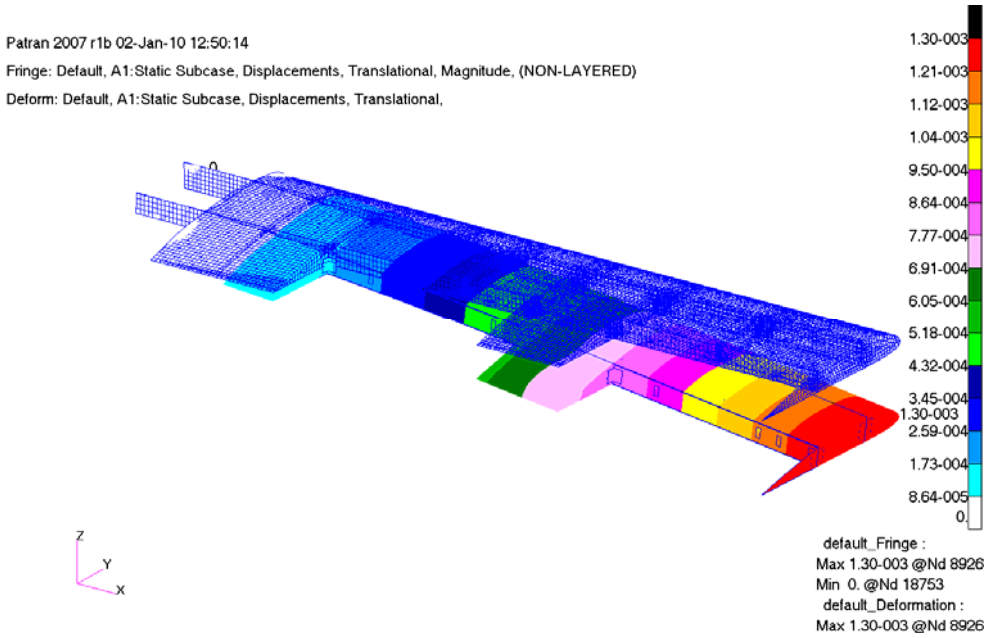

Figure 30: Displacement Field of the Wing Torque Box under Its Own Weight

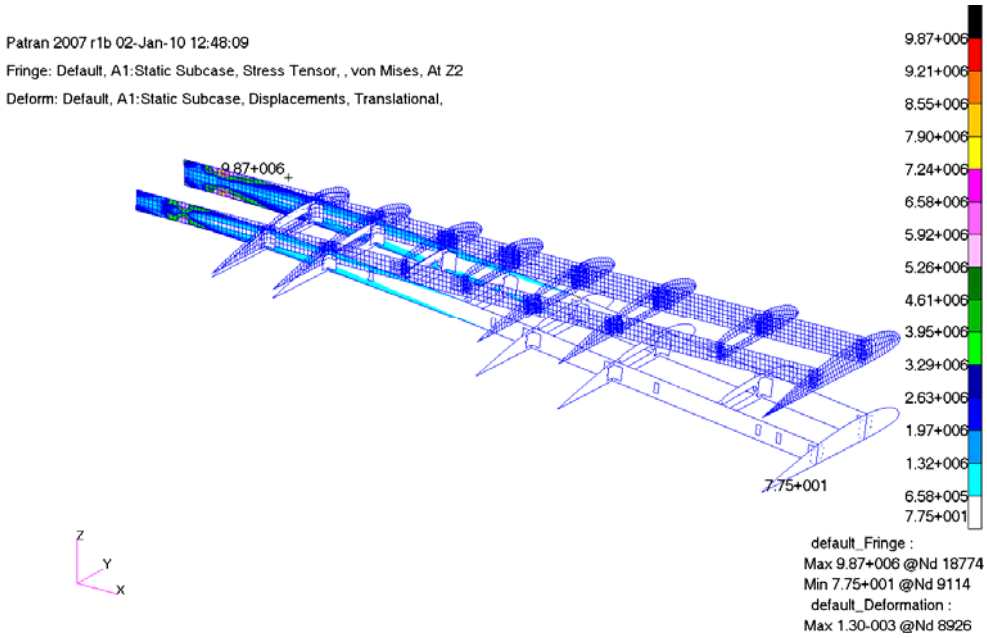

Figure 31: Stress Distribution on the Wing Torque Box Internal Structure under Its Own Weight

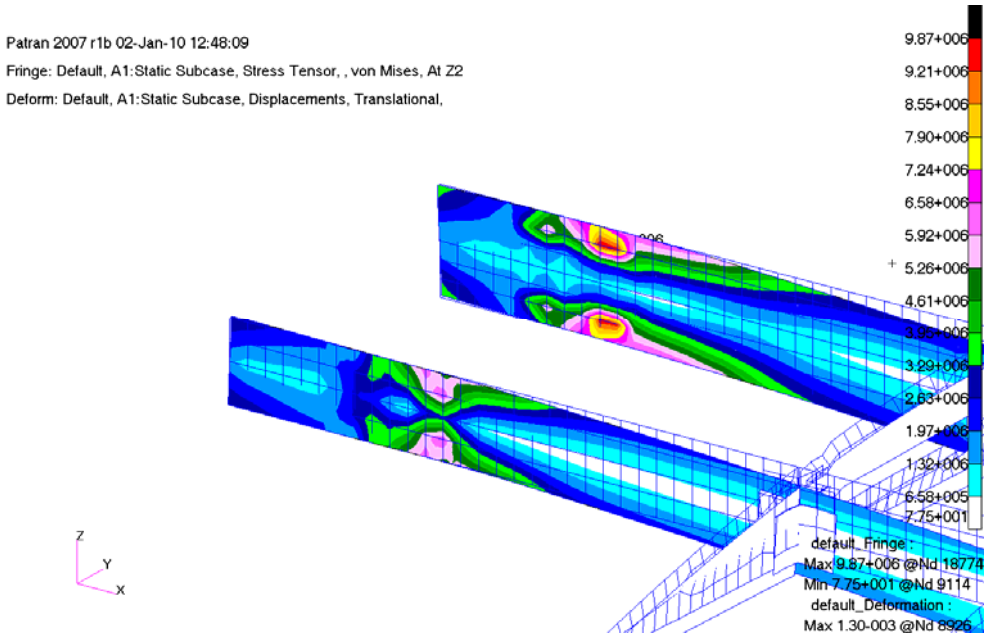

Figure 32: Zoomed View of the Maximum Stress Location at the Main Spar Boundary under Its Own Weight

5.3.2 Wing Torque Box under Aerodynamic Loading

The aerodynamic loading under the cruise conditions can simply be defined with the Eqn. 5.1 shown below [17].

$$L = W \qquad \text{(Eqn. 5.1)}$$

The take off gross weight of the unmanned aerial vehicle was estimated to be around 440 [N], and approximately half of this weight would be carried by each wing assuming that the tail and fuselage had negligible lifting effect. There are several ways to simulate this loading in finite element method. Regarding the possibility of buckling was decided to simulate the loading with the help of 2D Panel Method [18]. The solver utilized was an in-house developed steady potential flow solver for airfoil sections using low-order panel method algorithm. Figure 33 gives the actual normalized chordwise pressure coefficient distribution data over NACA 4412 airfoil section for 100 panels.

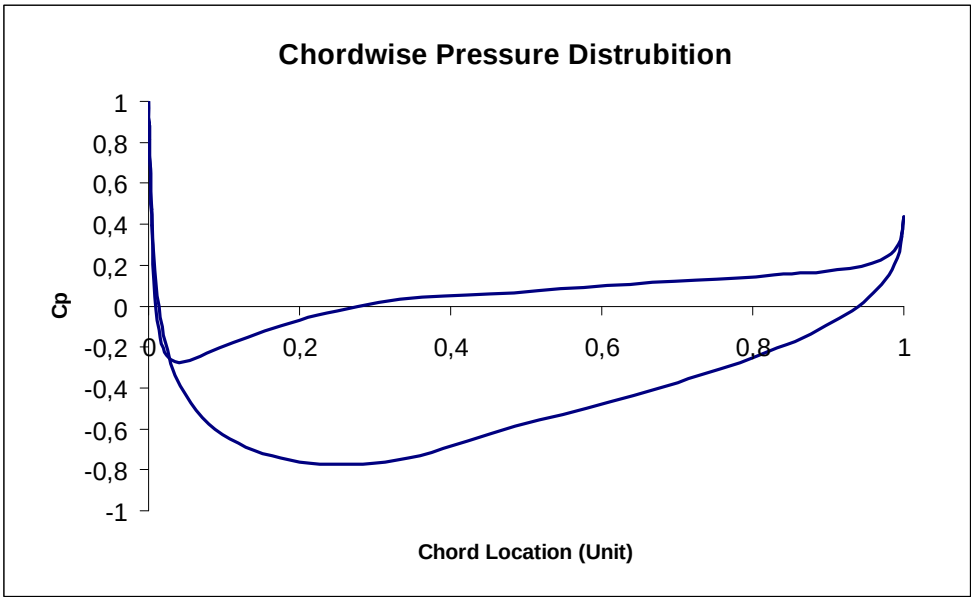

Figure 33: Chordwise Normalized Pressure Distribution over NACA 4412 Airfoil Section Having Unit Chord Length

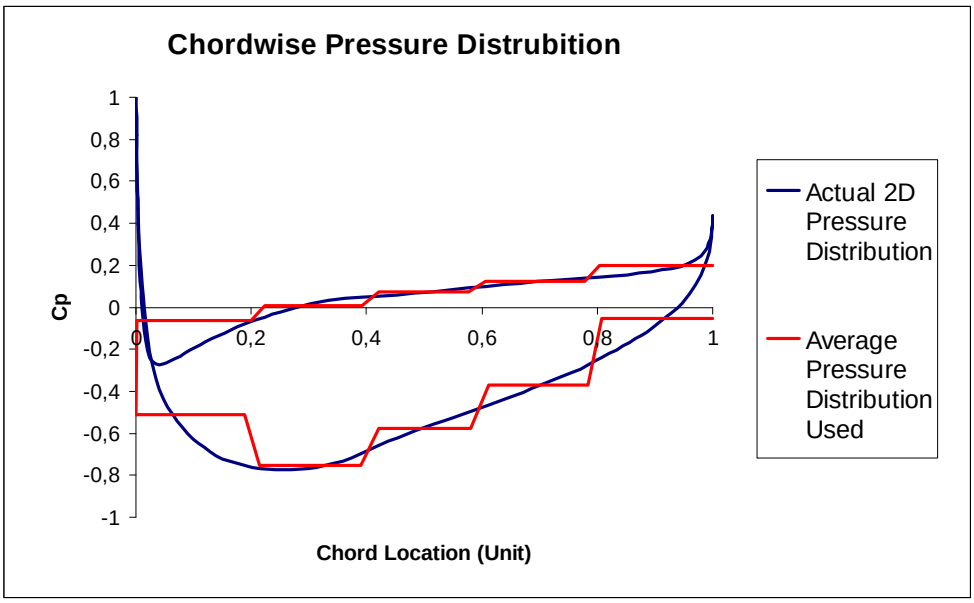

Figure 34: Average Chordwise Pressure Coefficient Distribution Used in Finite Element Modeling of the Aerodynamic Loading

It can be seen from Figure 34 that the upper and the lower skin was divided in the chord direction into 5 equal length segments to simulate the pressure distribution in the finite element model.

The second variation of the aerodynamic pressure was a spanwise variation. For a rectangular wing having the moderate aspect ratio this distribution can be assumed as an elliptic distribution [18]. For the spanwise variation of the aerodynamic pressure the span of the wing was divided into 10 equal length segments. Figure 35 illustrates the simulated spanwise pressure distribution.

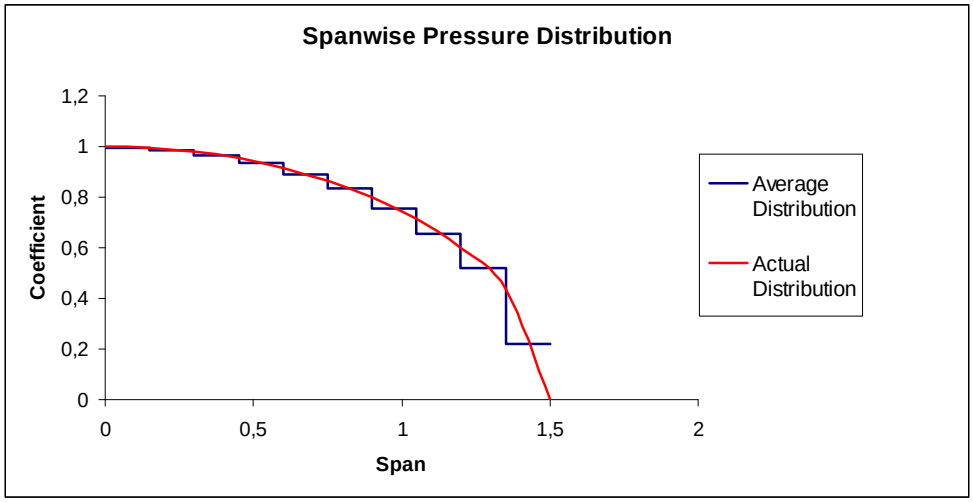

Figure 35: Spanwise Normalized Aerodynamic Pressure Distribution Coefficient Used in Finite Element Modeling

The normalized values of the modeled panel pressures were converted to the actual pressure values by multiplying them with the static pressure of the still air, which is 101.3 [KPa]. The pressure field was applied on the wing segments shown in Figure 36. Table 12 gives the pressure magnitudes applied on the upper and lower skins of the segments shown Figure 36. The pressure inside the wing was assumed to be equal to the atmospheric pressure at the sea level. This value was needed by the software used for the structural modeling as an input.

1	6	11	16	21	26	31	36	41	46
2	7	12	17	22	27	32	37	42	47
3	8	13	18	23	28	33	38	43	48
4	9	14	19	24	29	34	39	44	49
5	10	15	20	25	30	35	40	45	50

Chord

Span

Figure 36: Pressure Segments on the Wing Used for the Simulation of Aerodynamic Loading in the Finite Element Modeling

Table 12: Segmented Skin Gage Pressure Values in Magnitude

Panel Number	Upper Skin Gage Pressure [Pa]	Lower Skin Gage Pressure [Pa]
1	515.64	66.03
2	760.03	9.86
3	581.00	72.68
4	375.10	121.92
5	54.09	201.52
6	510.42	65.36
7	752.33	9.76
8	575.11	71.94
9	371.30	120.68
10	53.54	199.48
11	499.81	64.01
12	736.69	9.56
13	563.16	70.44
14	363.58	118.18
15	52.43	195.34
16	483.45	61.91
17	712.58	9.25
18	544.73	68.14
19	351.68	114.31
20	50.71	188.95
21	460.73	59.00

Table 12: Segmented Skin Gage Pressure Values in Magnitude

Panel Number	Upper Skin Gage Pressure [Pa]	Lower Skin Gage Pressure [Pa]
22	679.09	8.81
23	519.13	64.94
24	335.15	108.94
25	48.33	180.06
26	430.61	55.15
27	634.70	8.24
28	485.20	60.69
29	313.25	101.82
30	45.17	168.29
31	391.36	50.12
32	576.84	7.49
33	440.96	55.16
34	284.69	92.53
35	41.05	152.95
36	339.66	43.50
37	500.65	6.50
38	382.72	47.87
39	247.09	80.31
40	35.63	132.75
41	267.74	34.29
42	394.64	5.12

Table 12: Segmented Skin Gage Pressure Values in Magnitude

Panel Number	Upper Skin Gage Pressure [Pa]	Lower Skin Gage Pressure [Pa]
43	301.68	37.74
44	194.77	63.31
45	28.09	104.64
46	112.66	14.43
47	166.06	2.16
48	126.94	15.88
49	81.96	26.64
50	11.82	44.03

Some of the pressures given in Table 12 belong to the control surfaces. Since the model analyzed did not include the control surfaces, the effects of loads at these segments were simulated in finite element model in a different manner. They were simulated as if they were distributed forces and couples, due to the resultant pressure on them, on upper and lower flanges of the secondary spar. Table 13 gives the distributed couples applied on the secondary spar flanges.

Table 13: The Magnitudes of the Forces and Couples Applied on the Secondary Spar Flanges to Simulate the Pressure on the Control Surfaces (Forces are in [N/m] and all Moments are in [N.m/m])

Segment	Load Type	Lower Flange Loads	Upper Flange Loads
14-15	Force	41.6	31.3
14-15	Moment	2.6	3.5
19-20	Force	40.3	30.3
19-20	Moment	2.5	3.4
24-25	Force	38.3	28.9
24-25	Moment	2.4	3.3
29-30	Force	35.8	27.0
29-30	Moment	2.2	3.0
34-35	Force	32.6	24.6
34-35	Moment	2.0	2.8
39-40	Force	28.3	21.3
39-40	Moment	1.8	2.4
44-45	Force	22.3	16.8
44-45	Moment	1.4	1.9
49-50	Force	9.4	7.1
49-50	Moment	0.6	0.8

The inertial loads on the wing due to the gravitational field were also added to the computed aerodynamic load field. Table 14 gives the resultant loading on the Model 1. It can be seen that the aerodynamic force at z-direction is equal to 216.3

[N] which was approximately equal to the half of the estimate weight (220 [N]) of the unmanned aerial vehicle.

Table 14: Total Resultant Loading on the Structure due to Aerodynamic and Inertial Loading during Level Flight Cruise Conditions

Loading Type	Direction	Force [N]	Moment [N.m]
Aerodynamic Load	X	0.0	-34.3
	Y	-2.3	-137.0
	Z	216.3	-2.3
Inertial Load Due to Gravity	X	0	10.7
	Y	0	35.1
	Z	-51.2	0.0
Total	X	0.0	-23.6
	Y	-2.3	-101.9
	Z	165.1	-2.3

Figure 37 gives the displacement field on the wing torque box under aerodynamic loading during cruise conditions. The maximum tip displacement was found to be 3.71 [mm]. Figure 38 and Figure 39 show the stress distribution on the internal structure of the wing torque box and the zoomed view of the maximum stress location respectively. It can be seen from Figure 39 that the maximum stress value is 32.4 [MPa], which is still very low as compared to the material yield strength of 503 [MPa].

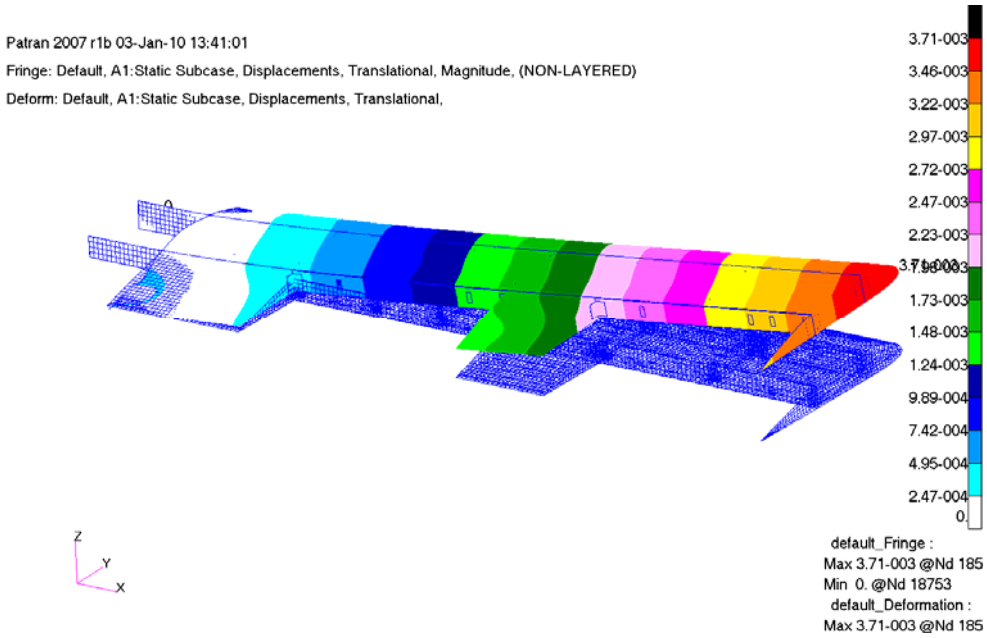

Figure 37: Displacement Field of the Wing Torque Box under the Loading due to Level Flight Cruise Conditions

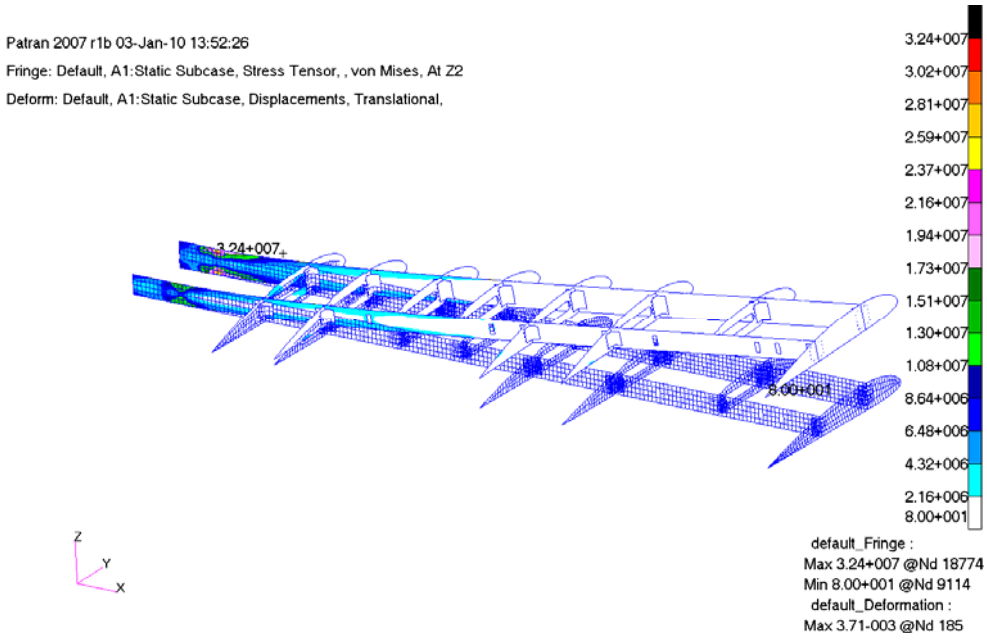

Figure 38: Stress Distribution on the Internal Structure of the Wing Torque Box under the Loading due to Level Flight Cruise Conditions

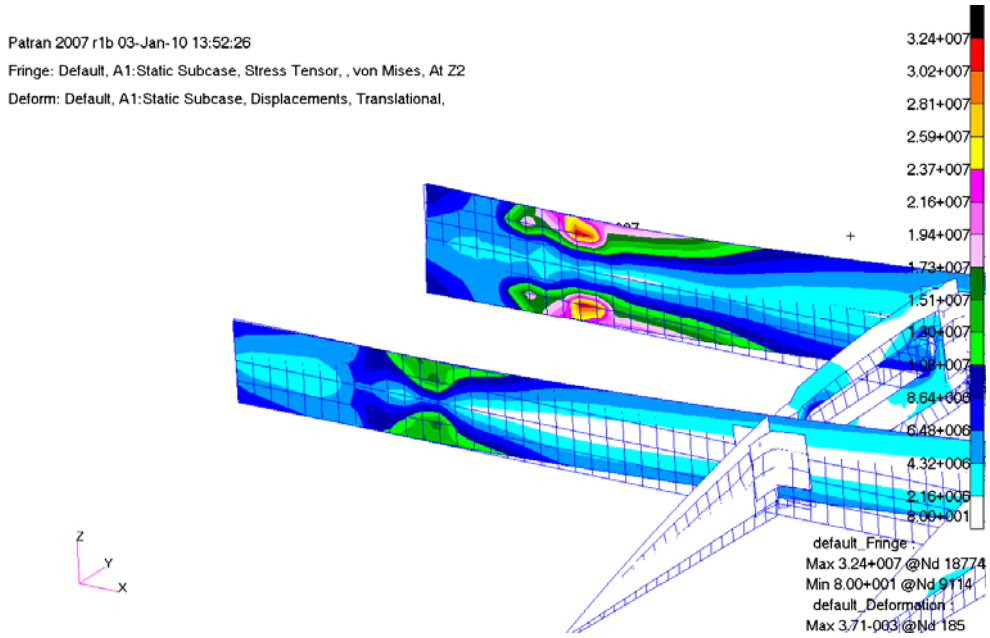

Figure 39: Zoomed View of the Maximum Stress Location at the Main Spar Boundary Condition under the Loading due to Level Flight Cruise Conditions

5.3.3 Wing Torque Box under the Loading due to the Maximum Load Factor Maneuver

The design maximum load factor of the wing was determined to be 5 and the condition is given in Equation 5.2 [17].

$$n = \frac{L}{W} \qquad \text{(Eqn. 5.2)}$$

The pull-down maneuver shown in Figure 40 [17] with 5g was selected as a case with excessive load to be examined.

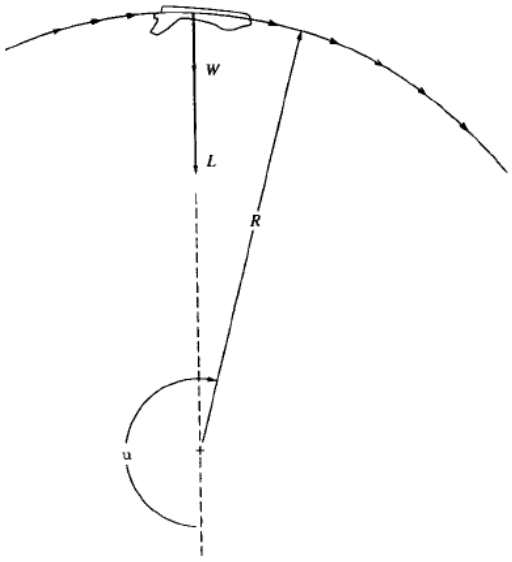

Figure 40: The Pull-down Maneuver [17]

During the pull-down maneuver the aerodynamic loads as well as the inertial loads due to the gravitational field are carried by the wing. In other words the wings' own weight will be in the same direction with the lifting force. Hence, the loading simulated on Model 1 for this case was the five times the pressures and loads given in Table 12 and Table 13 addition to its own weight. Table 15 gives the resultant loading for the case of the maximum load factor pull-down maneuver. It can be seen that the resultant aerodynamic force in z-direction is equal to 1081.3 [N], which is approximately equal to the half of the five times of the weight of the vehicle (1100 [N]).

Table 15: Total Resultant Loading on the Structure due to the Aerodynamic and Inertial Loading during a Pull-down Maneuver with Maximum Load Factor

Loading Type	Direction	Force [N]	Moment [N.m]
Aerodynamic Load	X	0.0	-168.3
	Y	-11.6	-684.9
	Z	1081.3	-11.3
Inertial Load Due to Gravity	X	0.0	-10.7
	Y	0.0	-35.1
	Z	51.2	0.0
Total	X	0.0	-179.0
	Y	-11.6	-720.0
	Z	1132.5	-11.3

Figure 41 shows the displacement field of the wing torque box during the pull-down maneuver with a maximum load factor of 5. The maximum displacement was again determined at the tip as 26.3 [mm]. Figure 42 and Figure 43 show the stress distribution over the internal structure of the wing torque box and the zoomed view of the maximum stress location at the main spar boundary respectively.

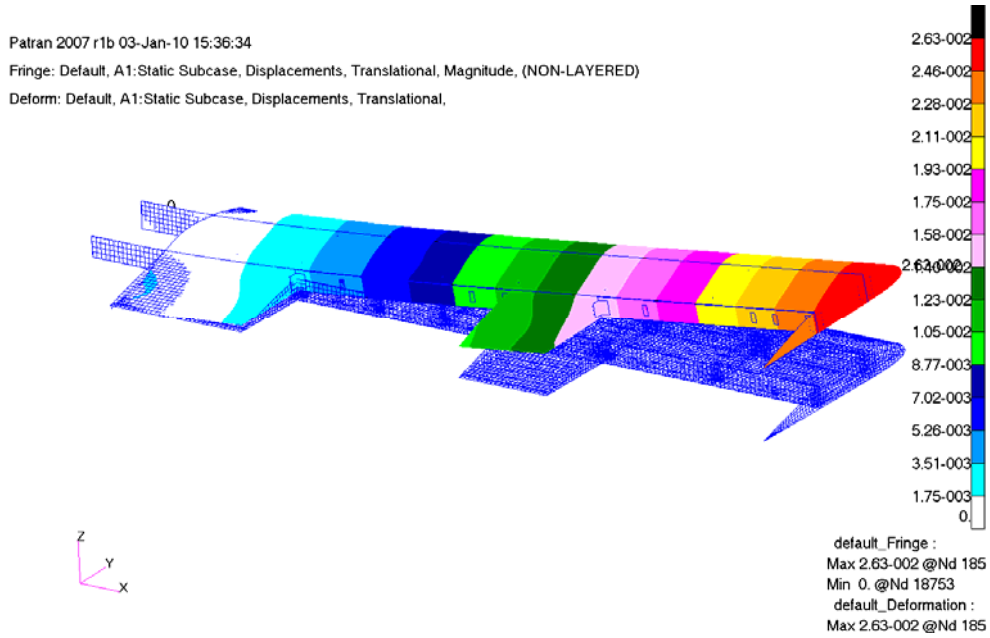

Figure 41: Displacement Field of the Wing Torque Box Due to the Loading at Pull-Down Maneuver with Maximum Load Factor of 5

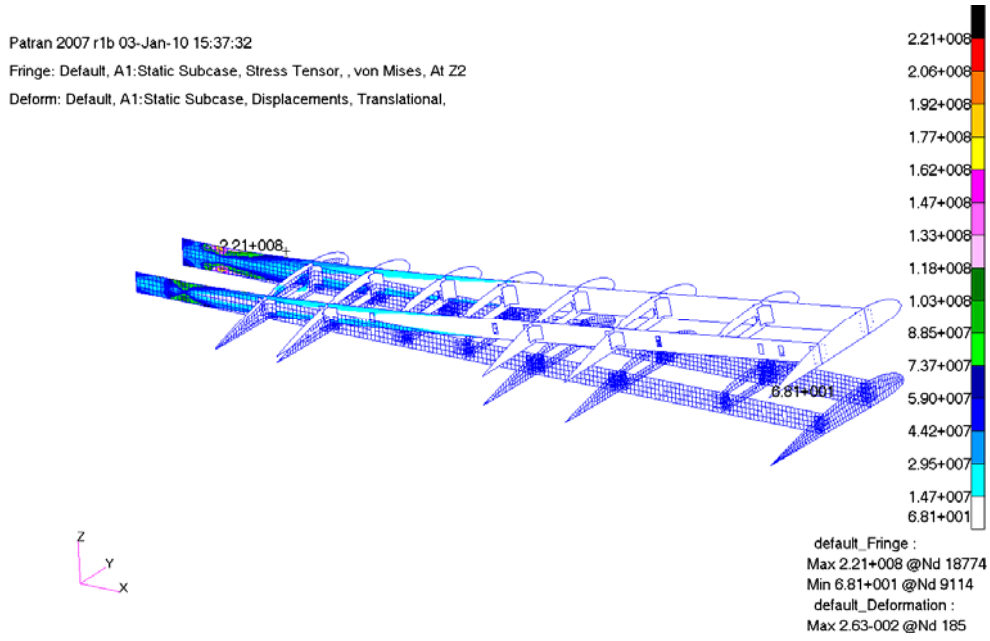

Figure 42: Stress Distribution on the Internal Structure of the Wing Torque Box under the Loading due to Pull-down Maneuver with Maximum Load Factor of 5

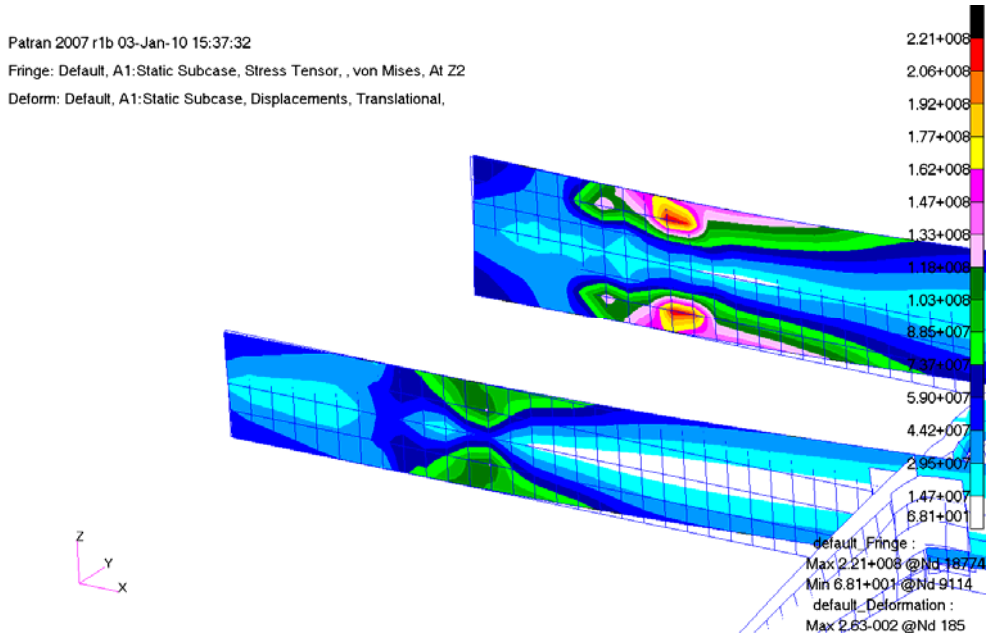

Figure 43: Zoomed View of the Maximum Stress Location at the Main Spar Boundary Condition under the Loading due to Pull-down Maneuver with Maximum Load Factor of 5

The maximum stress value of 221 [MPa], which occurred at the boundary of the main spar, was still below the material yield strength of 503 [MPa]. The corresponding margin of safety was determined to be 2.27.

5.4 Buckling Analysis of the Skin of the Wing Torque Box and Results

Panel buckling of the aircraft wing skin is a frequent problem in the aircraft structures. The buckling of the skin does not result in a catastrophic failure; however, the resultant deformations change the aerodynamic characteristics of the wing which may even cause the stall of the wing in the worst case scenario.

The buckling characteristics of the wing torque box were examined for only the designated maximum loading case which occurs at the pull-down maneuver with a load factor of 5 for the designed wing. The loading would be the same with the loading case of Section 5.3.3, however an update on the model was done. This update was required by the buckling solver module of MSC®/NASTRAN package

program because of the fact that the program can only work if there is no offset defined on the elements. Hence, the offsets of the spar flanges were removed and an updated model was run. The buckling analyses were conducted by using the solver 105 module of MSC®/ NASTRAN package program.

The buckling solver of MSC®/ NASTRAN gives the results in terms of translational eigenvectors of the elements and a factor [13].

$$Buckling\ Factor = \frac{Critical\ Buckling\ Load}{Actual\ Load\ on\ the\ Element} \qquad \text{(Eqn. 5.3)}$$

This factor, which is greater than 1 in magnitude, is always a negative number which indicates that the buckling phenomenon only occurs under compressive loading.

Figure 44 shows the translational eigenvector representation of the wing torque box under the loading due to the pull-down maneuver. The buckling factor of this loading is -1.48 which means that there would be no buckling on any skin panel even for the designated maximum loading case.

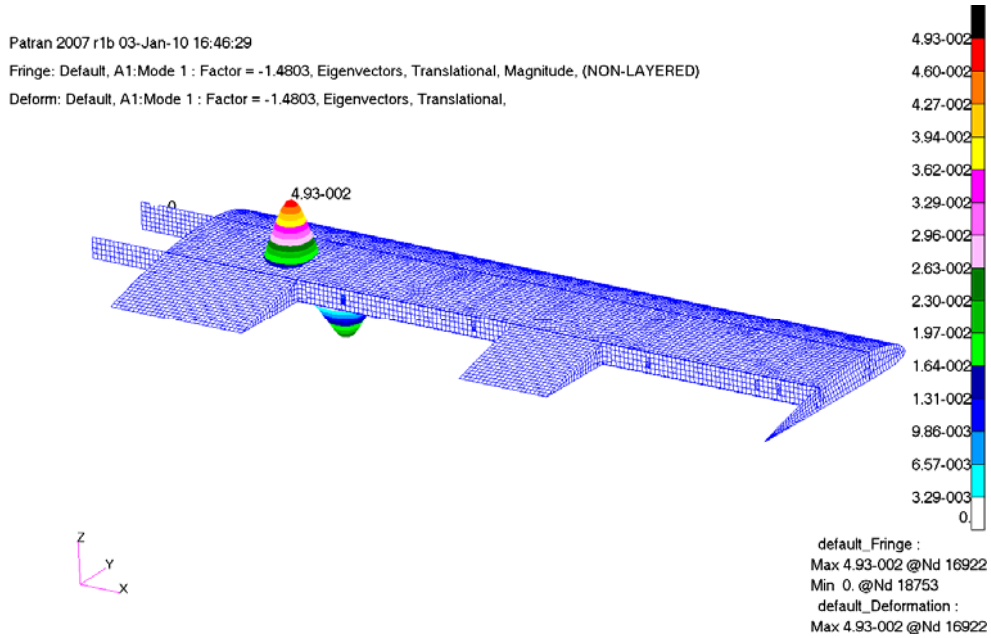

Figure 44: Translational Eigenvectors Representation of the Buckling Analysis Results under Loading due to Pull-down Maneuver with Maximum Load Factor of 5

5.5 Discussion

The wing torque box designed was structurally analyzed in this chapter. The dynamic and static analyses of the wing were conducted by using a commercial Finite Element package program. The skin buckling analysis was also done by the help of the same package program. It was observed from the results that the designed wing torque box can sustain each and every loading studied.

CHAPTER 6

MANUFACTURE OF A MISSION ADAPTIVE WING

6.1 Introduction

The mission adaptive wing structurally designed and structurally analyzed in Chapters 4 and 5 was manufactured by Turkish Aerospace Industries Inc. (TUSAŞ-TAI). The manufactured wing will be used for the ground vibration tests. The materials of the structural members of the wing torque box have already been decided and/or selected in Chapter 4 and the thicknesses and the cross-sections of the members were finalized after structural analyses in Chapter 5. Although the primary scope of this chapter is to illustrate the manufacturing process of the mission adaptive wing; the chapter also details some modifications to the original design because of the production requirements.

6.2 Manufacturing Process

6.2.1 The Spars

The spars of the wing were decided to be manufactured from Aluminum 7075-T651 material. This series of aluminum is specially developed for aerospace industry and has high ultimate and yield strength values. Nonetheless, this series of aluminum is also brittle and its hardness value is high. Hence, manufacturing the spars having relatively large thickness with the help of metal forming methods was nearly impossible. After the consultation with manufacturer team it was discovered that the extrusion profiles of 7075-T651 with various geometries were available at

the storage. There were two profiles found at the inventory to fit the geometrical properties selected at design stage and hence they were decided to be used in the production. The chosen cross-sectional profiles of the main spar and the secondary spar are given in Figure 45 and Figure 46 respectively.

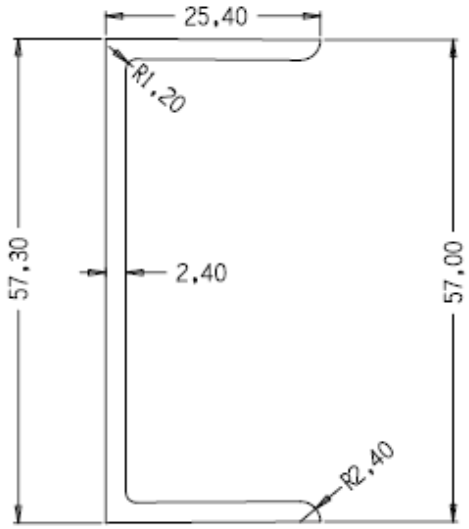

Figure 45: Cross-Sectional View of the Main Spar Extrusion Profile [mm]

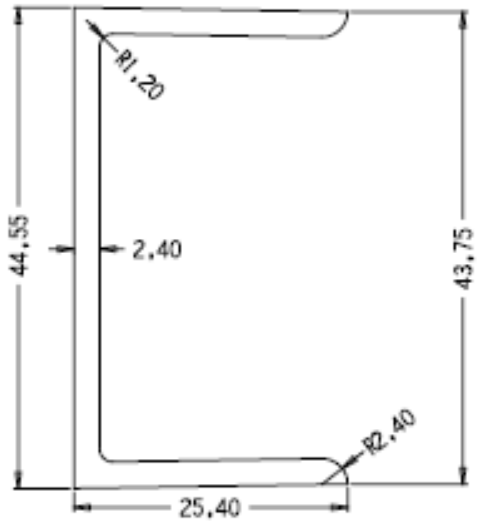

Figure 46: Cross-Sectional View of the Secondary Spar Extrusion Profile [mm]

6.2.2 The Ribs

The ribs were produced from Aluminum 2024-T3 with a thickness of 0.8 [mm]. The production was done by using a 2-Axis CNC bench. In order to do this the numerical coordinate frames for each rib to be used in CNC bench were created by utilizing a Computer Aided Design (CAD) tool Kubotek/KeyCreator [19]. Figure 47, Figure 48 and Figure 49 are the CAD models of the rib portions being, the portion at the leading edge, the portion between the main and secondary spars and the portion at the trailing edge in order.

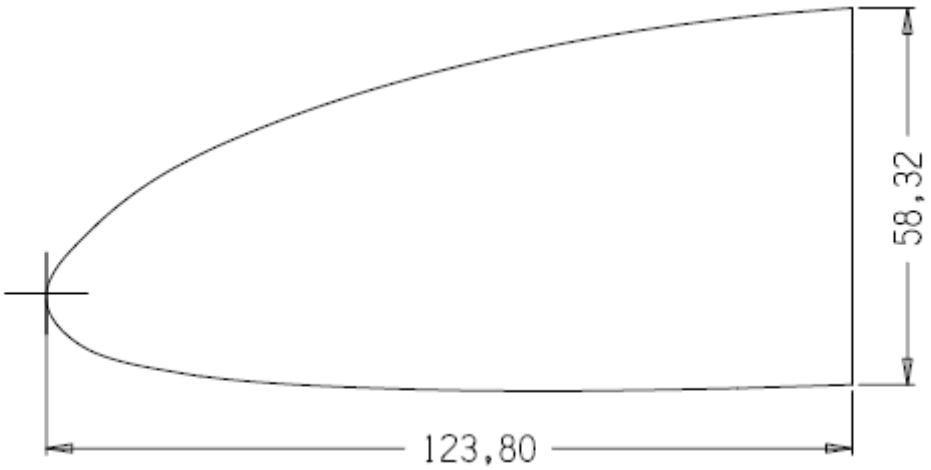

Figure 47: 2D View of the Rib Portion Located at the Leading Edge [mm]

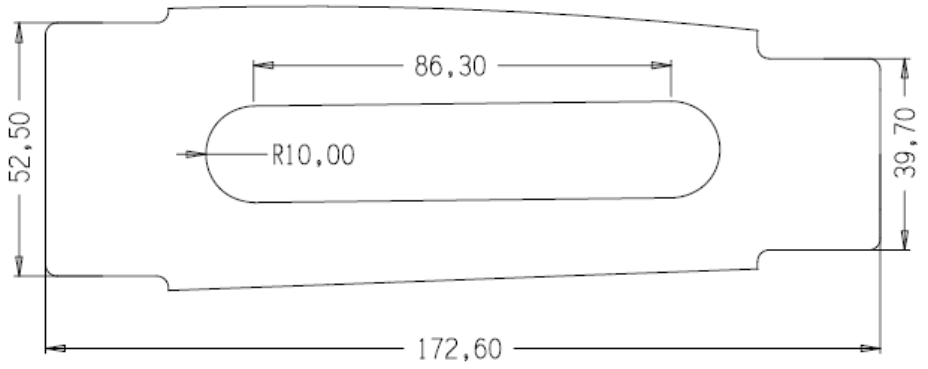

Figure 48: 2D View of the Rib Portion Located between the Main and Secondary Spars (Mid-Chord) [mm]

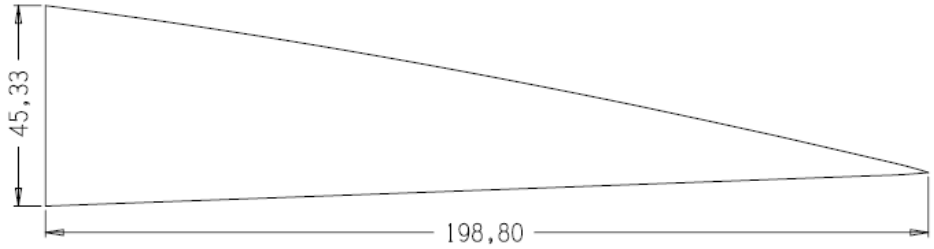

Figure 49: 2D View of the Rib Portion Located at the Trailing Edge [mm]

6.2.3 Composite Skin

The material selected for the composite skin manufacture was the fiber-reinforced composite formed of 7781 E-Glass Fabric – LY5052 Araldite Resin – HY5052 Aradur Hardener. The method of production was the wet lay-up method. The selected fabric 7781 has a woven form of 0°/90° fiber orientation. Four layers of this fabric was used to form the composite skin, hence the staking sequence of the skin was 0°/90°/0°/90°/0°/90°/0°/90°. Since the wet lay-up method also required a mold, then a mold for this process was first manufactured, and then the skin was cured at the room conditions. Figure 50 gives a picture of the mold and the cured composite skin lay-up.

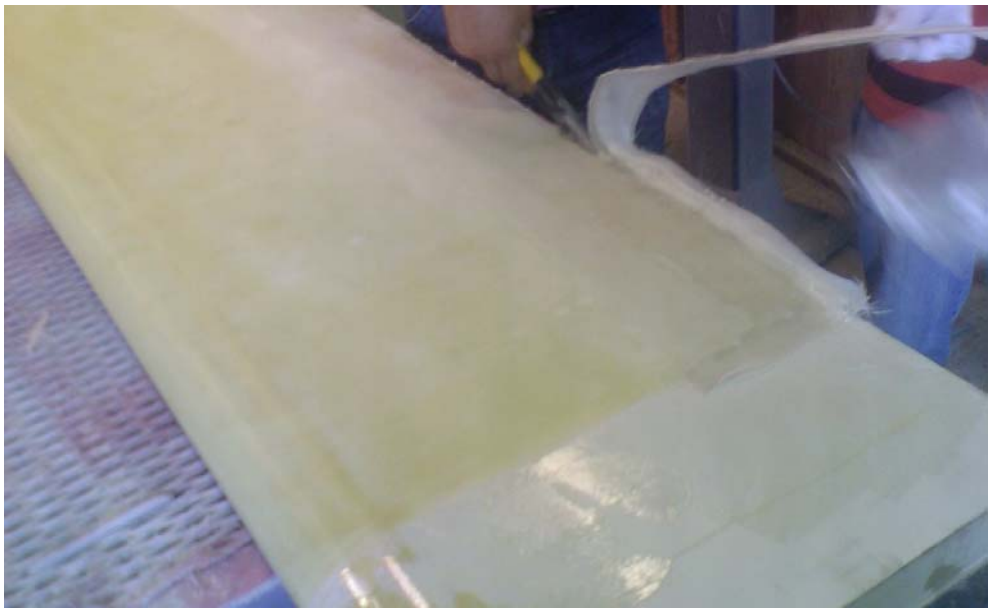

Figure 50: Picture of the Mold Manufactured for the Production of the Composite Skin with Wet Lay-up Method and the Cured Composite Skin

6.2.4 Corner Connectors

The corner connectors were used to stiffen the connection between the spars and the ribs. They were produced from an extrusion profile of Aluminum 7075-T651. Figure 51 shows the cross-sectional view of the profile selected.

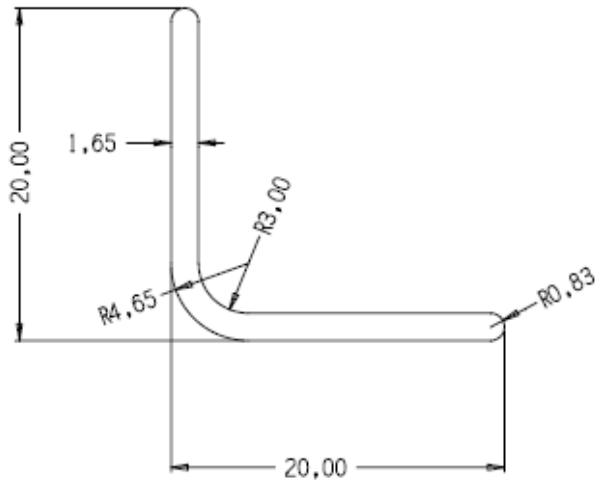

Figure 51: Cross-Section View of the Corner Connector Extrusion Profile [mm.]

6.2.5 Fasteners

There were two types of fasteners used which were the rivets and bolts. The rivets were used for the spar-rib and skin-rib connections. The types of the rivets used were ST3210 steel rivets and HKS3206 level head aluminum rivets. The bolts were used at the control surface portions in order to fasten the control surface skin, secondary spar and composite skin of the wing torque box. The bolts used were standard M4-15 type steel bolts.

6.2.6 The Process and Assembly

First the spars were cut from the corresponding extrusion profile of material Aluminum 7075-T651. Following the spars the ribs were cut from 0.8 [mm] Aluminum 2024-T3 sheet metal. Afterwards, the corner connectors were cut with the length of 30 and 40 [mm] from the extrusion profile of material Aluminum 7075-T651. Altogether 32 pieces of 30 [mm] connectors and 40 pieces of 40 [mm] connectors were cut. Finally the composite skin was manufactured by using the wet lay-up method from 4 layers of woven 7781 E-Glass Fabric – LY5052 Araldite Resin – HY5052 Aradur Hardener combination. The fiber orientation of the composite skin regarding the woven fabric was 0°/90°/0°/90°/0°/90°/0°/90°. Therefore, the necessary main parts of the wing torque box were manufactured and then assembled.

Figure 52 to Figure 54 give some intermediate assembly stages. Figure 52 shows an assembly of leading edge rib portions with corner connectors. Figure 53 gives the assembled leading edge rib and main spar, and Figure 54 illustrates the assembled mid-chord and trailing edge ribs on the spars. The assembled internal structure is presented in Figure 55.

Figure 52: Assembly of Leading Edge Rib Portions and Corner Connectors by ST3210 Steel Rivets

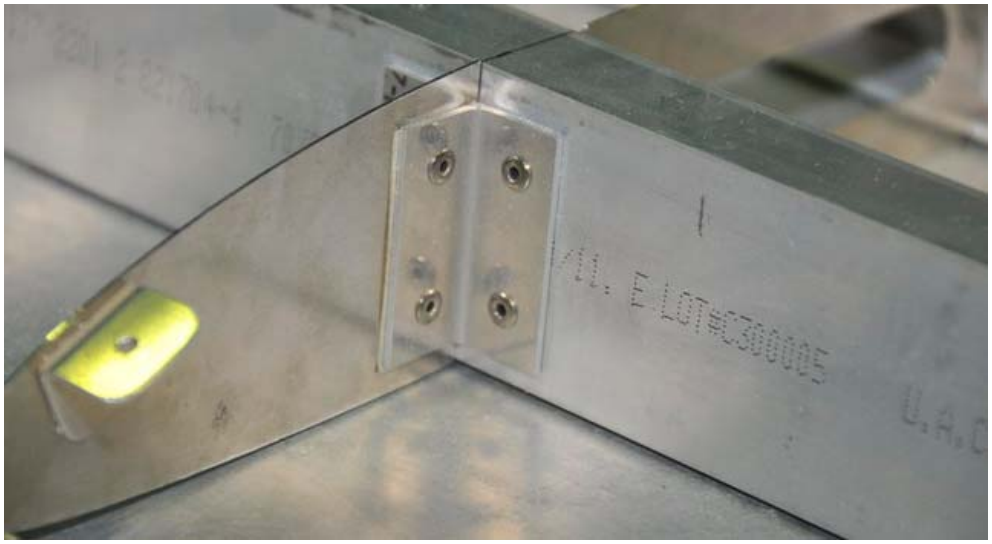

Figure 53: Leading Edge Rib Main Spar Assembly

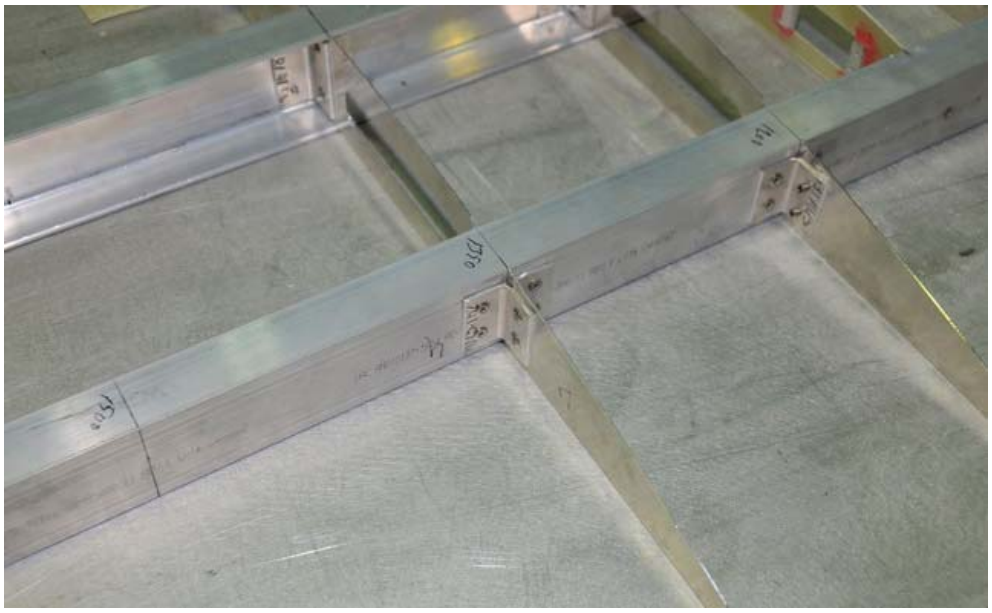

Figure 54: Mid-chord Ribs and Trailing Edge Ribs Assembled with the Main and Secondary Spars

Figure 55: Assembled Wing Torque Box Internal Structure

There were some cut-outs on the composite skin for the access of servos which were to be used in the smart control surfaces. There were two servo motors controlling each of the smart flap and smart aileron in each of the wing. Therefore,

four access seals were opened on the top surface of the composite skin. To support and close the seal a latch manufactured from the skin material. Figure 56 shows one of the access seals and its support structure.

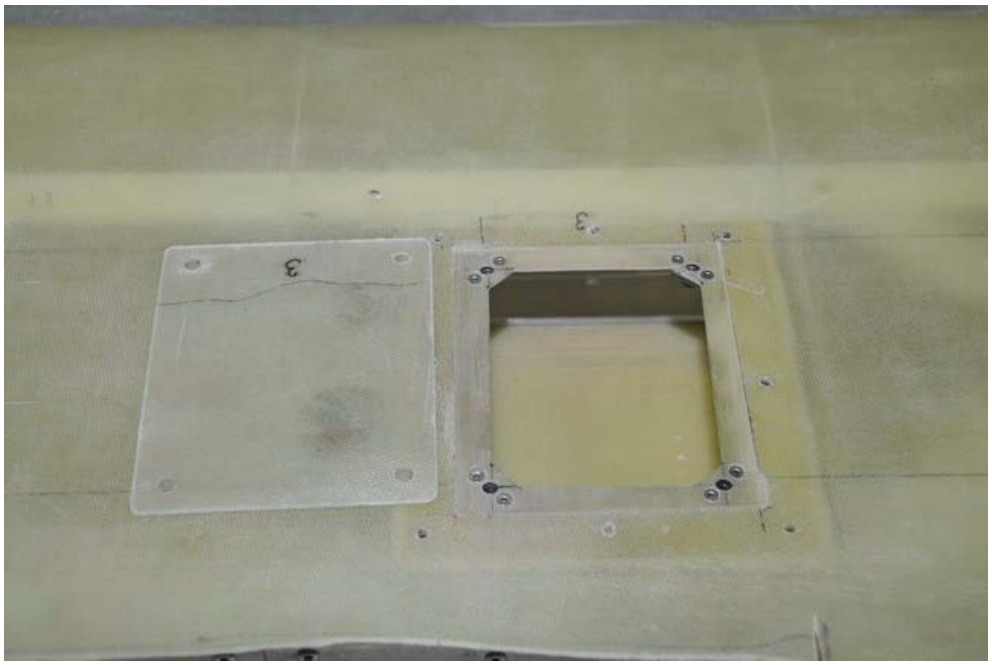

Figure 56: Servo Motor Access Seal and the Support Structure on the Composite Skin

At this stage of the study, the design of the mission adaptive control surfaces were also finalized [2]. The servo motors controlling these surfaces were found to be very powerful ones. The servo motors originally thought to be fitted on the skin, however, the 30 [kg.f/cm] torque amount they generate was over the maximum concentrated loading that the skin could sustain. Hence a rib like structure for each servo motor was designed and manufactured. This way the spars shared the load. The material used was the same composite material used for the skin. Nevertheless, the number of layers was increased to 6 layers which had a fiber staking sequence of 0°/90°/0°/90°/0°/90°/0°/90°/0°/90°/0°/90°/0°/90°. Figure 57 shows the cross-sectional view of the CAD model of the servo support structure and Figure 58 shows the assembled view.

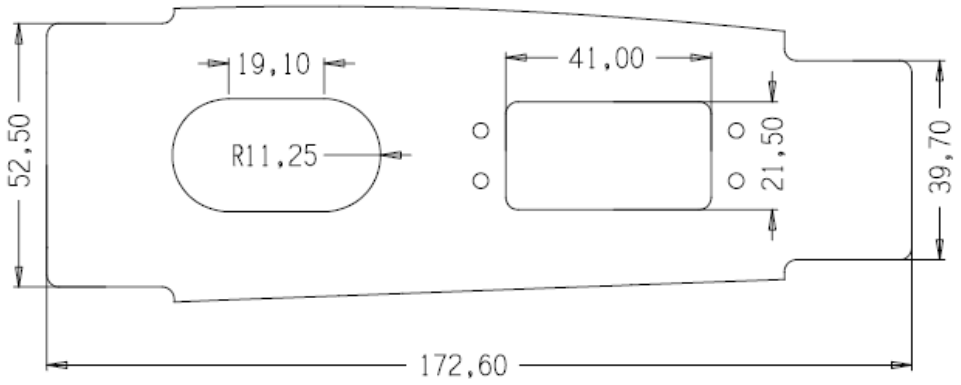

Figure 57: Cross-sectional View of the CAD Model of the Servo Support Structure

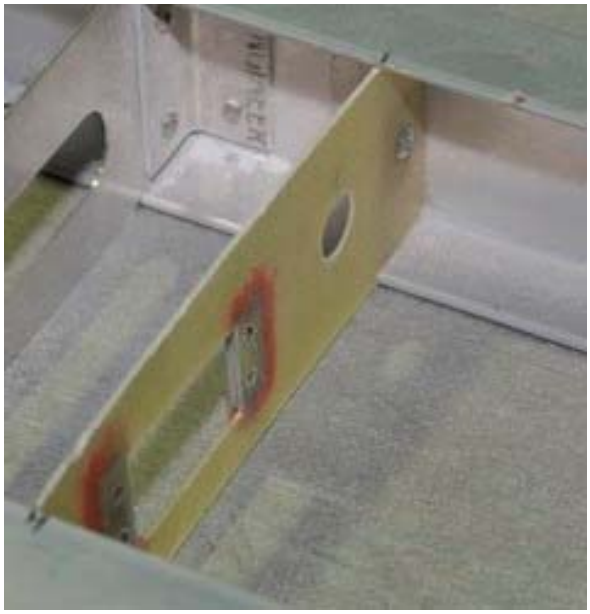

Figure 58: Assembled View of the Servo Support Structure

The final step was the assembly of the skin over the internal structure and polishing with undercoat dye. The skin was fastened to the ribs by using HKS 3206 Aluminum level head rivets and polymer adhesive. Figure 59 shows the assembled wing torque box and Figure 60 also shows the tip section of the wing torque box.

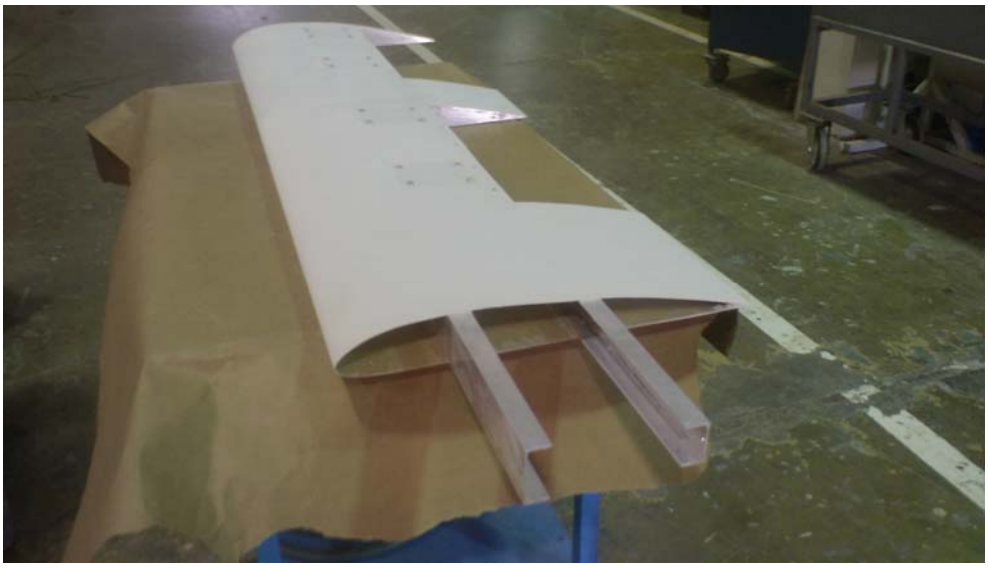

Figure 59: The Assembled Wing Torque Box Structure

Figure 60: The Tip Section of the Assembled Wing Torque Box Structure

6.3 Modifications

6.3.1 The Modifications in Material Properties

After the manufacturing of the skin was completed it was observed that there were differences in the properties of the laminated composite produced than theoretically assumed values. The theoretical values quoted a layer thickness of 0.27 [mm], but the material used were about 0.375 [mm]. In addition to that the mass of the composite skin was calculated as 2167 [grams] in Model 1 whereas the manufactured composite skin was measured to be 2060 [grams]. Following these observations, it was thought that an excess amount of resin and hardener might be present and it would affect the mechanical and physical properties of the material. An ignition testing was conducted at the Department of Chemical Engineering of Middle East Technical University to reassign the composite material properties.

The ignition test was based on the difference between the burning temperatures of the matrix and the fiber content of a fiber reinforced composite. This temperature difference makes the burning of the matrix content possible without harming the fiber content.

The standard ignition test [20] applied on a specimen with maximum edge length of 1 inch. The best suited length for the platinum crucibles used during the test were 1 centimeters. To increase the accuracy of the experiment 3 specimens were used at a time with 3 different platinum crucibles.

The first step of the experiment for the standard procedure was to heat the platinum vessels at 560°C for 10 minutes in order to clean the crucibles. Following this procedure the crucibles were cooled down to room temperature and then their empty masses were measured. Afterwards, the specimens put into the crucibles and their masses were measured again. Further step was the ignition of the specimens in oven at the temperature of 565±5°C for 90 minutes. When the necessary ignition time ends the crucibles containing the specimens were cooled down to room temperature and the masses measured one last time. Figure 61 shows the specimens before the ignition test and Figure 62 gives the specimens after the test. It can be

understood from the separated and delaminated appearance of the fibers that nearly the entire matrix was burned.

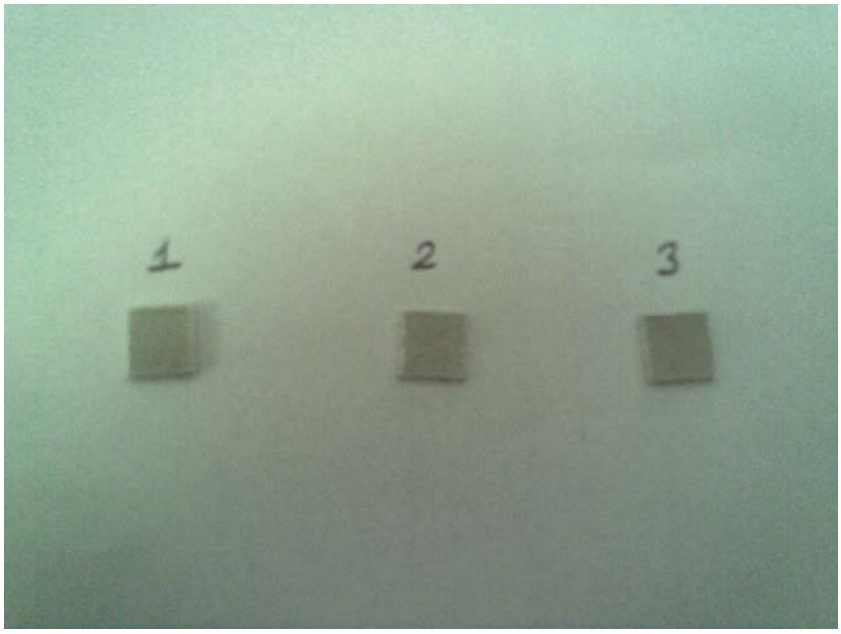

Figure 61: The Specimens before the Ignition Test

Figure 62: The Specimens after the Ignition Test

Table 16 shows the numerical values related to the mass measurements done during the ignition test procedure and Table 17 gives the calculated masses of the material content. The values in the tables were recorded with 4 significant digits by using high sensitivity scales, since the mass of the specimens are very small.

Table 16: The Mass Measurements during the Ignition Test [gram]

Specimen	Masses of the Corresponding Crucible	Mass of the Vessel and Specimen before the Ignition Test	Mass of the Vessel and Specimen after the Ignition Test
1	20.9049	21.0729	21.0023
2	21.1390	21.2998	21.2308
3	18.9629	19.1352	19.0633

Table 17: The Calculated Mass of the Specimen and Its' Contents [gram]

Specimen	Total Specimen Mass	Fiber Mass	Matrix Mass
1	0.1680	0.0974	0.0706
2	0.1608	0.0918	0.0690
3	0.1723	0.1004	0.0719
Average	0.1670	0.0965	0.0705

Using the results of the ignition test, the theoretical values of the mechanical and physical properties of the 7781 E-Glass – LY5052 Araldite Resin – HY5052 Aradur Hardener laminated composite, previously given in Table 5, could be tuned. The applicable method for this tuning was the rule of mixtures method for the calculation of the material properties of the laminated composites [21]. Although this method was originally developed for unidirectional fiber reinforced composites, it was proved that the method was also applicable for the woven composites with an acceptable accuracy [22]. In order to apply this method the density value of the

matrix must be known. The density of the matrix cured at the standard room conditions was found as 1157 [kg/m^3] [23]. The other relevant mechanical and physical properties of the laminated composite data, related to the application of the rule of mixtures method are given in Table 18.

One of the related observations of the experiment was the average volume of the specimens used. Using calipers the volumes of the specimens were measured and the average volume was found as 110.4 [mm^3]. The average matrix volume was also calculated by using the Eqn. 6.1 as;

$$Ave.\,Matrix\,Volume = \frac{Ave.\,Matrix\,Weigth}{Matrix\,Density} = \frac{0.0000705\left[kg\right]}{1157\left[kg/m^3\right]} = 60.9\left[mm^3\right] \quad \text{(Eqn. 6.1)}$$

This shows that the average fiber and matrix volume percentages were 44.8 % and 55.2 % respectively. These values proved that the matrix ratio in the laminated composite manufactured was more than the theoretically assumed values. Then the rule of mixtures method was applied by using the Eqn. 6.2 and Eqn. 6.3 to obtain the tuned properties of the laminated composite [21]. The tuned results are given in Table 19. From this section onwards, these tuned values will be used instead of the values previously given in Table 5.

$$E_{ii} = E_f \times V_f + E_R \times V_R \quad \text{(Eqn. 6.2)}$$

$$G_{ij} = \frac{G_R G_F}{V_R G_F + V_F G_R} \quad \text{(Eqn. 6.3)}$$

Table 18: Theoretical 2D Orthotropic Mechanical and Physical Properties of the 7781 E-Glass Fabric – Araldite LY5052 Resin / Aradur HY5052 Hardener Laminated Composite Material [10] [23]

Density	1772 [kg/m^3]
V_f	49 %
E_{11}	22.1 [GPa]
E_{22}	22.4 [GPa]
G_{12}	3.79 [GPa]
G_{13}	2.96 [GPa]
G_{23}	2.96 [GPa]
E_f	38.6 [GPa]
G_f	7 [GPa]
Ultimate Compression Strength	249 [MPa]
Ultimate Tensile Strength	369 [MPa]
Inter-laminar Shear Strength	33.21 [MPa]

Table 19: Tuned 2D Orthotropic Mechanical and Physical Properties of the 7781 E-Glass Fabric – Araldite LY5052 Resin – Aradur HY5052 Hardener Laminated Composite Material

Density	1513 [kg/m^3]
V_f	44.8 %
E11	21 [GPa]
E22	21.3 [GPa]
G12	3.6 [GPa]
G13	2.81 [GPa]
G23	2.81 [GPa]
E_f	38.6 [GPa]
G_f	7 [GPa]
Ultimate Compression Strength	237 [MPa]
Ultimate Tensile Strength	350 [MPa]
Inter-laminar Shear Strength	31.55 [MPa]

6.3.2 Modifications on the Total Mass

There were some non-load carrying masses added on the structure during the manufacture. These masses were basically the wing tip and the overcoat polish. Table 20 summarizes the necessary masses to be added on the Model 1. Those masses will be added as non-structural-mass on the structural model.

Table 20: Non-structural Masses to be Added on the Model 1

Mass to be Added	Corresponding Mass [gram]
Wing Tip Fairing	170
Polish and Adhesive	500
Rivets	1000
Bolts and Nut Plates	100

6.4 Discussion

This chapter detailed the manufacturing process of the mission adaptive wing. From this point onwards, the first manufactured wing torque box will be called as Wing 1.

CHAPTER 7

GROUND VIBRATION TESTS OF THE MISSION ADAPTIVE WING

7.1 Introduction

This chapter gives the details of the ground vibration tests (GVT) conducted on the wing manufactured by TAI (*i.e.* Wing 1). The purpose of these test were also to verify the theoretical model developed for the wing. Hence the Model 1 may be subjected to some modifications. This chapter also indicates and details these possible structural modifications.

7.2 Experimental Setup

The equipments used in the experiments are given in Table 21.

Table 21: The List of Equipments Used in the Ground Vibration Tests

Equipment	Type
Signal Generator	Agilent 33120A
FFT Analyzer	B&K Pulse 3560-C
Power Amplifier	B&K 2720
Impact Hammer	B&K Type 8206
Modal Exciter	B&K Type 4825
Force Transducer	B&K Type 8230-002
One-Axis Accelerometers	B&K Type 4508-B

Figure 63 shows a picture of the control and analyses equipments used in the experiments, and Figure 64 gives a picture of the fixture designed, wing torque box, modal exciter and the accelerometers mounted on the structure.

Figure 63: The Control and Analyses Equipments Used in Ground Vibration Tests (From Left to Right, FFT Analyzer, Computer, Signal Generator at top and Power Amplifier at bottom)

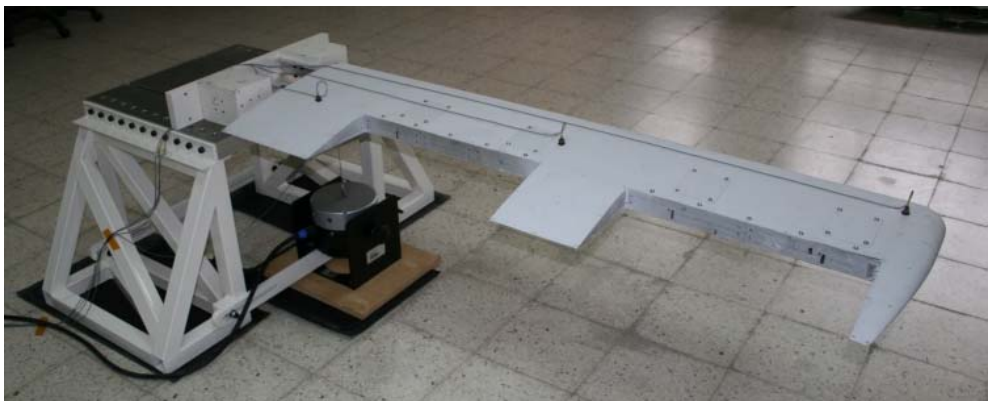

Figure 64: The Picture of the Fixture, Wing Torque Box, Modal Exciter and Three Single-Axis Accelerometers

7.3 The Experiments and the Results

The following procedure was employed during the experiments. First the wing was excited by the impact hammer to locate the ranges of the resonances. The wing was then excited by using a modal shaker and white noise type excitation. This gave the accurate locations of the resonant frequencies. The wing was finally excited by using the modal shaker but this time with a sine sweep signal. That helped to verify the accurate resonant frequencies. The mode-shape at the resonance frequencies were determined by using roving-hammer test [24] [25].

7.3.1 The Impact Hammer Excitation

The impact hammer of 8206 series was used to excite and measure impact forces on small to medium structures [26]. There were three kinds of tips available for the device; rubber, plastic and aluminum. The plastic tip was selected. This was due to the fact that around 100 [Hz.] which was the second out-of-plane bending resonance frequency the rubber tip starts to loose effectiveness and the aluminum tip was suitable for higher levels of forcing and higher frequencies. These can be better understood from Figure 65.

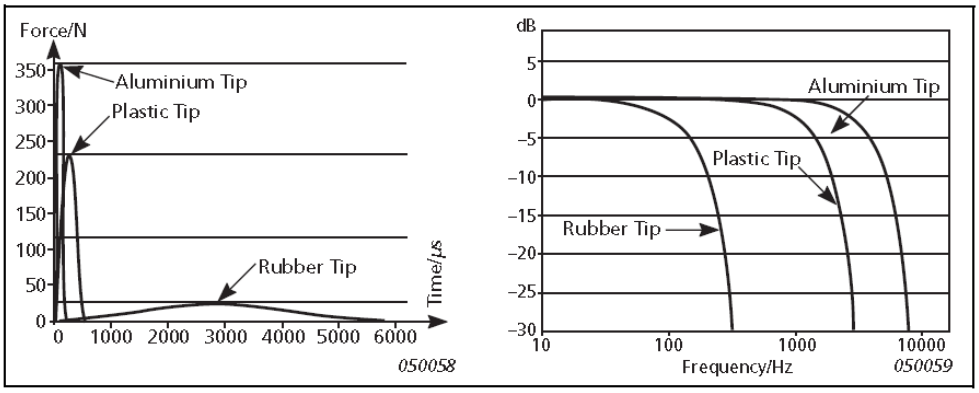

Figure 65: Impulse Shapes and the Peak Values (Left) and Force Spectrum (Right) Related to Tips of Impact Hammer B&K Type 8206-002 [26]

The system used for analyses, PULSE™ Type 3560-C, can be operated using a software called Modal Test Consultant™ which has an ability of geometry-driven data acquisition. During the experiments this tool was used. The geometry defined for the data acquisition is given in Figure 66. In addition to that, Table 22 defines the utilization of the data points on the geometry given in Figure 66.

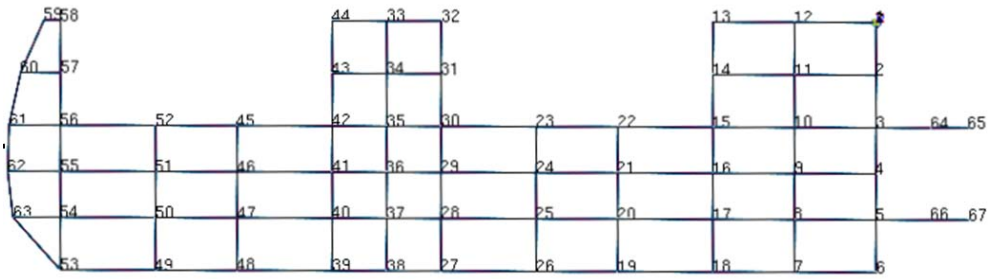

Figure 66: The Geometry Defined for Data Acquisition Using Modal Test Consultant™ for Impact Hammer Tests

Table 22: The Summary of the Utilization of the Data Points in the Software Model Test Consultant™

Data Point	Use Defined in Modal Test Consultant™
1-63	Roving Hammer
64-67	Boundary Conditions
5	Force Transducer
54	Accelerometer 1
29	Accelerometer 2
10	Accelerometer 3

Approximately 10 data sample were collected for each of the 63 excitation locations. The average of these data was used in FFT analyses for each of the data location. The FRF data representing the magnitude of accelerance (Acceleration/Force) measured by three single-axis accelerometers corresponding to

63 data locations are shown in figure. The magnitude of accelerance values obtained by averaging all the data obtained is given in Figure 68.

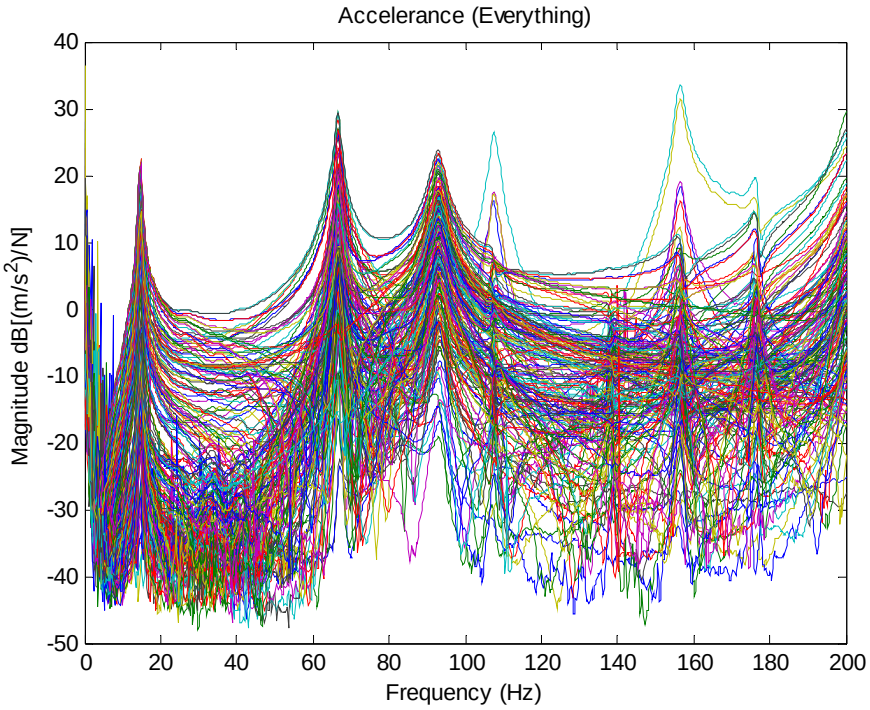

Figure 67: The Magnitude of the Accelerance Data in Frequency Domain Obtained from Three Single-Axis Accelerometers and Force Transducer for 63 Measurement Points

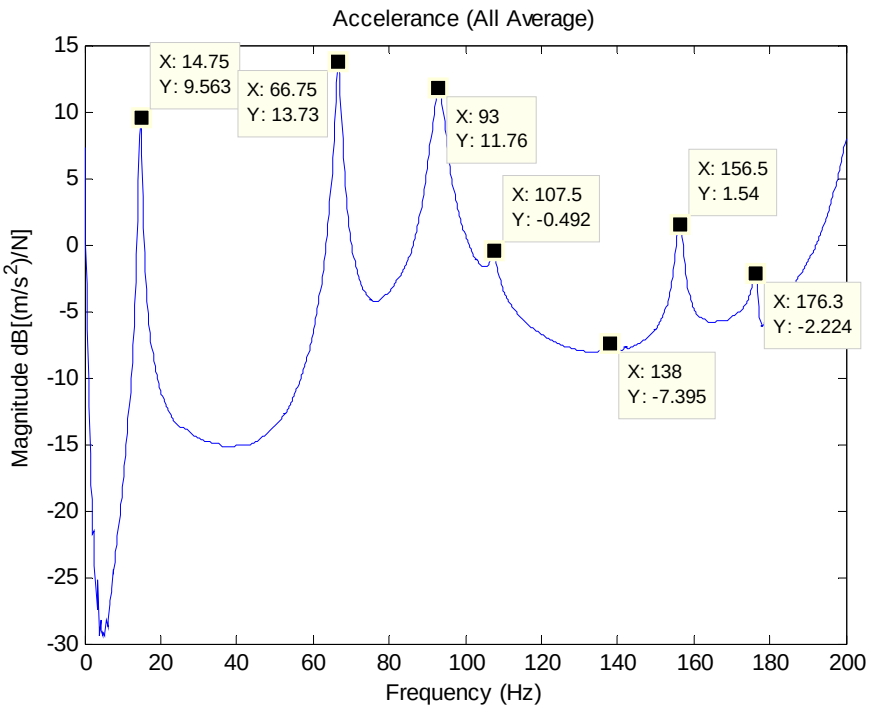

Figure 68: The Averaged Magnitude of the Accelerance Data in Frequency Domain Obtained from Three Single-Axis Accelerometers and Force Transducer for 63 Measurement Points

The peak values of Figure 68 give some of the resonance frequencies of the structure. Since the accelerometers used are single-axis accelerometers it was known that they can only be sensitive to out-of-plane bending and torsional motions. The mode shapes had been calculated by averaging the experimentally obtained data. The experimental mode shapes corresponding to first three resonance frequencies of Figure 68 are given in Figure 69, Figure 70 and Figure 71 in order. The processed data was normalized with respect to the maximum value.

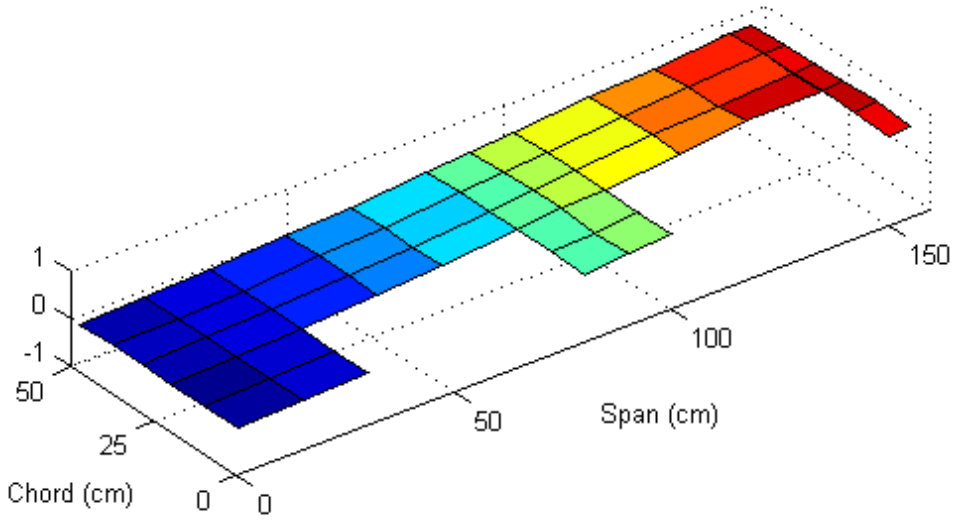

Figure 69: The Experimental Mode Shape of the Wing Torque Box at 14.75 Hz (Corresponding to First Out-of-plane Bending Resonance Frequency)

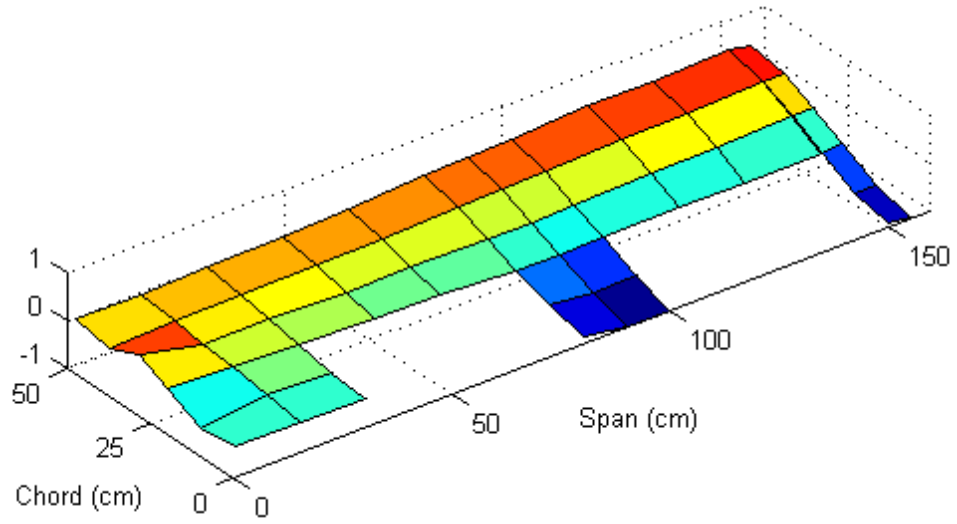

Figure 70: The Experimental Mode Shape of the Wing Torque Box at 66.75 Hz (Corresponding to First Torsional Resonance Frequency)

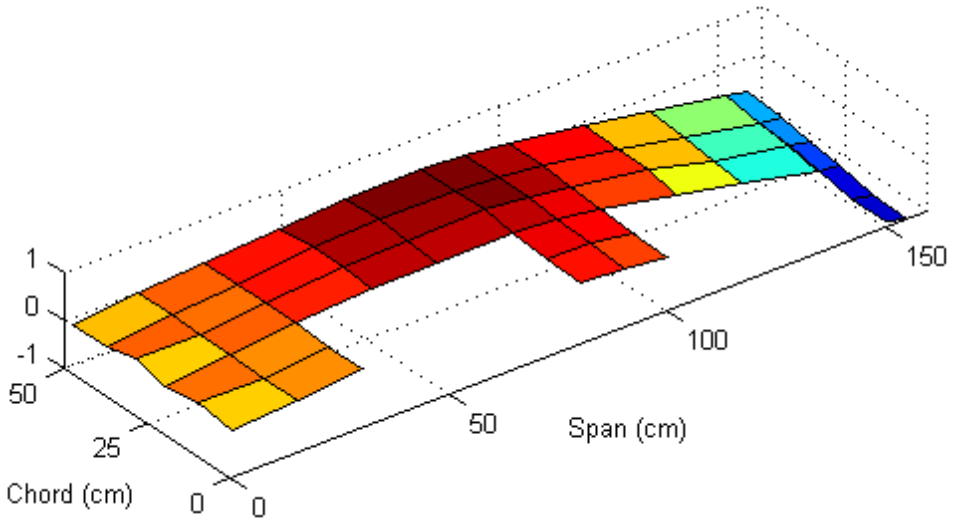

Figure 71: The Experimental Mode Shape of the Wing Torque Box at 93.00 Hz (Corresponding to Second Out-of-plane Bending Resonance Frequency)

The in-plane bending resonance frequency value was also obtained by rotating the measurement axis of the accelerometers by 90°. The excitation applied was this time lateral. The obtained resonance frequency value was roughly found to be around 43.5 [Hz.], however the corresponding mode shape could not be obtained because of the difficulties in both lateral excitation and response measurement.

7.3.2 The White Noise Excitation

The white noise is a random signal which contains equal power within a fixed bandwidth at any center frequency. By using the signal generator the modal exciter was given an input with a white noise signal. FFT analyzer was set to a center frequency of 100 [Hz.] for data processing. Figure 72 gives the accelerance values were obtained from data collected from Accelerometer 1 which was located at point 54 and the force transducer which was located at point 5 of Figure 66.

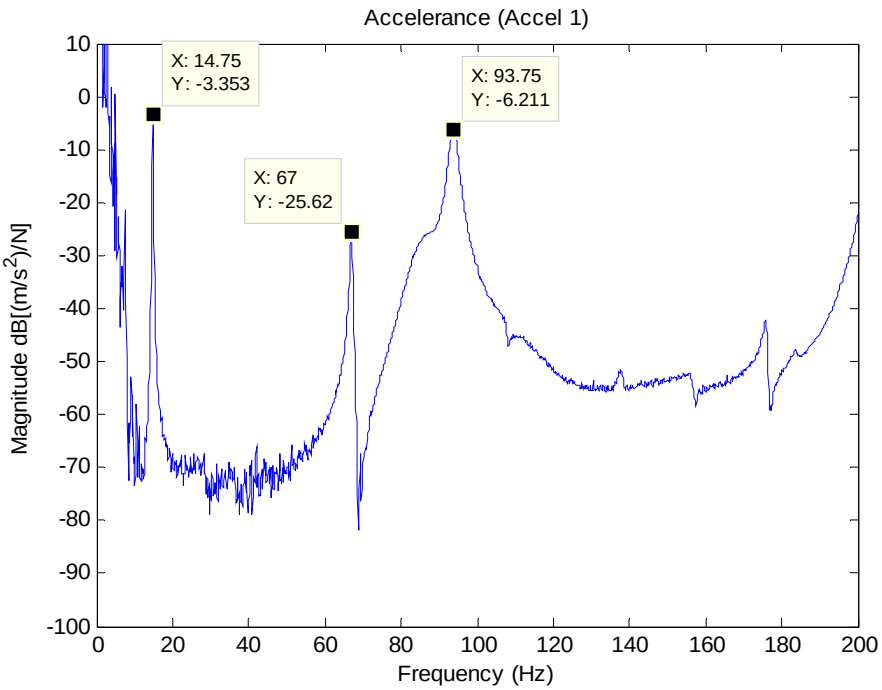

Figure 72: The Magnitude of the Accelerance Data in Frequency Domain Obtained from Accelerometers 1 and Force Transducer for White Noise Excitation

7.3.3 The Sine Sweep Excitation

By using the signal generator, the modal exciter was given an input with a sine sweep signal of 5-200 [Hz] band. Figure 71 gives the accelerance values were calculated by data collected from Accelerometer 1 which was located at point 54 and force transducer which was located at point 5 of Figure 66.

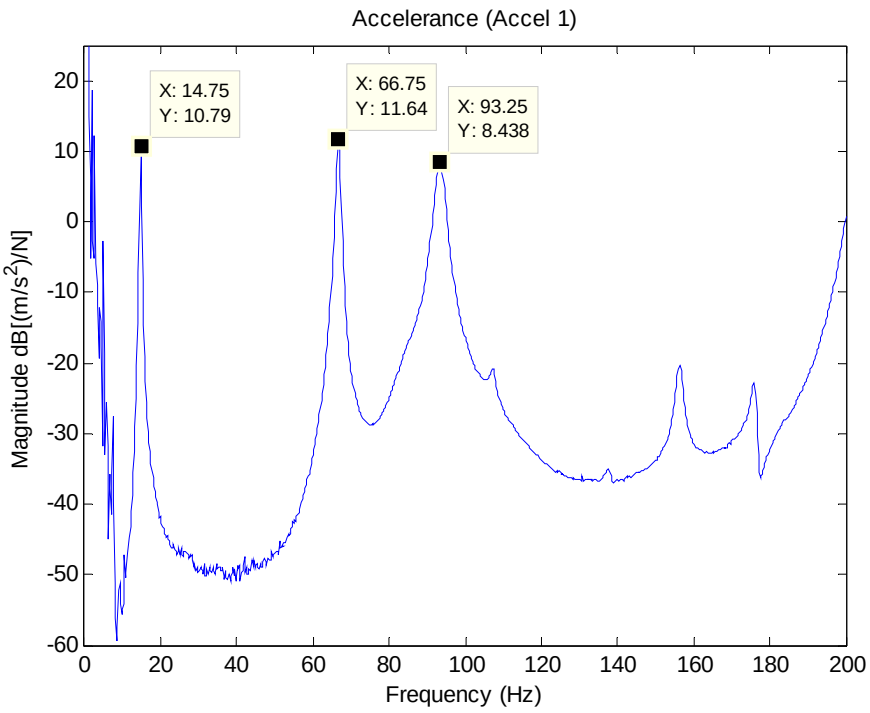

Figure 73: The Magnitude of the Accelerance Data in Frequency Domain Obtained from Accelerometers 1 and Force Transducer for Sine Sweep Excitation

Table 23 gives the comparison of the results of the ground vibration tests, obtained from the roving impact hammer excitation, the white noise excitation and the sine sweep excitation.

Table 23: Summary of Results of the Ground vibration Tests

Mode Shape	Resonance Frequency (Impact Hammer) [Hz]	Resonance Frequency (White Noise) [Hz]	Resonance Frequency (Sine Sweep) [Hz]
1. Out-of-Plane Bending	14.75	14.75	14.75
1. Torsional	66.75	67.00	66.75
2. Out-of-Plane Bending	93.00	93.88	93.25

CHAPTER 8

VERIFICATION AND TUNING OF THE STRUCTURAL MODEL OF THE MISSION ADAPTIVE WING

8.1 Introduction

This chapter gives the comparative studies of the theoretically obtained natural frequency values and the mode shapes with those obtained from the ground vibration tests. The purpose was to verify the developed finite element model of the wing and structurally tune that model wherever necessary.

8.2 The Comparison of the Results of the Experiments and the Finite Element Analyses

Table 24 gives the results of the developed finite element model (Model 1) and experimental results achieved on the manufactured wing (Wing 1) together with the percent difference with respect to the experimental results.

Table 24: The Comparative Frequency [Hz.] Results of the Finite Element Analysis of Model 1 and Experimental Analysis of Wing 1 with the Percent Difference with Respect to the Experimental Results of Wing 1

Mode Shape	Model 1 Natural Frequencies (FEM)	Wing 1 Resonance Frequencies (Experimental)	% Difference with Respect to Experimental Data
1. Out-of-plane Bending	17.29	14.75	~17.20
1. In-plane Bending	56.42	43.50	~29.70
1. Torsion	63.16	66.75	~-5.38
2. Out-of-plane Bending	106.67	93.00	~14.70

The analysis of the results revealed an appreciable level of discrepancy. The following sections will detail the studies conducted for the alleviation of these differences.

8.3 The Structural Tuning of Model 1

There were two structural modifications done on the original design during the manufacturing of Wing 1. These were the addition of rib like structures for servo motor supports and the servo motor access seals opened on the upper surface of the skin. As the first step during the updating process, the rib like structures and the seals were added to the model directly as they appear in the Wing 1.

8.3.1 Modeling the Structures for the Servo Support

The servo support structures were manufactured from the E-glass 7781 Woven Fabric – Araldite LY5052 Resin – Aradur HY5052 Hardener fiber reinforced composite with staking sequence of 0°/90°/0°/90°/0°/90°/0°/90°/0°/90°/0°/90° and the geometry was previously shown in Figure 57. The same corner connectors and rivets used for fastening the ribs at the mid-chord location were also used in the manufacturing of the servo motor support structures already given in Figure 51. The element type used for meshing was 2D shell elements with QUAD4 element topology. Figure 74 shows the geometrical model of the servo support structures generated for finite element modeling, and Figure 75 illustrates the mesh generated on the servo support structures. Figure 76 and Figure 77 on the other hand represent, respectively, the geometric model and the finite element model of the internal structure of the wing torque box where the servo support structures were included in the analysis.

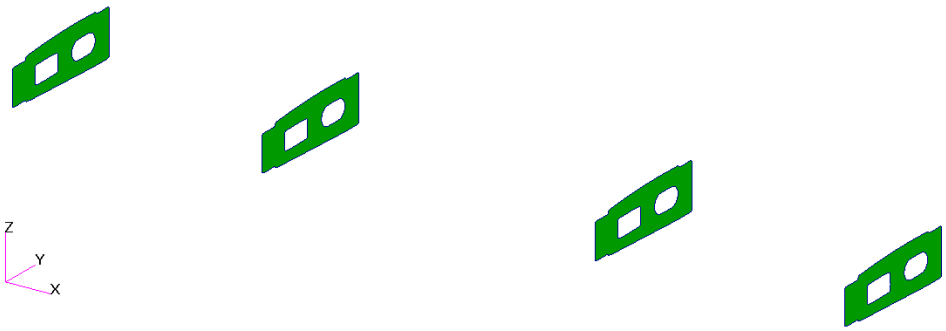

Figure 74: Geometrical Model of the Servo Support Structures Generated for Finite Element Method Applications

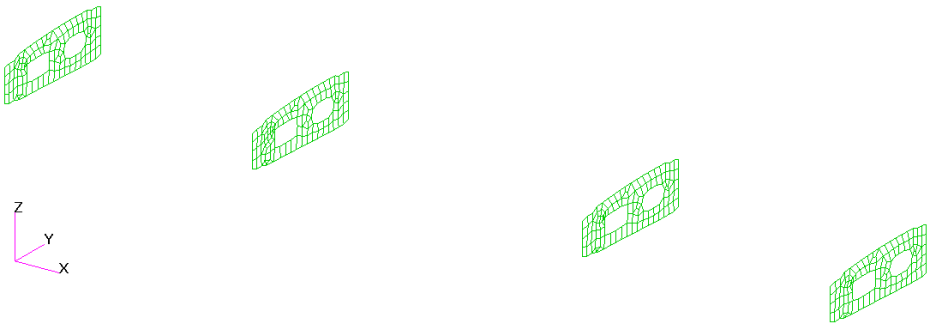

Figure 75: Mesh Generated on the Servo Support Structures by Using 2D Shell Elements for Finite Element Analyses

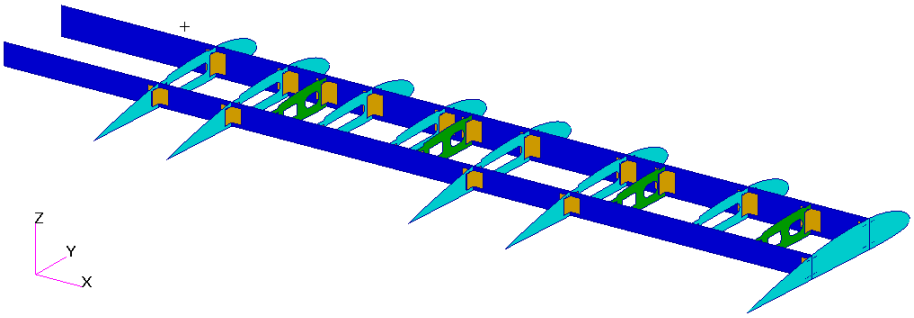

Figure 76: Modified Geometrical Model of the Wing Torque Box Internal Structure

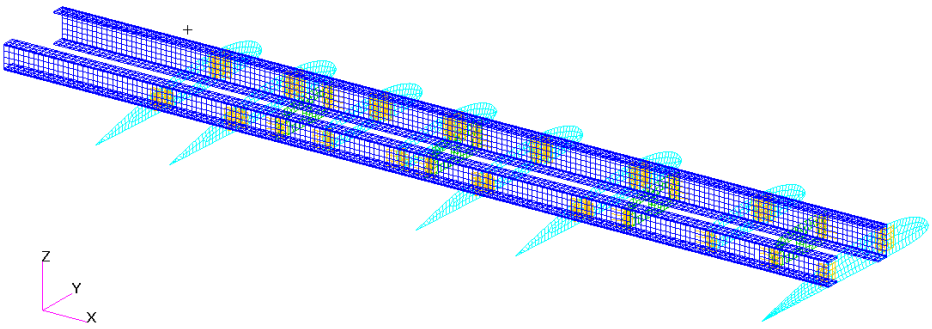

Figure 77: Mesh Generated on the Modified Geometrical Model of the Wing Torque Box Internal Structure

8.3.2 Modeling the Servo Motor Access Seals

The servo motor access seals were opened on the upper surface of the composite skin for servo motor mounting and maintenance purposes. The material used for manufacturing the servo access seals and their support structures were E-glass 7781 Woven Fabric – Araldite LY5052 Resin – Aradur HY5052 Hardener fiber reinforced composite with staking sequence of 0°/90°/0°/90°/0°/90°/0°/90°. The modeling of the seals and the related support structures were done by using 2D Shell elements. Figure 78 is the isometric view of the geometric model of the support structures and Figure 79 is the isometric view of the geometric model of the seals and support structures together. Furthermore, the finite element mesh generated over the geometries is given in Figure 80.

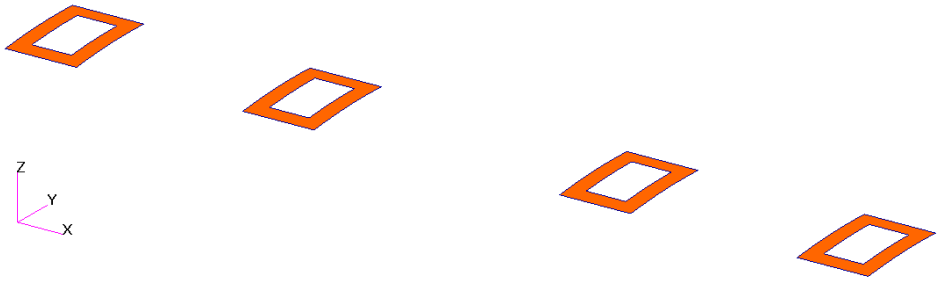

Figure 78: Isometric View of the Geometric Model of the Servo Access Seals' Support Structures

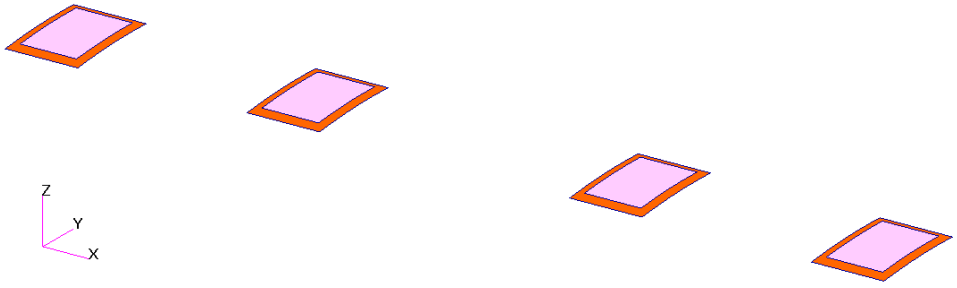

Figure 79: Isometric View of the Geometric Model of the Servo Access Seals and Their Support Structures

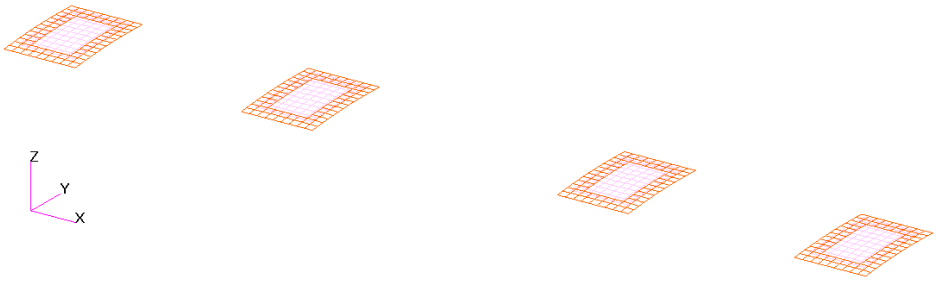

Figure 80: Mesh Generated over the Servo Motor Access Seals and Their Support Structures

The connections of the support structure and the seals to the composite skin were done using RBE2 type multi-point-constraint elements. Since the material used for the skin and the support structures are the same the bonding between them assumed to be perfect, hence the RBE2 element were created between every close node of both structures. The support structures were connected to the seals with the help of four bolts used at each corner of the rectangular seals. Therefore, at the finite element model the stiffness of these connections were also simulated with RBE2 type elements at the bolt locations. Figure 81 shows a zoomed view of the RBE2 type connection used in the servo access seals and their support structures.

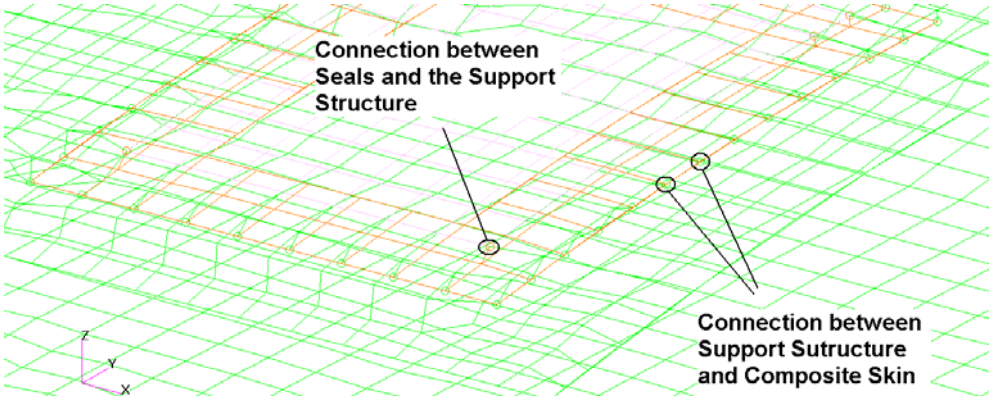

Figure 81: Zoomed View of the RBE2 Type Multi-Point-Constraints Used to Model the Connections of the Servo Access Seals and Their Supports

8.4 The Mass Tuning of Model 1

The manufactured Wing 1 contained some additional mass of 1.984 [kg] comparing with the Model 1. These masses were the structural and non-structural masses. The structural masses coming from the structural changes which were already been added in finite element model, Model 1, by the inclusion of the servo motor support structures and the latches. Those structural mass values were being 51 [gram] for the servo motor access seal support structures, 55 [gram] for the servo motor supports, and 99 [gram] for the corner connectors of the servo motor supports. The total amount of structural mass added to the structure is 205 [gram]. In addition to these the mass of the composite skin of the Model 1 was calculated as 2111 [gram], however, the physical properties of the composite material were modified using the ignition test data. Thus, the mass of the composite skin of the Model 2 was slightly decreased to 2038 [gram] including the servo access seals, since they were integral parts in the Model 1.

The non-structural masses given in Table 20, except the wing tip fairing, were modeled by using the non-structural mass option of the software MSC®/PATRAN. This option distributes a defined non-structural mass amount on a selected property set. For instance, the mass amount of the polish and adhesive on the composite skin could be added by giving an input of 0.5 [kg] non-structural mass in the composite skin property input window. Figure 82 shows the input properties window of MSC®/PATRAN for the inclusion of the non-structural mass.

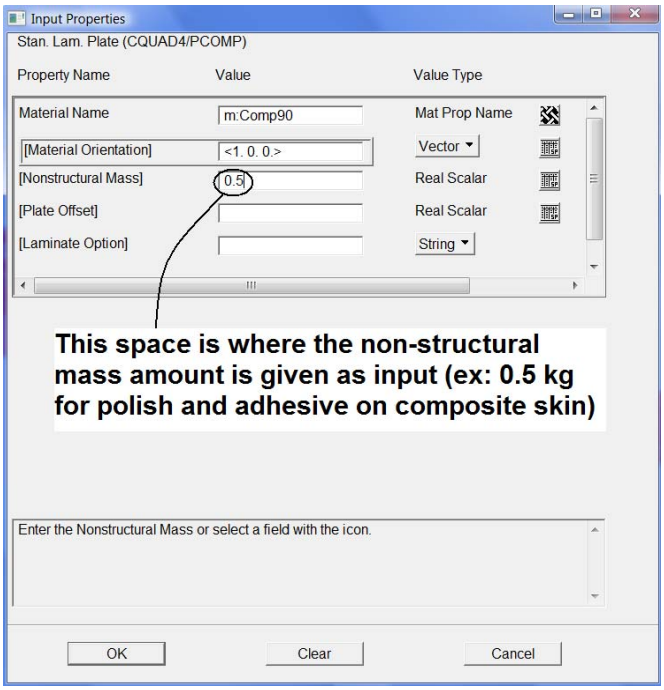

Figure 82: Illustration of Non-structural Mass Input in Software MSC®/PATRAN

The previously defined non-structural masses of Table 20 were added to the related locations. The rivets and some of the bolts were modeled on the corner connectors and rest of the bolts was modeled on the servo motor access seals and their supports.

Finally, the wing tip fairing was modeled with the help of 2D shell elements by using the same material properties with the composite skin. The four layer composite element property assigned for this part resulted in 54 [gram] of mass. Hence the remaining 116 [gram] of the tip fairing mass was again modeled as a non-structural mass. Figure 83 gives the zoomed view of the finite element model of the wing tip fairing.

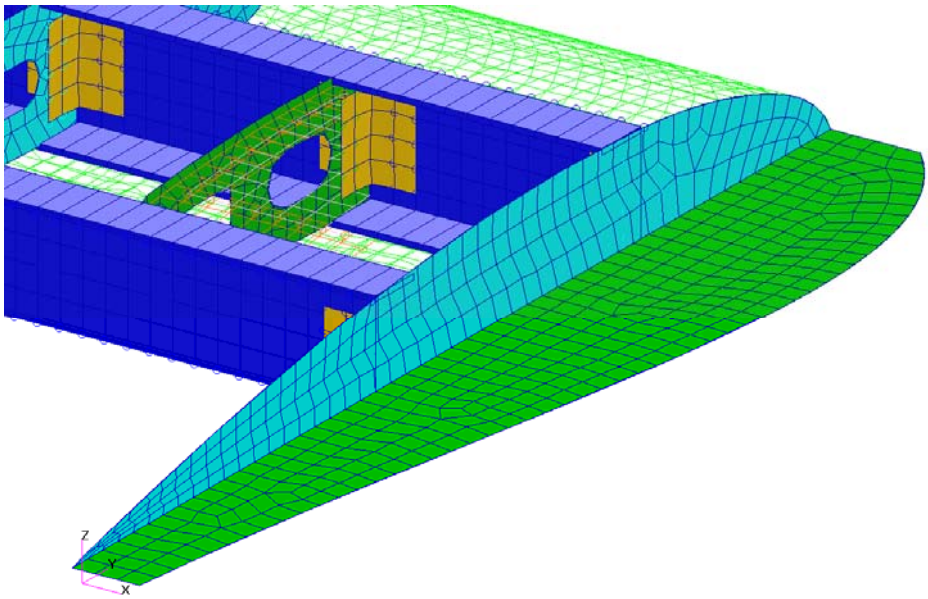

Figure 83: The Finite Element Model of the Wing Tip Fairing

8.5 The Result of Tuning of Model 1

Table 25 gives the comparative results of the tuned model and the produced wing. It can be seen from Table 25 that the results, except the in-plane bending, are in close agreement and even impeccable for the out-out-plane bending modes. The reason behind comparably large relative error between theoretical and the experimental values of in-plane bending was a result of the standard formulation of the 2D shell elements in finite element theory [12]. From this section onwards the tuned model will be referred to as Model 2.

Table 25: The Comparative Frequency [Hz.] Results of the Finite Element Analysis of Model 2 and Experimental Analysis of Wing 1 with the Percentage Difference with Respect to the Experimental Results

Mode Shape	Model 2, Natural Frequencies (FEM)	Wing 1, Resonance Frequencies (Experimental)	% Difference with Respect to Experimental Data
1. Out-of-plane Bending	14.90	14.75	~0.99
1. In-plane Bending	50.16	43.50	~15.32
1. Torsion	63.30	66.75	~-5.17
2. Out-of-plane Bending	93.00	93.0	~0.00

Figure 84 to Figure 87 show the first four mode shapes of the Model 2 corresponding to the natural frequency values given in the second column of the Table 25.

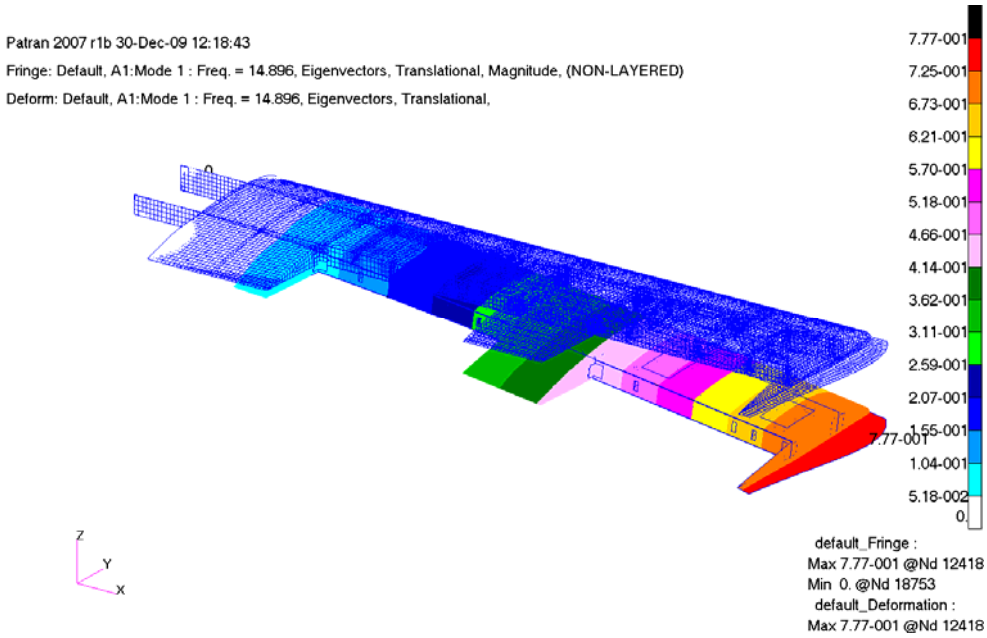

Figure 84: First Out-of-plane Bending Mode Shape of Model 2 [14.896 Hz]

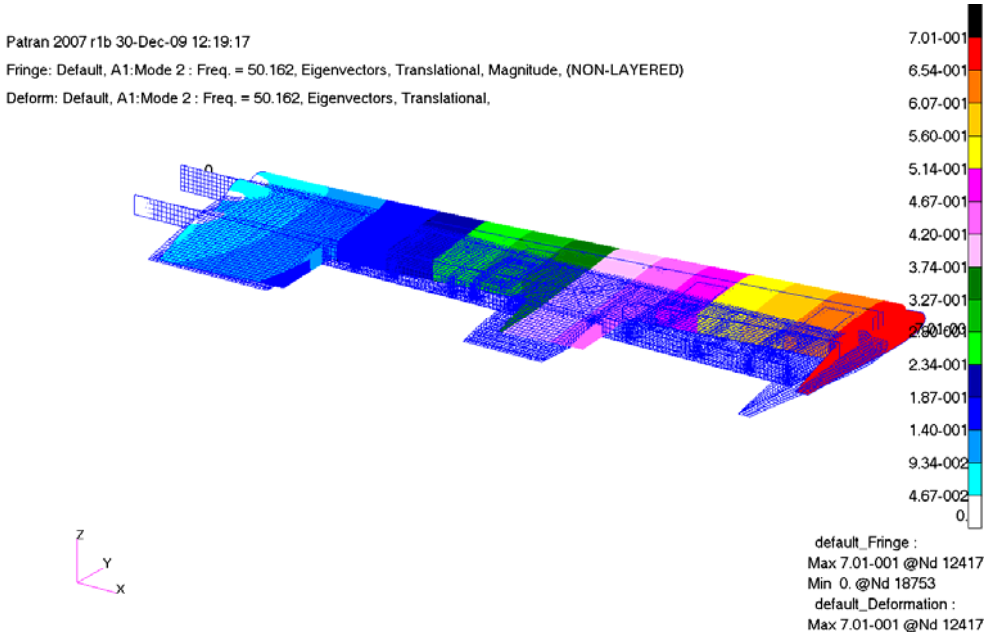

Figure 85: First In-plane Bending Mode Shape of Model 2 [50.162 Hz]

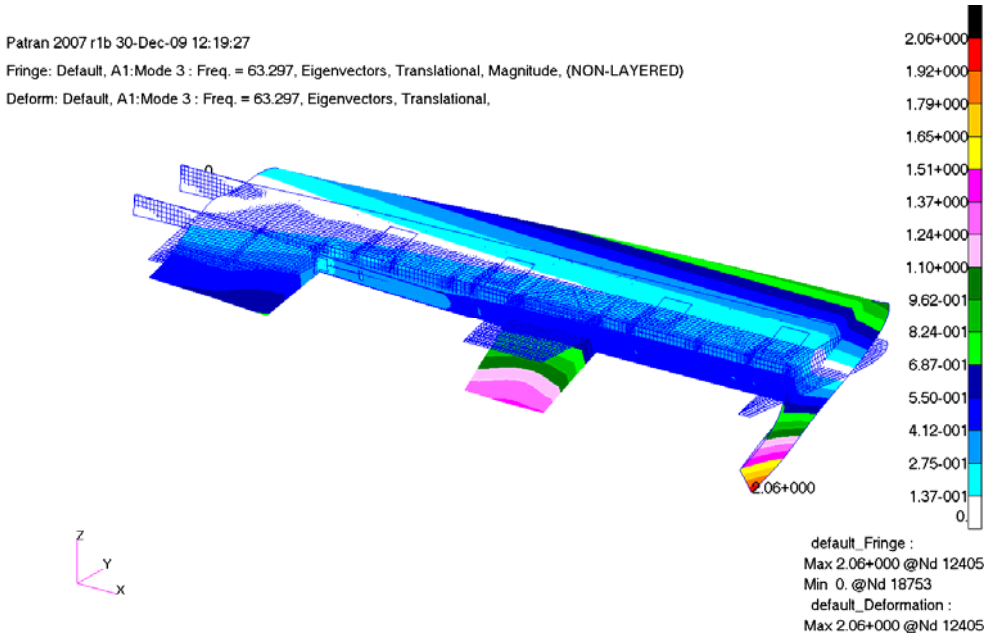

Figure 86: First Torsion Mode Shape of Model 2 [63.297 Hz]

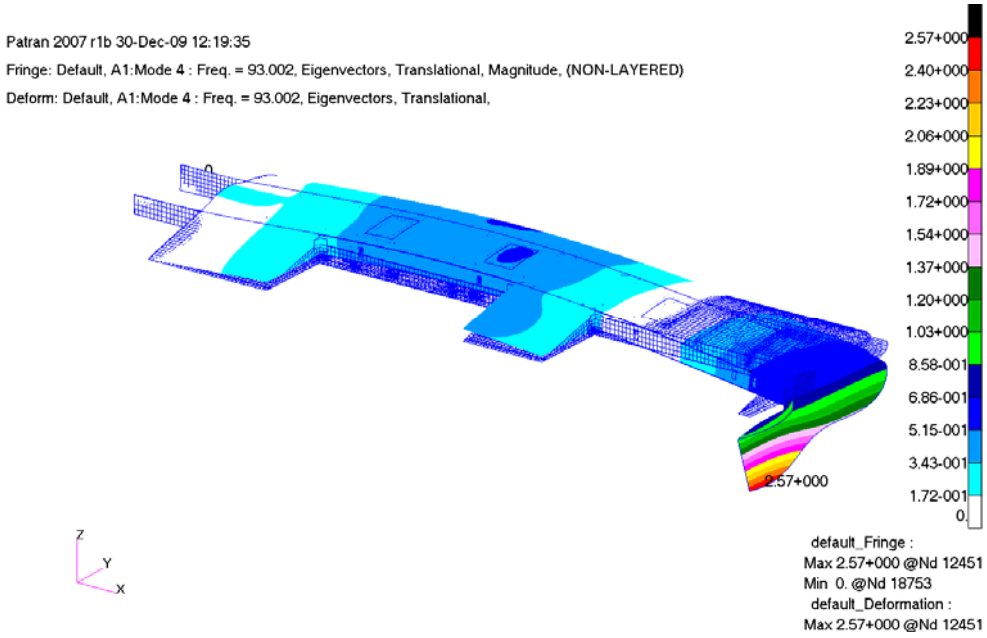

Figure 87: Second Out-of-plane Bending Mode Shape of Model 2 [93.002 Hz]

8.6 Characteristics of the Model 2

The tuned finite element model, Model 2, has a total mass of 7210 [gram], which is exactly the same with the measured mass of the manufactured wing, Wing 1. In addition to the macro scale mass comparison, Table 26 gives some more comparisons about masses of the Model 2 and Wing 1.

Table 26: Mass [gram] Comparison of Model 2 and Wing 1

Part of Interest	Model 2	Wing 1
Main Spar	1986	2000
Secondary Spar	1356	1350
Composite Skin	2066	2060
Rib Portion at the LE	12.5	12
Rib Portion at the Mid-chord	15.7	15
Rib Portion at the TE	11	11
Servo Motor Support Ribs	20.5	20
Tip Rib	45	45
Corner Connector at Main Spar	7	7
Corner Connector at Secondary Spar	5	5
Servo Access Seal Supports	12.8	14
Servo Access Seals	13	13
Wing Tip Fairing	170	170
Polish and Adhesive	500	500
Rivets and Bolts	1100	1100

The total degrees of freedom in the Model 2 by excluding the multi-point-constraints were 85199 corresponding to a number of total nodes of 18904. Table 27 gives the elements used in the Model 2 and their topologies.

Table 27: Element Summary of the Model 2

Element Type	Element Topology	Total Used in the Model
1D Beam	Bar2	668
2D Shell	Quad4	17439
2D Shell	Tria3	33
MPC	RBE2	1650

8.7 The Structural Analyses of the Model 2 and the Results

The static and buckling analyses of Model 2 and the relevant results are given in this section.

8.7.1 The Static Analyses of the Model 2

The static analyses of the Model 2 were done in the same manner with the analyses of the Model 1 described in Section 5.3 and the results are given accordingly.

8.7.1.1 The Static Analysis under Own Weight

The total mass of the Model 2 was 7210 [gram]. Under the effect of the gravitational field the total loading on the wing torque box structure is shown in Table 28.

Table 28: Total Loading on Model 2 under Its Own Weight

Loading Type	Direction	Force [N]	Moment [N.m]
Inertial Load Due to Gravity	X	0	14.0
	Y	0	50.5
	Z	-70.7	0.0

Due to the loading calculated, the displacement field of the wing torque box and the related stress distribution on the internal structure are shown in Figure 88 and Figure 89 respectively. The maximum displacement of 1.85 [mm] occurred at the tip of the wing torque box and the maximum Von-Misses stress value of 15 [MPa] was reached at the boundary of the main spar. Comparing this stress value with the 503 [MPa] yield strength of the aluminum 7075-T561 it was concluded that the resultant stress value was very small and the structure was safe.

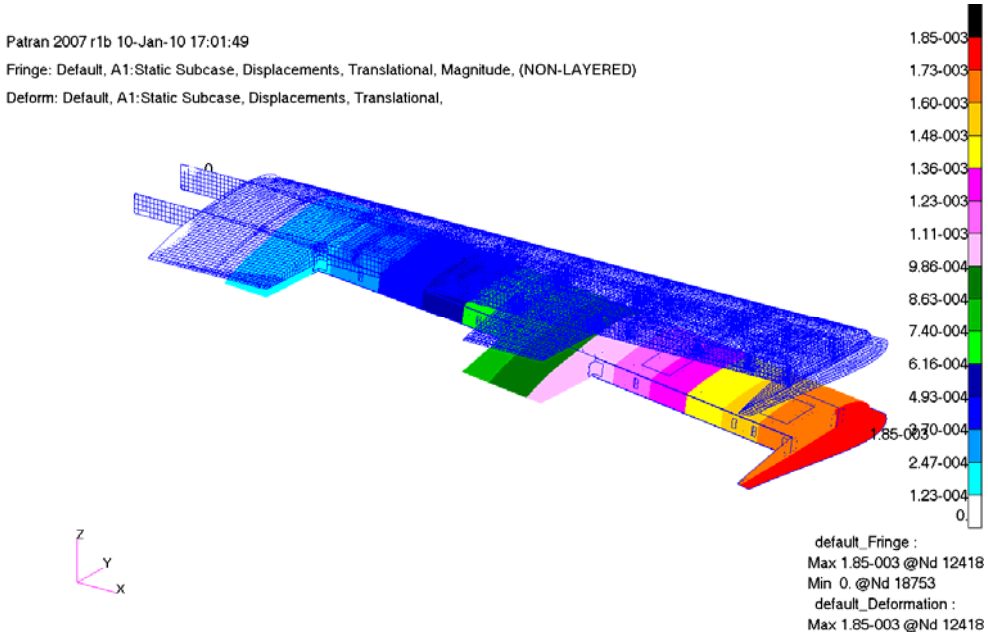

Figure 88: Displacement Field of the Wing Torque Box under Its Own Weight

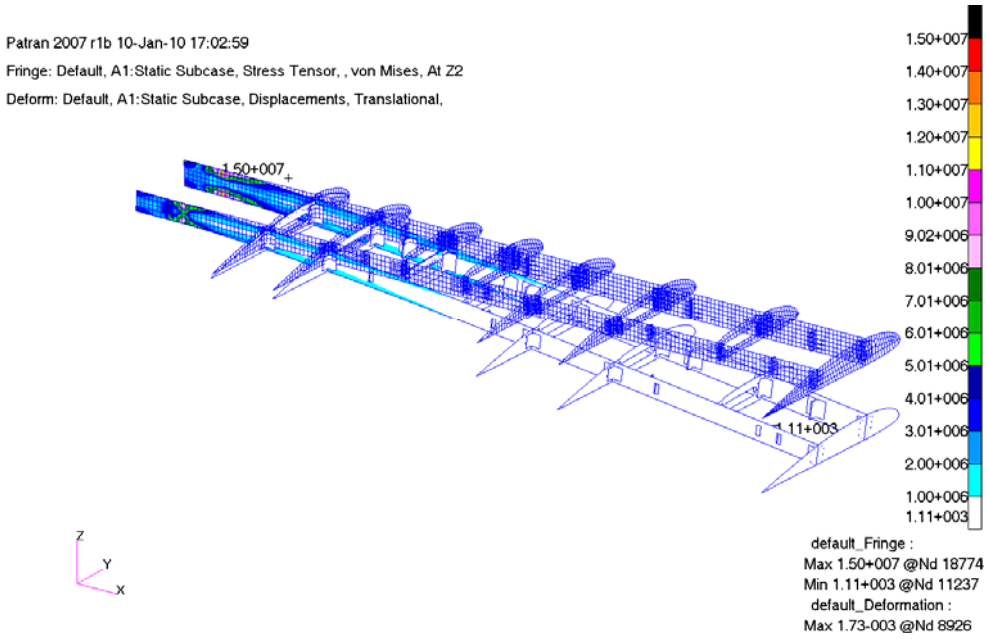

Figure 89: Stress Distribution of the Wing Torque Box Internal Structure under Wings' Own Weight

8.7.1.2 The Static Analysis of the Model 2 in Cruise

The aerodynamic loading used in this analysis was exactly the same as the one used in Section 5.3.2, however, the weight of the wing torque box structure was now changed and hence the total loading was different. Table 29 gives the loading on the Model 2 during level flight cruise conditions.

Table 29: Total Loading on the Structure due to Aerodynamic and Inertial Loading during Level Flight Cruise Conditions

Loading Type	Direction	Force [N]	Moment [N.m]
Aerodynamic Load	X	0.0	-34.3
	Y	-2.3	-137.0
	Z	216.3	-2.3
Inertial Load Due to Gravity	X	0	14.0
	Y	0	50.5
	Z	-70.7	0.0
Total	X	0.0	-20.3
	Y	-2.3	-86.5
	Z	145.6	-2.3

Under the effect of the loading at level flight cruise conditions the displacement field of the wing torque box structure is given in Figure 90. The maximum displacement was found to be 2.99 [mm]. Figure 91 shows the stress distribution on the internal structure of the wing torque box. It was determined that the maximum Von-Misses stress of 29.4 [MPa] occurred at the main spar boundary location. Figure 92 gives the zoomed view of the maximum stress location at the boundary of the main spar.

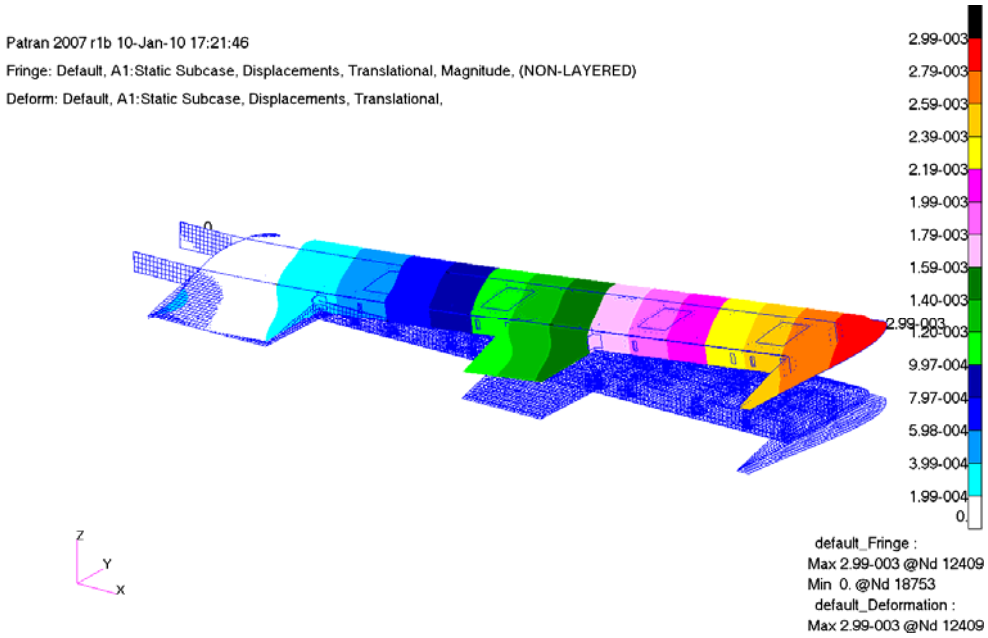

Figure 90: Displacement Field of the Wing Torque Box under Loading at Level Flight Cruise Condition

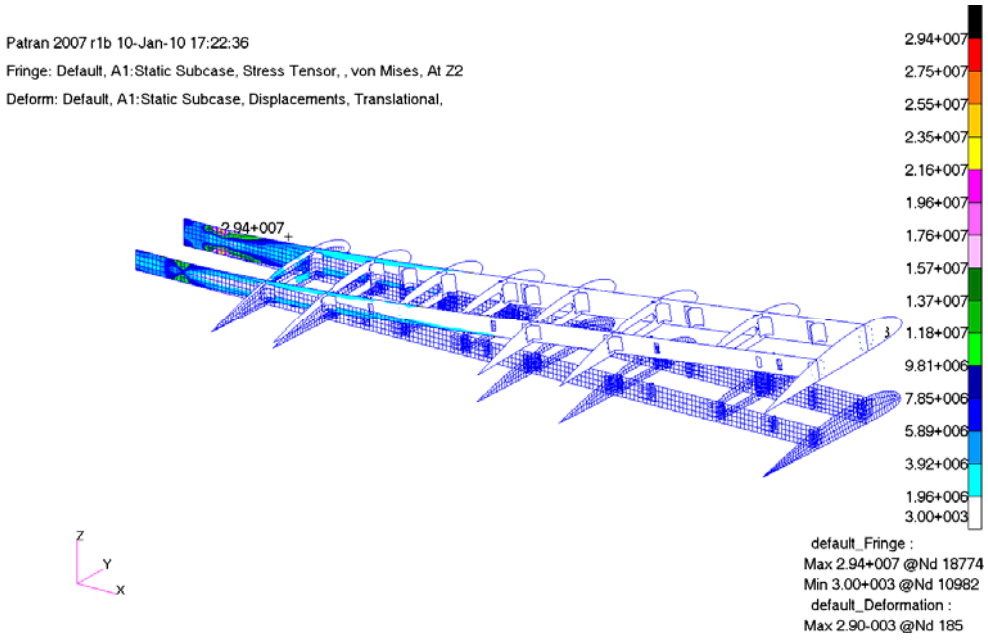

Figure 91: Stress Distribution of the Wing Torque Box Internal Structure under Loading at Level Flight Cruise Condition

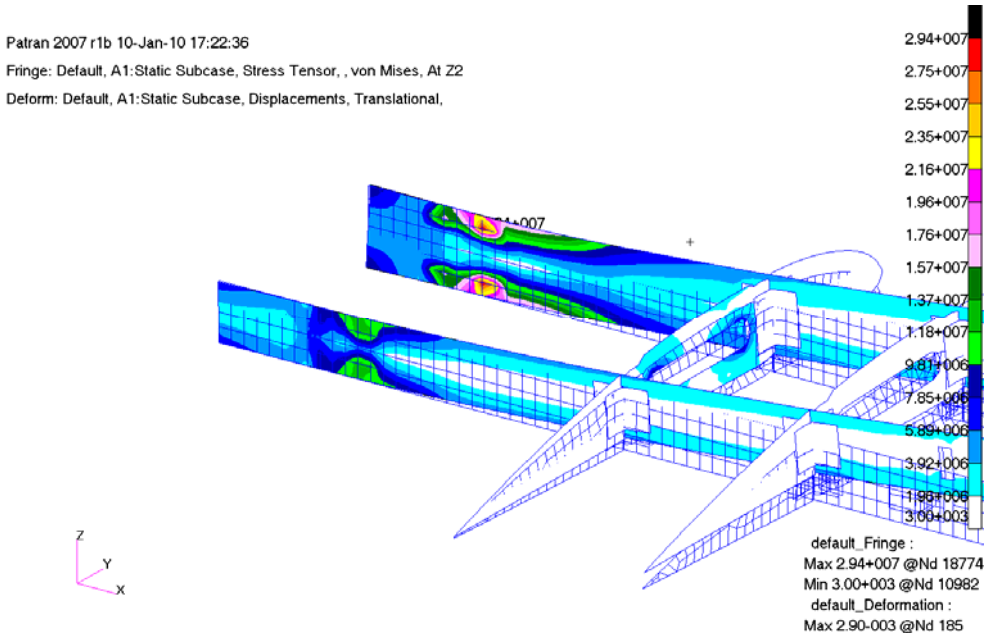

Figure 92: Zoomed View of the Maximum Stress Location at the Main Spar Boundary under Loading at Level Flight Cruise Condition

8.7.1.3 The Static Analysis of the Model 2 in 5g Pull-down Maneuver

The designated maximum loading case that the wing could be subjected during flight was the pull-down maneuver with a maximum load factor of 5g. Table 30 gives a summary of the loading on the Model 2 in the case of that maximum loading.

Table 30: Total Resultant Loading on the Structure Due to Aerodynamic and Inertial Loading during a Pull-down Maneuver with Maximum Load Factor

Loading Type	Direction	Force [N]	Moment [N.m]
Aerodynamic Load	X	0.0	-168.3
	Y	-11.6	-684.9
	Z	1081.3	-11.3
Inertial Load Due to Gravity	X	0	-14.0
	Y	0	-50.5
	Z	70.7	0.0
Total	X	0.0	-182.3
	Y	-11.6	-735.4
	Z	1152.0	-11.3

The displacement field of the wing torque box under the loading due to the pull-down maneuver with maximum load factor is given in Figure 93. The maximum displacement of 25.9 [mm] was found to occur at the tip of the wing torque box. The stress distribution on the internal structure of the wing torque box as a result of the loading given in Table 30 is shown in Figure 94. The maximum Von-Misses stress of 237 [MPa] took place at the main spar boundary. In addition to these Figure 95 shows the zoomed maximum stress location at the main spar boundary. The maximum Von-Misses stress of 237 [MPa] found in the aluminum 7075-T651 and its 503 [MPa] yield strength had resulted in a factor of safety of 2.12 and indicated a safe condition.

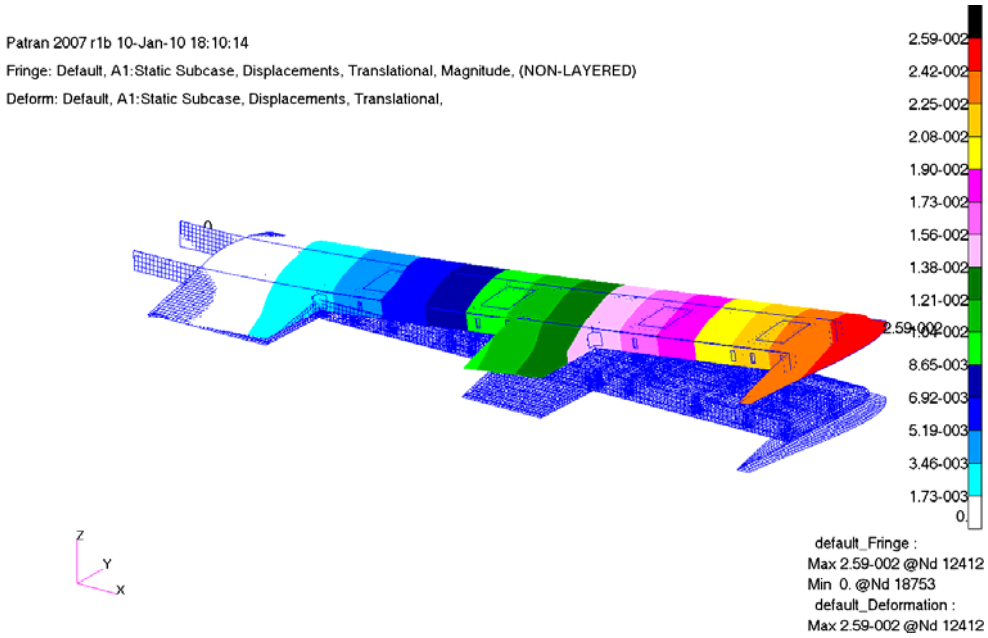

Figure 93: Displacement Field of the Wing Torque Box under Loading at Pull-down Maneuver with Maximum Load Factor of 5g

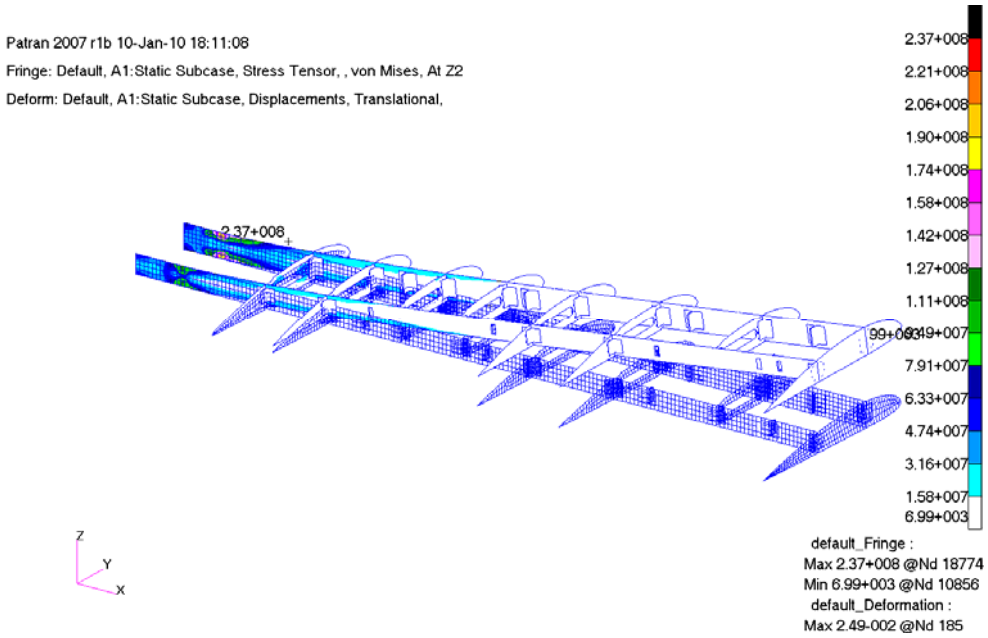

Figure 94: Stress Distribution of the Wing Torque Box Internal Structure under Loading at Pull-down Maneuver with Maximum Load Factor of 5g

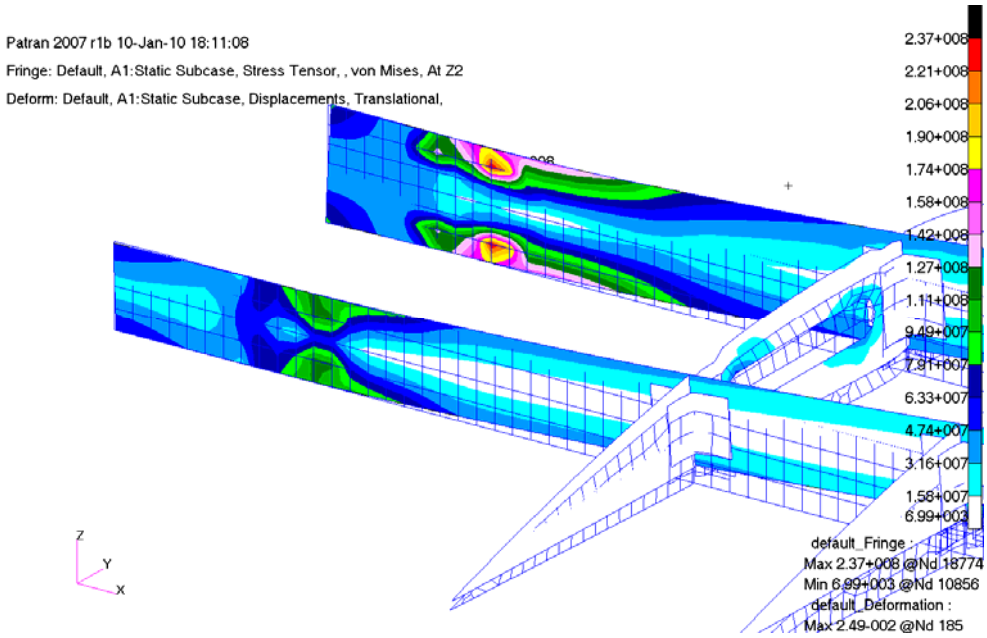

Figure 95: Zoomed View of the Maximum Stress Location at the Main Spar Boundary Condition under Loading at Pull-down Maneuver with Maximum Load Factor of 5g

8.7.2 The Buckling Analysis of Model 2

The panel buckling characteristics of the wing torque box structure were examined under the designated maximum load case of pull-down maneuver with maximum load factor of 5g. The loading case given in Table 30 was used during the current analysis as well. When the analysis was conducted a buckling factor of -1.4871 was found which indicated a safe design. The resulting case is shown in Figure 96.

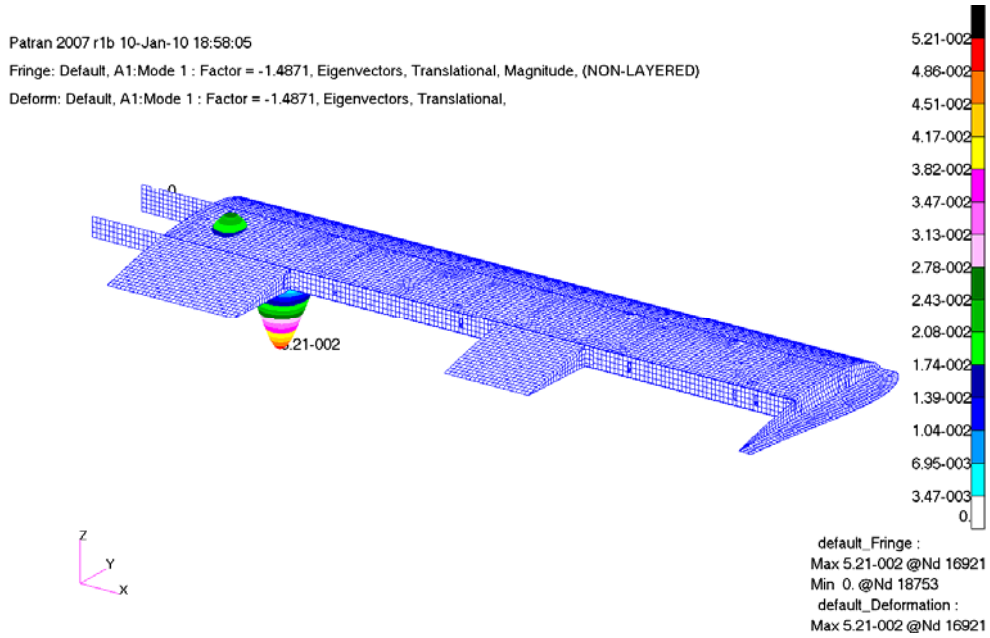

Figure 96: Translational Eigenvectors Representation of the Buckling Analysis Results under Loading of Pull-down Maneuver with Maximum Load Factor of 5g

8.8 Discussion

This section detailed the verification studies conducted for the developed finite element model of the wing torque box. The model was updated and the tuned model was proved to be the safe after various structural analyses studies.

CHAPTER 9

CONCLUSION

9.1 General Conclusions

In this thesis a wing torque box structure of an unmanned aerial vehicle, on which the mission adaptive control surfaces will be installed, was studied. The wing torque box was structurally modeled by using MSC®/PATRAN package program and the structural analyses were conducted by the help of the MSC®/NASTRAN package program. The designed and structurally analyzed wing torque box was then manufactured by TUSAŞ Aerospace Industries (TAI). During the manufacturing process the required technical drawings were developed by using the Computer Aided Design tool KeyCreator of Kubotek. The manufactured wing torque box was then subjected to ground vibration tests. Furthermore, the results obtained from the experiments were used for the verification and the tuning of the initially developed structural model. Finally, the verified structural model was again structurally analyzed to obtain the final theoretical results. The structural analyses conducted on the experimentally verified and tuned structural model showed that, the structure could sustain each and every type of anticipated loading condition studied.

Although, the theoretical model was developed by including each and every detail, it was observed that the actual results could only be reached by repeatable experimental studies. The experimental data should always be accepted as a baseline for structural modeling. Therefore, the structural model must be updated by using experimental results.

9.2 Recommendations for the Future Work

The wing torque box designed can be subjected to a formal optimization study.

The composite skin of the wing torque box was manufactured from 7781 E-Glass Fabric – LY5052 Araldite Resin – HY5052 Aradur Hardener with staking sequence of 0°/90°/0°/90°/0°/90°/0°/90°. The ply orientation of the composite skin can be changed and/or optimized to improve the stiffness characteristics and hence to modify the modal characteristics of the wing torque box.

The aeroelastic characteristics of the wing torque box can also be studied in detail.

Since they were not within the scope and intention of the current thesis; the fatigue characteristics of the designed wing were not investigated. However, as a future study those might be considered.

REFERENCES

[1] Insuyu, E. T., “Aero-structural Analysis of an Unmanned Aerial Vehicles and Its Mission Adaptive Wing”, MSc. Thesis, METU, February 2010

[2] Sakarya, E., “Structural Design and Evaluation of and Adaptive Camber Wing”, MSc. Thesis, METU, February 2010

[3] Friswell, M. I., Inman, D. J., “Morphing Concepts for UAVs”, 21st Bristol UAV Concepts Conference, April 2006

[4] Gilbert, W. W., “Mission Adaptive Wing System for Tactical Aircraft”, AIAA Journal of Aircraft, Vol. 18, No. 7: 597-603, July 1981

[5] Andersen, G. R., Cowan, D. L., Piatak D. J., “Aeroelastic Modeling, Analysis and Testing of a Morphing Wing Structure, AIAA, 2007

[6] Kota, S., Osborn, R., Erwin, G., Maric, D., Flick, P., Paul, D., “Mission Adaptive Compliant Wing – Design, Fabrication and Flight Test”, RTO-MP-AVT-168, 2006

[7] Raymer, D. P., “Aircraft Design: A Conceptual Approach”, AIAA Education Series, 1989

[8] Blevins, R. D., “Formulas for Natural Frequency and Mode Shape”, Van Nostrand Reinhold Company, 1979

[9] Niu, C. Y. M., “Airframe Structure Design”, Conmilit Press, 1989

[10] Susuz, U., “Aeroelastic Analysis of an Unmanned Aerial Vehicle”, MSc. Thesis, METU, January 2008

[11] Automation Creations Inc., ‘Online Materials Information Resource’, www.matweb.com, 1999

[12] Cook, R. D., Malkus, D. S., Plesha, M. E., Witt, R. J., “Concepts and Applications of Finite Element Analysis”, John Wiley & Sons Inc., 2001

[13] MSC.Patran, Reference Manual, MSC.Software, 2007

[14] Megson, T. H. G., “Aircraft Structures for Engineering Students”, Butterworth Heinemann, 2003

[15] Callister, Jr., W. D., “Materials Science and Engineering an Introduction”, John Wiley & Sons Inc.

[16] Beer, F. P., Johnston, Jr., E. R., DeWolf, J.T., “Mechanics of Materials”, McGraw-Hill Inc., 2002

[17] Anderson, Jr., J. D., “Aircraft Performance and Design”, McGraw-Hill Inc., 1999

[18] Anderson, Jr., J. D., “Fundamentals of Aerodynamics”, McGraw-Hill Inc., 1984

[19] Product Data Sheet: KeyCreator, Kubotek USA Inc., 2008

[20] ASTM Designation: D 2584 – 08, “Standard Test Method for Ignition Loss of Cured Reinforced Resins”

[21] Jones, R. M., “Mechanics of Composite Materials”, Brunner-Routledge, 1998

[22] Withcomb, J., Tang, X., “Effective Elastic Moduli of Woven Composites”, Journal of Composite Materials, December 2001, 35: 2127-2144

[23] Data sheet: Araldite LY5052 / Aradur HY5052. Ciba polymers, Switzerland, 1994

[24] Ewins, D. J., “Modal Testing: Theory and Practice”, Research Studies Press Ltd., 1984

[25] Schwarz, B. J., Richardson, M. H., “Experimental Modal Analysis”, CSI Reliability Week, Orlando, FL, October 1999

[26] Product Data Sheet: Impact Hammers – Types 8206, 8206-001, 8206-002, 8206-003, B&K, BP2078-12, 2005

[27] Beer, F. P., Johnston, Jr., E. R., “Vector Mechanics for Engineers: Statics”, McGraw-Hill Inc., 1998

APPENDIX A

CALCULATION OF DESIGN PARAMETERS

The most important design parameters related to this work were the lateral rigidity and the mass of the structure. In order to properly estimate the required lateral rigidity and the mass the basic aerospace engineering design approach was preferred. According to this approach an estimate mass of the wing structure calculated. Afterwards, the main structural members were located to satisfy the control system requirements using conventional structural design methodology as a guide. The final stage was to select the member thicknesses and materials. In order to get a simultaneous solution a formulation based on trial-error method was used regarding the overall lateral rigidity.

The formulation was calculating the mass and lateral rigidity of the structure simultaneously with any change applied on any design parameter. The governing equations for the formulation were the simple second moment of area equations [27]. Assuming the neutral axis is parallel to the chord line of the wing cross-section and calling that axis as x-axis the Eqn. A.1 below is the second moment area of any area with respect to that axis.

$$I_x = \int y^2 dA + Ad^2 \qquad \text{(Eqn. A.1)}$$

There were some other assumptions made during generating the algorithm. First of all, the stiffness effects of the ribs were ignored and the structure was assumed to have uniform cross-sectional properties. The second one was the skin can be regarded as finite segments which has second moment of area values that can be summed to be equal to the total second moment of area value of the whole skin cross-section. The third assumption was ignoring the second moment of area values

of the skin segments with respect to their own centroid, since they were very small compared to their second moment of area values with respect to the neutral axis. All these assumptions were made since the calculation of the parameters were estimate and slight errors seemed tolerable.

The required input for the algorithm was the elastic modulus, density and thickness values of spars and the skin. The axial stiffness and weight of the structure were then estimated by the formulation.

The program was helpful for assigning the materials and the thicknesses to the main structural members in order to satisfy a specific stiffness to weight ratio. The Figure 97 below is a segment of the program calculating the lateral rigidity and the mass of the skin. The Figure 98 is the segment calculating the lateral rigidity and the mass of the spars.

B	C	D	E	F	G	H	I	J	K	L	M	N	O
x	y	dx	dy	y	y2	absdx	absdy	area	Ix	Ix m^4	t	Ixx	5,20746E-07
0	0	-0,13642	1,984492	7,007754	49,10862	0,136421	1,984492	2,14831	105,5005	1,05501E-10	1,08	Ixx2	2,60373E-07
-0,13642	1,984492	0,092771	0,840418	5,595299	31,30737	0,092771	0,840418	0,913165	28,58878	2,85888E-11	1,08		
-0,04365	2,82491	0,281049	1,206756	4,571712	20,90055	0,281049	1,206756	1,338176	27,96861	2,79686E-11	1,08		
0,237399	4,031666	0,698149	1,742356	3,097156	9,592375	0,698149	1,742356	2,027185	19,44552	1,94455E-11	1,08		
0,935548	5,774022	1,591603	2,532515	0,959721	0,921063	1,591603	2,532515	3,230416	2,975418	2,97542E-12	1,08		
2,527151	8,306537	1,703881	1,993855	-1,30346	1,69902	1,703881	1,993855	2,832539	4,81254	4,81254E-12	1,08		
4,231032	10,30039	3,566628	3,240874	-3,92083	15,3729	3,566628	3,240874	5,20467	80,01087	8,00109E-11	1,08		
7,79766	13,54127	4,619144	3,309455	-7,19599	51,78232	4,619144	3,309455	6,136927	317,7843	3,17784E-10	1,08		
12,4168	16,85072	4,724371	2,831641	-10,2665	105,4019	4,724371	2,831641	5,948621	626,9958	6,26996E-10	1,08		
17,14118	19,68236	4,795307	2,510955	-12,9378	167,3877	4,795307	2,510955	5,84597	978,5434	9,78543E-10	1,08		
21,93648	22,19332	4,848092	2,270956	-15,3288	234,972	4,848092	2,270956	5,781909	1358,586	1,35859E-09	1,08		
26,78457	24,46427	9,813556	3,997415	-18,463	340,8816	9,813556	3,997415	11,44419	3901,114	3,90111E-09	1,08		
36,59813	28,46169	9,929583	3,436891	-22,1801	491,9583	9,929583	3,436891	11,34817	5582,825	5,58282E-09	1,08		
46,52771	31,89858	10,01554	2,992459	-25,3948	644,8963	10,01554	2,992459	11,28928	7280,412	7,28041E-09	1,08		
56,54326	34,89104	10,08206	2,618051	-28,2001	795,2436	10,08206	2,618051	11,24975	8946,295	8,94629E-09	1,08		
66,62532	37,50909	10,13477	2,290187	-30,6542	939,6789	10,13477	2,290187	11,22153	10544,64	1,05446E-08	1,08		
76,76009	39,79928	10,17699	1,995453	-32,797	1075,643	10,17699	1,995453	11,20044	12047,68	1,20477E-08	1,08		
86,93708	41,79473	10,21089	1,72554	-34,6575	1201,142	10,21089	1,72554	11,18412	13433,72	1,34337E-08	1,08		
97,14797	43,52027	10,23796	1,474981	-36,2578	1314,625	10,23796	1,474981	11,17115	14685,88	1,46859E-08	1,08		
107,3859	44,99525	10,25925	1,240005	-37,6153	1414,907	10,25925	1,240005	11,16063	15791,26	1,57913E-08	1,08		
117,6452	46,23526	10,2756	1,0179	-38,7442	1501,113	10,2756	1,0179	11,15196	16740,36	1,67404E-08	1,08		
127,9208	47,25316	10,28763	0,806659	-39,6565	1572,637	10,28763	0,806659	11,14475	17526,64	1,75266E-08	1,08		
138,2084	48,05981	10,29586	0,60475	-40,3622	1629,106	10,29586	0,60475	11,13869	18146,12	1,81461E-08	1,08		
148,5043	48,66456	10,30071	0,410974	-40,8701	1670,361	10,30071	0,410974	11,13361	18597,16	1,85972E-08	1,08	E	2,20E+10
158,805	49,07554	10,30252	0,224374	-41,1877	1696,429	10,30252	0,224374	11,12936	18880,17	1,88802E-08	1,08	EI	5,73E+03
169,1075	49,29991	10,30162	0,044171	-41,322	1707,507	10,30162	0,044171	11,12585	18997,47	1,89975E-08	1,08	den	1772
179,4091	49,34408	10,29824	-0,13029	-41,2789	1703,951	10,29824	0,130285	11,12299	18953,03	1,8953E-08	1,08	W	2,939340913

Figure 97: The Segment of the Program Calculates the Skin Parameters

Q	R	S	T
MAIN SPAR WEB		SECONDARY SPAR WEB	
yt	45,88374234	yt	39,389329
yb	-11,42431426	yb	-3,670721791
ybar	20,6540283	ybar	21,53002539
t	2,54	t	2,54
Ixx	1,01934E-07	Ixx	6,75983E-08
area	145,5624638	area	109,372529
MAIN SPAR UPPER FLANGE		SECONDARY SPAR UPPER FLANGE	
yt	2,5	yt	2,5
ybar	37,88374234	ybar	31,389329
t	25	t	25
Ixx	8,97312E-08	Ixx	6,16132E-08
area	62,5	area	62,5
MAIN SPAR LOWER FLANGE		SECONDARY SPAR LOWER FLANGE	
yt	2,5	yt	2,5
ybar	19,42431426	ybar	11,67072179
t	25	t	25
Ixx	2,36141E-08	Ixx	8,54541E-09
area	62,5	area	62,5
Ixx TOTAL	2,15279E-07		1,37757E-07
area total	0,000270562	area total	0,000234373
E	7,30E+10	E	7,30E+10
EI	7,44E+03	EI	4,93E+03
den	2780	den	2780
W	1,128245474		0,977333446
EI TOTAL	18104,03		
W TOTAL	5,044919833		

Figure 98: The Segment of the Program Calculates the Spar Parameters

APPENDIX B

VIBRATION TEST BENCH

During the study in order to conduct the ground vibration tests a testing bench was needed and hence it was designed and externally produced. The most important design criterion was the first natural frequency of the bench. The first natural frequency had to be higher than the last natural frequency of interest of the wing torque box, which was the second out-of-plane natural frequency. The second out-of-plane bending natural frequency of the Model 1 was found to be 106.67 [Hz]. Therefore, it was thought that a natural frequency value of roughly 50 [Hz] higher than that value was required for the first natural frequency of the bench. The bench was designed and in accordance a first natural frequency value of 155.57 [Hz] was obtained in free-free boundary conditions. Figure 99 shows the first non-rigid body mode shape of the test bench at 155.57 [Hz].

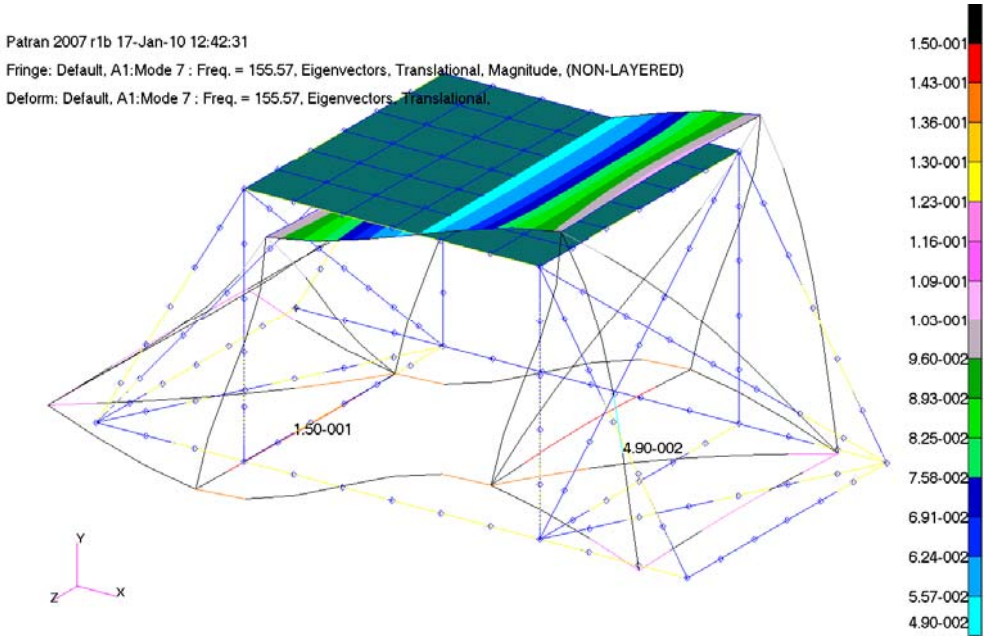

Figure 99: First Non-Rigid Body Mode Shape of the Test Bench [155.57 Hz]

The design was produced by the help of the technical drawings; Figure 100 and Figure 101 give the technical drawings of the truss leg structures which were produced from ST32 steel construction profiles and Figure 102 shows the technical drawing of the main bench which was manufactured from Aluminum 2024 block by using CNC machining. The wing was fixed onto the main bench with the help of steel blocks. Figure 103 and Figure 104 illustrate the clamp blocks which were produced from ST32 steel. In addition to those, Figure 105 is the manufactured and assembled test bench with the wing torque box mounted on it. Furthermore, Figure 106 shows the boundary where the wing torque box clamped on the vibration test bench.

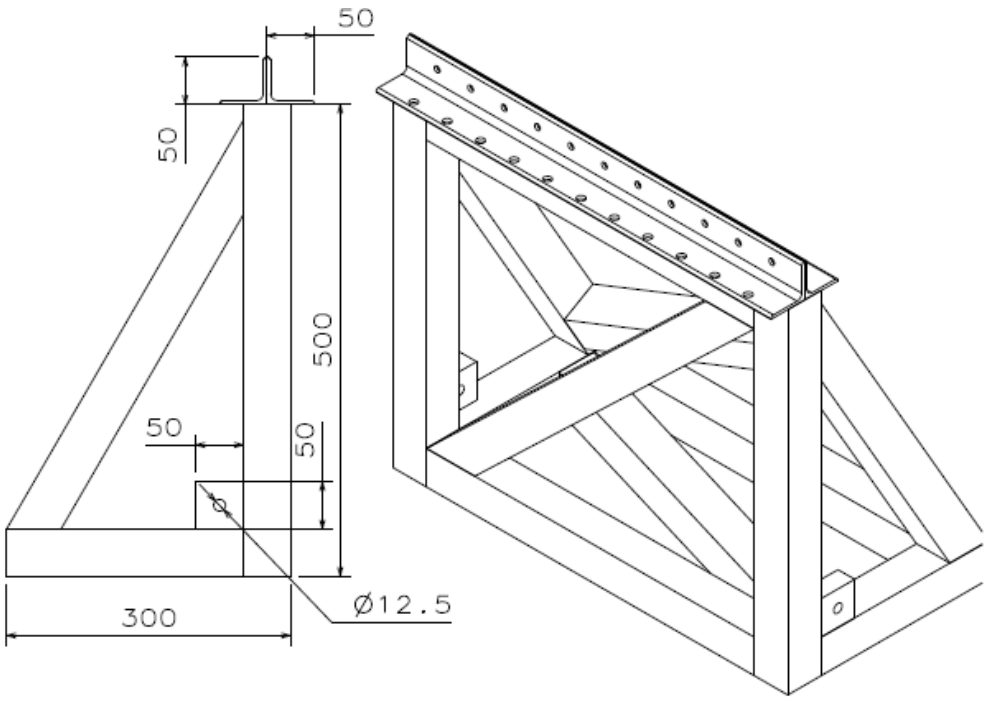

Figure 100: Left and Isometric Views of the Truss Leg Structure [mm]

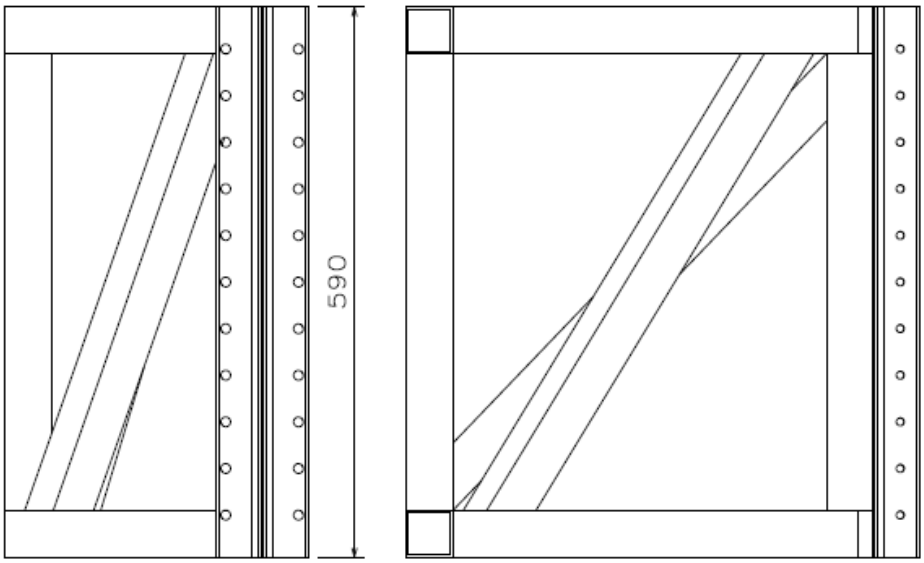

Figure 101: Top and Front Views of the Truss Leg Structure

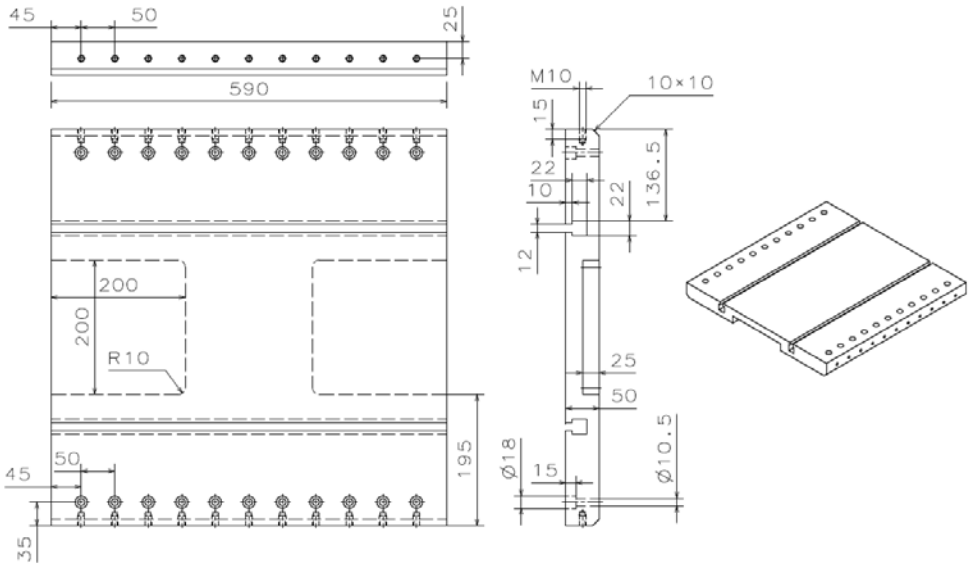

Figure 102: Front, Left, Top and Isometric Views of the Main Bench [mm]

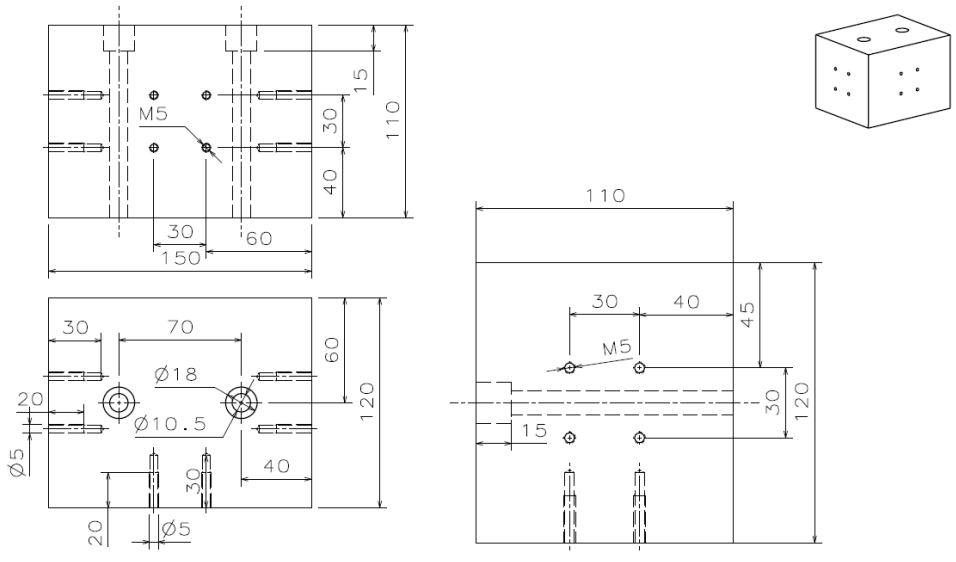

Figure 103: Front, Left, Top and Isometric Views of a Unique Clamp Block [mm]

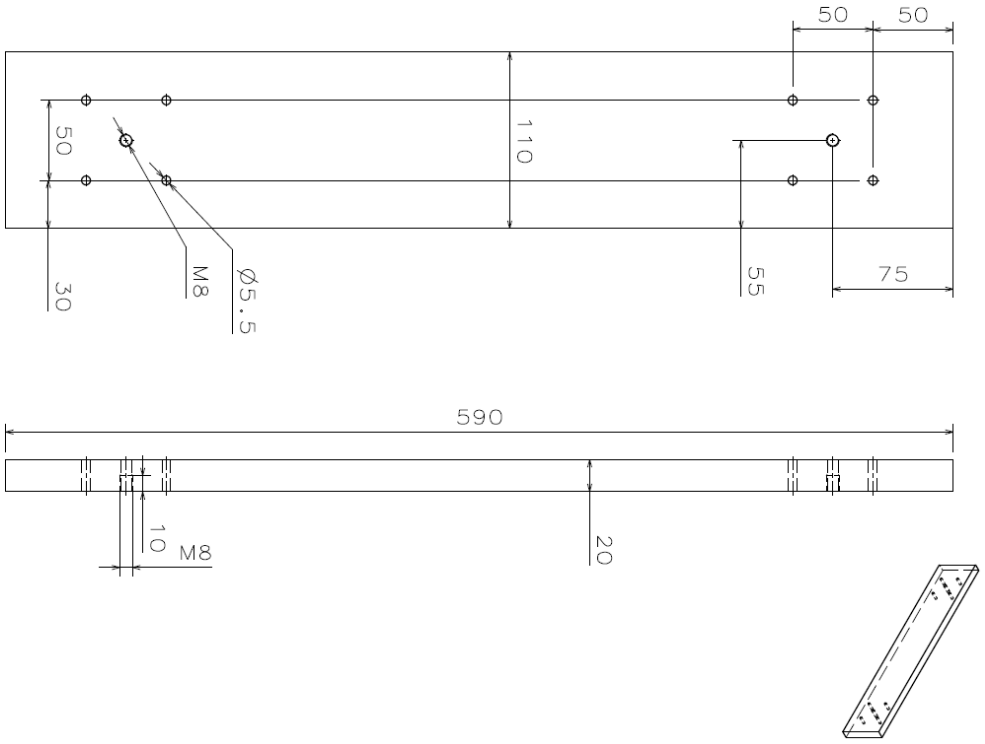

Figure 104: Front, Left, Top and Isometric Views of a Unique Clamp Block

Figure 105: The Picture of the Assembled Vibration Test Bench and the Wing Torque Box Mounted on It

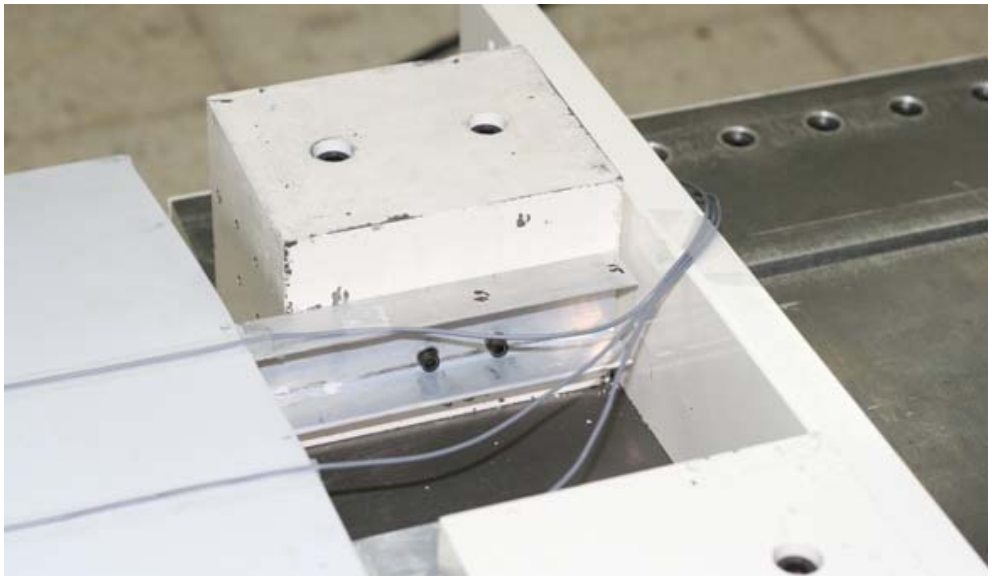

Figure 106: The Wing Torque Box Boundary on the Vibration Test Bench